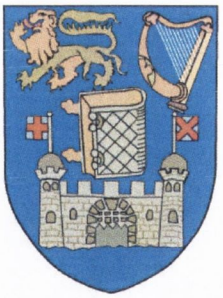

Theoretical studies of doped carbon nanotube-based materials

by

Andrew Wall

A thesis submitted for the degree

of Doctor of Philosophy

School of Physics

Dublin University

Trinity College Dublin

Declaration

I have not previously submitted this thesis as an exercise for any degree.

The work in this thesis is mine, except where I specifically refer to published or unpublished work carried out with the help of those collaborators whom I have acknowledged in the text.

The Library has my permission to lend or copy this work, if requested.

Andrew Wall May 2018

Andrew Wall

Summary

For the last fifteen years, carbon nanotubes have piqued the interest of many in the materials research community, due to their superlative individual characteristics. One possible route to their technological exploitation may lie through utilising their interactions with other materials. Proposed uses for nanotubes, which depend crucially on their behaviour when exposed to such foreign substances, variously include use as sensors, as interconnects in electronic devices, as non-conventional transistor elements, as conductive agents in non-conductive plastics, as hydrogen storage devices and as components in super-tough fibres, capable of being used in light-weight body armour. In each case of crucial importance is the detailed interaction that occurs between the nanoscopic carbon cylinders and other materials.

To this end, we have performed a range of theoretical investigations into the interaction between carbon nanotubes and foreign agents. Among other things, we have proposed a theoretical framework capable of modeling the electronic interaction between nanotubes and doping bodies based on the existence of well-known sum rules for interaction-induced changes in the density of states of the system. Using simple models for the electronic structure of the dopant and the nanotube, we have investigated the effect that different dopants have on the electronic structure of the combined structure. Mathematically transparent, and numerically light-weight, the scheme allows not simply qualitative analysis, but also quantitative. To this end we have utilised the method to perform calculations for the electronic structure of nanotubes doped with atoms and small molecules. Our analysis has allowed us to derive a scheme capable of parameterising semi-empirical electronic structure calculations involving many dopants, by using the outputs of *ab-initio* calculations for a few foreign objects. Our method also allows us to show the existence of correlations between the binding energy and the charge transfer that takes place between the parts, when a dopant is brought into contact with a nanotube.

Furthermore, we have treated the interaction between a nanotube and a wrap-

ping polymer by treating it as a polarising perturbation to the electronic structure of the nanotube. Through the calculation of the electronic contribution to the binding energy of a wrapped nanotube, we show how it is possible for a spontaneous chiral order to form in a nanotube / wrapping molecule system, due to the existence of energetically favourable wrapping angles. We have investigated how the electronic structure of a nanotube responds when exposed to a polarising, wrapping perturbation, such as is the case when a charged polymer attaches itself to the surface of a nanotube in a helically ordered fashion. In particular, we have investigated the manner in which the coiling angle, the strength of the interaction, and the role of coverage impact on the density of states of the nanotube. In addition a simple classical model is used to investigate the interfacial adhesion between a nanotube and a wrapping polymer, which leads to a clarification of how nanotubes may be capable of reinforcing a polymer / nanotube composite.

Acknowledgements

Over the last four years I have received immeasurable support from so many people without whose help I would not be writing this today. In particular, I would like to thank those people I have been lucky enough to collaborate with directly: Dr. Mauro S. Ferreira, Dr. Claudia G. Rocha, Dr. Alexandre R. Rocha and Prof. Jonathan N. Coleman. I must thank my supervisor Mauro, for his patience and his attention to my work. One of the advantages of working in a relatively small group is the chance for regular one-on-one interaction with those who know far more than you do. So for a constantly open door, and a constantly open mind, I am grateful. I must also give a special thank you to Claudia, for whose help in performing *ab-initio* calculations I am especially thankful. Thanks as well to David Kirwan, who proofread a portion of this thesis, and to Felipe, who helped me reason through a particularly thorny problem towards the end of my thesis. I must also thank Stefano Sanvito and his group, who have provided scientific and computing support, as well as someone to have lunch with.

I must mention the financial support that I have received from both the Irish Research Council for Science, Engineering and Technology, who awarded me an inaugural Government of Ireland Scholarship under the Embark initiative, and from Science Foundation Ireland, who also funded me for part of the duration of the project. Suffice to say, the existence of such funding was a crucial factor in my deciding to continue my studies in Ireland. Indirect assistance also came in the form of the complimentary access to world class computational facilities; for this I owe thanks to the Trinity Centre for High-Performance Computing and to the Irish Centre for High-End Computing.

On a more personal note, I must mention the unwavering support that my family has given me, both during my undergraduate studies and during this postgraduate work. Thanks to my parents Joe and Gráinne and to my brothers Michael, David and Conor. Thanks to Paddy and Mick for giving me something to smile at. A special

mention must go to my aunt Eileen McGlade, who gave me an insider's glimpse into the academic life, and who always emphasised the importance of education.

I count myself lucky beyond reckoning to have made such good friends over the years. For the love and friendship that you have given me, I must thank Ciara, Rónán, Deco, Keith, John and Karen, Enda, Turlough, Leanne, Fiona, Eoin and Aileen[1].

[1]Order determined by random allocation

Contents

List of Figures

List of Tables

Chapter 1

Introduction

1.1 Historical perspective

The discovery of the carbon nanotubes is commonly attributed to the Japanese scientist Sumio Iijima, who first described them in 1991 [1]. Iijima used state-of-the-art high resolution transmission electron microscopy to image what he referred to as nanoscopic needles of carbon. While there is convincing evidence that this was not the first time that nanotubes had been synthesized, what is certain is that he was the first to give a detailed description of the form and structure of these remarkable structures.

It soon became clear that carbon nanotubes were an intriguing material with interesting physical properties. Early theoretical predictions of the electronic properties of the single walled nanotubes raised the prospect that a subclass of them may be electrically conductive [2]; subsequent experiments showed the accuracy of such early predictions. A crucial step in this demonstration was showing the stability of the structure against the so-called Peierl's distortion - the symmetry breaking mechanism which ensures that undoped one-dimensional structures have a vanishing density of states (DOS) at the Fermi level, and thus cannot carry an electric current. Carbon was already known to form useful materials: graphite is one of the

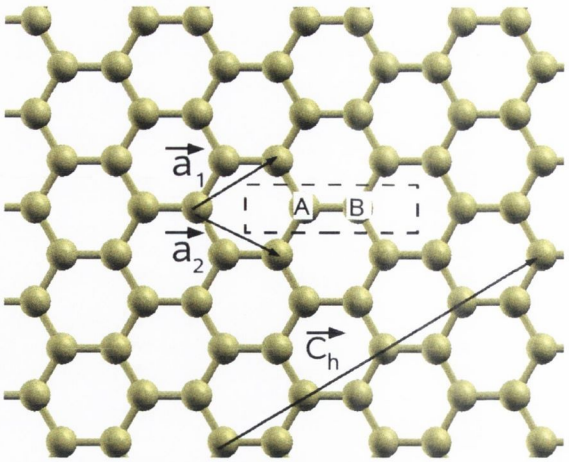

Figure 1.1: Ball and stick models for a graphene sheet. Displayed are the unit cell, delimited by the dashed lines, the unit vectors $\vec{a}_1$ and $\vec{a}_2$, and the chiral vector $\vec{C}_h$ for a $(4, 0)$ nanotube. The two inequivalent sites A and B are also labelled.

best lubricants we have, while diamond is both the hardest material and the best thermal conductor known. Partly by analogy with the known electronic structure of graphite, nanotubes were quickly predicted to have remarkable thermal, mechanical, electronic and electrical properties, which would see them catapulted to the forefront of the nascent field which had the aim of utilising nanostructures for technological applications.

Before giving details of those properties that excited such early interest in these nanoscale structures, it is worth addressing the question: just what *are* these carbon nanotubes?

1.2 Geometry of nanotubes

We begin by describing the geometry of carbon nanotubes. Carbon is one of the most versatile elements, in the sense that structures of pure carbon can occur which are essentially 0D (fullerenes), 1D (nanotubes), 2D (graphene), and 3D (diamond, graphite). Of these forms, perhaps the most familiar is graphite (diamond being the other form met in everyday life). Graphite consists of stacked layers of carbon atoms

arranged into a hexagonal honeycomb lattice. Successive layers are spaced by about 3.5Å and are attracted to each other through a weak van der Waals interaction. The weakness of this interaction is what allows the layers to slide over one another, the property which makes graphite such an excellent lubricant. A single sheet of graphite is what is referred to as graphene, a material that is only recently coming into sharp focus for the research community in its own right [3, 4, 5]. In fact, the geometry of nanotubes is most easily described in terms of that of graphene, which is a hexagonal, planar structure. At each vertex resides a carbon atom, and the edges of the lattice correspond to strong sp^2-hybridised chemical bonds. As carbon has four valence electrons, and it forms three bonds with neighbours (each of length about 1.42Å), we must account for one extra electron per atom. This extra electron goes into a dumb-bell shaped orbital perpendicular to the graphene plane, and the electronic structure of the graphene sheet is essentially determined by these so-called π-orbitals. Graphene has a trigonal Bravais lattice spanned by vectors $\vec{a}_1$ and $\vec{a}_2$ with a two atom basis, the inequivalent atoms being labelled A and B. The geometry of a graphene sheet is specified in Fig. 1.1. An important parameter is the length of these basis vectors, which we will simply denote by the symbol a; it is the distance between nearest equivalent atoms.

The structures that interest us in this work are the essentially one-dimensional nanotubes. A single-walled carbon nanotube (SWNT) is like a parallelogram-shaped section of a graphene sheet with four equivalent carbon atoms (all of type A or of type B) at the corners, which is deformed into a cylindrical structure such that the slanted lines are coincident. Double-walled nanotubes consist of two such concentric cylinders, while tubes with more than two walls are called multi-walled nanotubes. The shortest vector in the graphene plane that connects two carbon atoms that are to be rolled on top of each other is called the *chiral vector*, $\vec{C}_h$. The chiral vector for a $(4,0)$ zigzag nanotube is displayed in Fig. 1.1. With reference to unit vectors $\vec{a}_1$ and $\vec{a}_2$ of graphene, we usually refer to a (n,m)-nanotube as that nanotube that

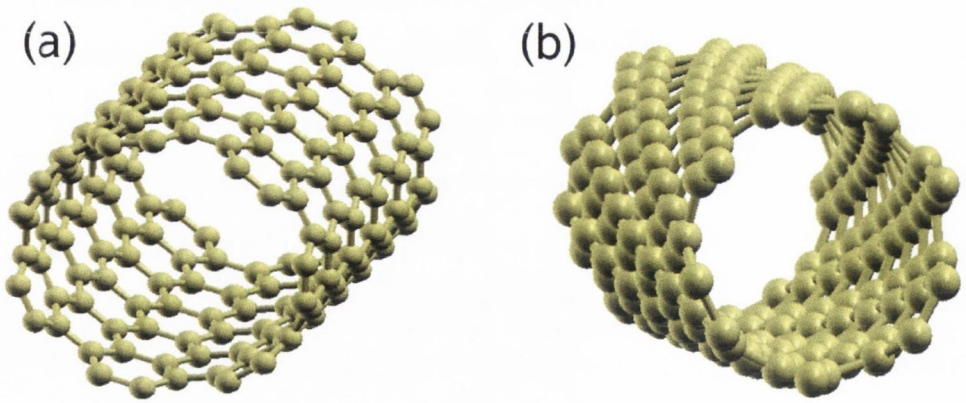

Figure 1.2: Ball and stick models for two nanotubes. In panel (a) we display the schematic for 6 fundamental unit cells of a metallic (7,7) nanotube. This achiral nanotube displays no helicity, in contrast to the (6,3) nanotube, displayed in panel (b), which displays a clear helicity.

is uniquely generated by choosing $\vec{C}_h = n\vec{a}_1 + m\vec{a}_2$, and n and m are called the chiral indices of the nanotube. Due to the variety of ways in which a graphene sheet can be rolled upon itself, we see the existence of a plethora of different types of nanotubes, each specified by its chiral indices. Theory, and indeed experiment, show that properties such as the intrinsic conductance of nanotubes are governed by their chiral indices. In particular, it is found that a nanotube that has $n = m$ is inherently metallic, and such tubes are called *armchair nanotubes*. Together with the zig-zag tubes, characterised by $m = 0$, we have the set of achiral nanotubes. These molecules are identical to their mirror images. All other tubes fall into the class of achiral tubes. The geometry of an achiral (a (7,7) armchair nanotube) and a chiral tube (a (6,3) nanotube) is depicted in Fig. 1.2, where the "twist" of the lattice is readily apparent in the chiral tube, but non-existent for the achiral tube.

As regards their size, typical single-walled nanotubes tend to have diameters of the order of a nanometre, with thicker tubes tending to undergo structural deformation. There seems to be no upper limit on the length of nanotubes; reports have indicated growth of up to 4cm [6] (an apparently apparatus limited upper bound).

However, typical lengths are in the micro-metre range, giving an extremely large aspect ratio [7]. Such a large aspect ratio is what allows us to view the nanotubes as being one-dimensional structures. As grown, carbon nanotubes tend not to be found in this pristine form. They can suffer a range of defects, including substitutional defects (where a carbon atom can be replaced by an atom such as boron), vacancy defects, and Stone-Wales type defects (where a bond is rotated by 90 degrees in the plane of the molecule). In real life, things are further complicated by the propensity of nanotubes to aggregate together to form bundles.

1.3 Intrinsic properties of nanotubes

Much research into carbon nanotubes is driven by their remarkable electronic, thermal and mechanical properties. Nanotubes can display high levels of purity, and a low level of defects, as evidenced by microscopy. While typical defects that can occur in nanotubes, including topological defects and vacancy defects, certainly have an impact on the physical properties, crucially the defected structures still possess exceptional intrinsic properties. It is worth noting in passing that the amount of defects in the nanotube is usually determined by how they are grown, be it by laser ablation, arc-discharge or chemical vapour deposition. Typically, those nanotubes grown by arc-discharge possess a higher concentration of defects, which can impact on the as-measured physical properties of the structure. It is worth spelling out some of the most exceptional properties that as-grown nanotubes possess, which I now do.

1.3.1 Electronic properties

It has already been stated that the so-called chiral indices (n, m) play a crucial role in determining the electronic properties of nanotubes. In fact, theory predicts that single-walled nanotubes can be conducting ($m = n$), semiconducting with a tiny

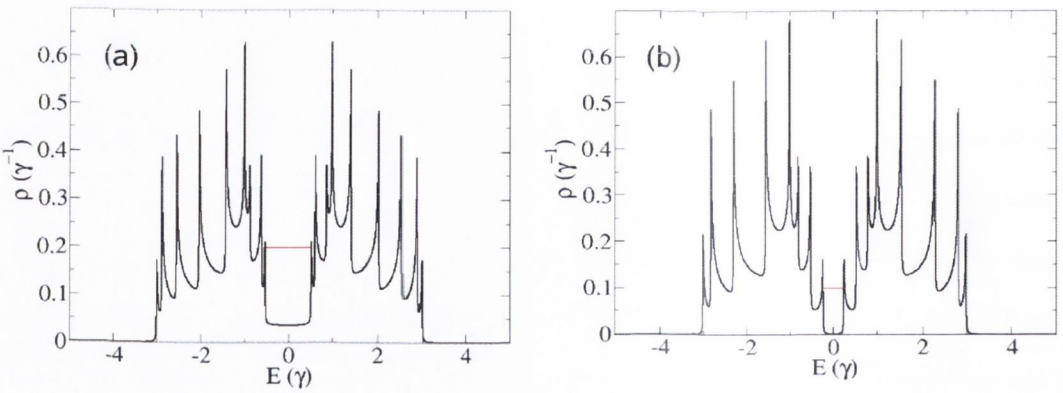

Figure 1.3: Density of states per atom for two different achiral nanotubes as calculated within the zone-folding approach (see the text). (a) Corresponds to an (8,2) chiral nanotube, while (b) corresponds to a (6,2) nanotube. The red lines indicate the distance between the first van Hove singularities above and below the band, known as M_{11} transitions in the case of metallic tubes and S_{11} transitions in the case of the semiconducting. As per the zone-folding theory, (a) has $m - n = 6$ and is metallic , while (b) has $m \neq n \bmod 3$ and is semiconducting. The parameter γ has the dimensions of energy, and has a value of about 2.7eV.

gap ($m = n \bmod 3$, $m \neq n$), or semiconducting with a diameter dependent gap ($m \neq n \bmod 3$). The tiny gap, which is opened when $m = n \bmod 3$, vanishes if the curvature of the tube is neglected. Such is the case in the so-called zone-folding approach, where we extract the electronic structure of a nanotube from that of graphene through the imposition of suitable boundary conditions. In contrast, pristine armchair nanotubes remain conducting, even when a non-isotropic electronic hopping is used. These predictions have been borne out by experiments which show that about 2/3 of single walled nanotubes behave as semiconductors, in line with theory [8]. The DOS for two chiral nanotubes, calculated within the zone-folding approach, is displayed in Fig. 1.3. Besides from the absence or presence of an energy gap between the conduction and valence bands, another characteristic feature of the band structure of these quasi-one-dimensional systems is the so-called van Hove singularities. These features were originally elucidated in the elastic structure of crystals, and are a general feature of the single particle DOS in low dimensional systems [9]. These refer to the clearly observable spikes in the DOS in Fig. 1.3, and

have been observed experimentally through the investigation of the local density of states through the use of scanning tunnelling microscopy [10]. Within the zone-folding approach, the van Hove singularities can be viewed as the energies at which the lines of allowed reciprocal lattice vectors are tangent to the appropriate iso-energy surface of the underlying graphene sheet.

It has been shown that carbon nanotubes can display quantised conductance [11], which is due to circumferential confinement of the wavefunction. Electronic transport within metallic carbon nanotubes is essentially ballistic over distances large compared to the nanoscale, meaning that they can carry high currents with little heating over such distances, with the primary source of resistance in these tubes coming from a contact resistance due to the interface with macroscopic electrodes. Due to imperfections transport over longer distances becomes diffusive. As regards the mobility for nanotubes in the diffusive regime (a quantity that determines how easily the carriers can be induced to drift by the application of an electric field), reports indicate mobilities greater than that of any other semiconductor [12].

1.3.2 Mechanical properties

Another area of interest is the superlative mechanical properties of nanotubes. Nanotubes possess extremely high Young's moduli. The Young's modulus is conventionally defined as the initial slope of a stress-strain curve. One problem with defining the Young's modulus of a single walled nanotube is that it is a hollow cylinder. Since the definition of the stress requires the area over which a force acts, it would seem that the Young's modulus may be ill-defined. On the other hand, the surface area of a bundle of nanotubes is indeed a well-defined quantity. By performing experiments to ascertain the modulus of bundles, the results can be normalised by the number of nanotubes in the bundle, to yield a Young's modulus for an individual tube. Experiments on bundles have led to reported Young's modulus values for *individual nanotubes* of between 320 GPa and 1470 GPa [13]. By way of comparison,

theory says that the Young's modulus of a small diameter SWNT should be of the order of 1000 GPa (which is roughly the in-plane tensile modulus of graphite) [14], but should decrease as the diameter increases. Nanotubes also have exceptional strength. Composites made with nanotubes have been shown to have exceptional toughness, defined as the total energy to break. By way of a reference, it is useful to compare this value with the Young's modulus of steel, which is commonly quoted as being about 200 GPa.

1.3.3 Thermal Properties

Due to the strength of the sp^2 and sp^3 bonds that carbon can form, materials based on it are found to have excellent thermal properties. While graphite itself is extremely good at transporting thermal currents, it is a different allotrope of carbon that is best in class; diamond. Experiments on diamond at *room temperature* show a thermal conductivity of the order of 3000W/mK [15], and orders of magnitude higher at cryogenic temperatures. Recent experimental investigations into the thermal conductivity of individual freely suspended (multi-walled) nanotubes [16] find a diameter-dependent thermal conductivity of about 2000W/mK, which is comparable with, if somewhat lower than, the value of about 3000W/mK which has previously been reported for multi-walled tubes [17]. These values are to be compared with early theoretical predictions [18] of conductivity of about 6500W/mK for single walled nanotubes; recent calculations [19] indicate such high values of thermal conductivity may only be the case for nanotubes with lengths of the order of tens of micrometers. This high thermal conductance has led to nanotubes being proposed as components in devices which produce a lot of heat, with the aim of using them as connections between the hot device, and a thermal sink.

1.4 Nanotubes in composite structures

In this section, I will briefly detail some of the results of investigations performed with the aim of integrating nanotubes into useful structures. As we have seen, theory and experiment have shown that carbon nanotubes are a promising candidate for a next generation material due to their remarkable intrinsic traits. To maximise the utility of these remarkable structures, they must however be combined with other structures. For example, if nanotubes are to be used as transistor elements, they must make contact at the tips of the tubes with macroscopic metallic electrodes. If a bad contact is made, the intrinsic resistance of the transistor can be dwarfed by the contact resistance at the interface. Since the interaction with other substances can crucially determine the usefulness of nanotube-based devices, it is natural to question how it will be possible to integrate nanotubes with existing materials to form composite structures. As a sidenote, in this work, I will often use the word composite in its most general sense to refer to a combination of nanotubes and other structures, which maintains the distinct morphology of the nanotubes.

1.4.1 Utilising mechanical properties

One particularly promising area of application for carbon nanotubes is as fillers in carbon nanotube/polymer *composites*. A *polymer* strand is a macromolecule, which consists of covalently bonded elementary units, called monomers, which bind together to form a chain [20]. Organic polymers have a sp^2 hybridised backbone of carbon atoms, with different polymers having different groups of atoms bonded to the backbone. Typically polymers form a tangled mess, due to interactions between different monomers. Experiment has shown that such polymers readily form composites with nanotubes [21, 22]. Typically in such composites, up to a few percent by volume of carbon nanotubes are added to a polymer matrix with the aim of enhancing its physical properties. For instance, it is well known that polymers are

typically poor electrical conductors, since they suffer a Peierls distortion which destroys their conductivity. However, the addition of a small quantity of nanotubes can increase the electrical conductivity of the sample, with the resulting increase in the conductivity being normally explained through percolation theory [23].

Another area where nanotubes promise an improvement over the pure polymer is in the realm of mechanical reinforcement. When we think of polymers, we tend to think of their macroscopic realisation in the form of plastics, so called because of their plasticity. It is not surprising then, that polymers tend to form bulk aggregates that are mechanically weak. However, it is found that the addition of small quantities by volume of the far stronger and stiffer carbon nanotubes to a polymer sample can greatly affect the mechanical properties of the composite material. It is often desired that such changes be made using minute quantities, in order not to adversely affect those properties of the polymer that we find desirable (such as malleability). One of the major successes to day in the field is that new composite materials with world-record toughness (defined as the total energy a material can absorb before structural failure) have been synthesized, leading to the prospect of light-weight protective textiles, which may find application as light-weight bulletproof vests [24].

As far as the elastic properties of composites are concerned, a number of theoretical tools are used to model the effect of nanotube loading. One of the tools is the so-called rule of mixtures, which is used in macroscopic physics and in engineering to predict the mechanical properties of a composite material made from different species. This relation formula is found experimentally to overestimate the Young's modulus of the composite in the case of multi-walled carbon nanotubes. This has been attributed to a low load being carried by the inner tubes inside the multi-walled tubes, due to sliding of the inner layers relative to the outer layers [25]. However, as pointed out in [21], the same experimental observations may be attributable to poor *stress transfer* across the polymer / nanotube interface, as opposed to across the interface between different sheets of the multi-wall. Understanding, and indeed

quantifying, the interfacial stress transfer between a polymer / nanotube interface is an open topic which may be crucial for further improvements in the properties of composites.

With regard to the morphology of composites it has been reported that certain polymers, such as polyvinal-alcohol (PVA) and PmPV, crystallize about carbon nanotubes which are loaded into a polymer matrix. Transmission electron microscopy reveals a substantial ordered layer of polymer that surrounds the multi-wall nanotubes [26]. Such a coating has been linked with the observed strength increase when Young's modulus experiments are performed on multi-wall / PVA composites [27], in contrast with reports of substantially smaller strength increases when a polymer which does not crystallize, poly(9-vinyl carbazole), is used.

Furthermore, when certain polymers bind to carbon nanotubes in a crystalline coating, it is often observed that they bind in a helical geometry [26]. The helical pitch does not seem to be random – preferential coiling angles for different nanotube/polymer system have been observed. A simple, classical model based on geometric considerations [28] sought to explain the existence of spontaneous chiral order in such structures by examining the balance between the coiling induced stress in a wrapping molecule and the surface dependent affinity such molecules have. Indeed, this fact has been proposed to be a central element of a scheme to separate carbon nanotubes by chirality and electronic properties [29].

1.4.2 Nanotubes in electronic devices

At the time of writing, the material of choice for the semiconductor industry is silicon, as it has been for decades. In order to get more and more transistors onto a given size wafer of silicon requires that the components be shrunk, smaller transistors leading to faster computer chips. However, the components cannot be shrunk indefinitely. In recent years, much attention has been focused on the field of molecular electronics, first proposed in the 70s, partly due to improvements in characterisation

techniques. The basic idea of molecular electronics is to replace the current bulky transistors with small molecules which are capable of emulating their characteristics. This may provide a possible alternative to the current miniturization schemes employed by the semiconductor industry. In fact, it has been proposed that the underlying properties of nanotubes may allow them to play a role in this budding domain. The combination of the existence of semiconducting nanotubes with their reported high mobility seems to make them ideal candidates for constituents of transistors. Indeed, some of the most exciting early experiments on nanotubes showed the ability of nanotubes to act as device elements [30], [31].

Another promising applications for nanotubes is as nanoscale sensing devices. One remarkable feature of carbon nanotubes (NT) is that their conductance is strongly affected by the interaction with certain foreign objects (FO). Atoms, molecules and nanoparticles are some of the objects known to interact strongly with NT, paving their way to being used as nanoscopic sensors. Nanotubes have been shown to experience large changes in their resistance upon exposure to oxygen [32], nitrogen dioxide and ammonia [33]. In this light it may be possible to utilise the properties of nanotubes to generate selective sensitive nanoscale devices. A recent review of the nascent field of carbon-based electronics has appeared in [34], while a more general treatment of the electronic transport properties of nanotubes has recently appeared in [35].

1.5 The crucial role of control

Perhaps the biggest problem facing those who wish to utilise the tantalising properties of nanotubes is their sheer variability. Nanotubes can be single-walled, double-walled and multi-walled. In a multi-walled tube, the different layers are isomorphic to the walls of a single walled nanotube. Since there is a definite relationship between the diameter of the tube and its chirality, and the various walls of the multi-wall

must have different diameters, it is clear that many different chiralities must be present in the same tube. Bearing in mind the decisive influence that the chiral indices have on the electronic structure of a nanotube, we see that in principle some of the walls of the nanotube will be conducting and some not (under the assumption that the different walls don't interact with each other). If we take as a rule of thumb that one third of single walled nanotubes are metallic, we see the difficulty in finding a semiconducting multi-wall tube.

Even if we are able to restrict ourselves to considering only single walled nanotubes, we still run into problems. While nanotubes of very small chiral indices are not found since they are energetically unstable, there is still a plethora of different chiral indices that are allowed. The problem is that for a useful technological device, there is often call for a certain chirality of nanotube. For example, a metallic nanotube will not be a useful component where the need is for a semiconducting one. Current manufacturing methods allow only a poor control over the chiral indices of the nanotubes in a sample. While there can be some control over the spread of diameters that are grown in a sample [36], since there exist semiconducting and metallic tubes with similar diameters, this does not give you control over the metallicity of a sample.

Furthermore, just as successive layers of graphene in graphite are attracted via van der Waals forces, so exists a similar nanotube-nanotube interaction. The effect of this attraction is that nanotubes tend to aggregate into what are called bundles, which consist of a collection of coaxial nanotubes in close proximity to each other. This is a serious issue for those who want to use nanotubes in devices. Usually, applications call for the components of the device to possess certain properties. Seeing as each of the tubes in the bundle may possess different properties, and bearing in mind that the interaction with nearby structures is capable of altering these properties, it is clear that isolated nanotubes are preferred for applications to those in bundles. The lack of knowledge of how to breakup these bundles without

causing damage to the tubes or irreversibly altering their properties in some way is, as of now, one of the most fundamental barriers to the commercial exploitation of nanotubes.

On the other hand, if the nanotube experiences a dramatic dependence on its environment, it may be possible to control its properties through controlling what is in its vicinity. For example, it has been shown that the conductance of a nanotube can be strongly altered by letting oxygen adhere to its surface [32]. We will often refer to such an interaction as a doping process, by analogy with the conventional definition of the term. By far the most dramatic success of doping in technology, and in the sciences, is in the addition of foreign species to pure semiconductors to increase the number of possible electrical current carriers, a crucial step in the manufacture of modern logic devices. Since a semiconductor is characterised by an energy gap between the conduction and valence electrons, a non-trivial amount of energy must be added to the material in order to promote some electrons to the conduction band in order to allow an electrical current to flow. However, the introduction of atoms of a different valence into the crystal introduces free carriers that can dramatically increase the conductance of the material. If such extrinsic control could be exerted over nanotubes, it could overcome deficiencies in as-grown samples, and provide a path towards their integration in technological devices.

1.6 The desire for a general formalism

In the light of the foregoing discussions, it is clear that a theoretical understanding of the doping process for carbon nanotubes is highly desirable, and the elucidation of a framework capable of accounting for the changes induced is one of the main aims of this work.

As things stand, the interaction between carbon nanotubes and foreign objects is usually treated by performing two separate studies: one which addresses what

conditions a foreign object will bind to a nanotube, and one which investigates the effects that this interaction brings to the electronic properties of the device. Typically, the first step is performed by utilising *ab-initio* calculations to provide the energy change that occurs when the foreign object adheres to the nanotube, while the second considers the conductance of the structure in the presence of a finite concentration of dopants. To take into account a disordered array of molecules on the surface of a nanotube, an ensemble average must be performed. Since we have to average over a large number of configurations computationally expensive *ab-initio* evaluations are unattractive, and so parameterised semi-empirical Hamiltonians are often used. Besides from the large demand on computational resources this puts, one reason this approach is dissatisfying is a lack of mathematical transparency in the first part; the *ab-initio* calculation is treated as a "black-box", and the chance to make general statements about the binding process can be lost.

What form would an alternative approach take? There are undoubtedly certain characteristics that we would desire a calculational framework to possess, so it is worth spelling out in detail what properties such a formalism should have. First and foremost, the scheme utilised must provide an accurate reflection of what happens in nature. If the method is unable to reproduce accurately the properties of hybrid structures, it must be rejected. The scheme should be able to not only tell under what circumstances that binding will take place, but also be capable of accounting for changes in the physical properties of the system. While ab-initio calculational schemes such as density functional theory set the standard for accuracy, it is at a steep price in terms of computational resources, particularly if we wish to model disordered systems. With this in mind, we would wish that the scheme should be capable of giving quantitatively accurate values for those properties that are of interest, but should be less intensive in terms of resources. Seeing as there is a huge range of possible dopants of interest, ideally the scheme should be able to treat a wide variety of disparate doping entities under the same framework. Since the

introduction of a foreign object naturally destroys the translational invariance of the unperturbed system, the methodology must be capable of calculating quantities in direct space; however, since we would also like to be able to treat certain periodic perturbations, it is desired that the scheme be extendable to utilise the Bloch theorem and work within a supercell representation.

Lloyd's formula method (LFM) provides one candidate for such a formalism which meets the criteria above. This scheme utilises mathematical rules which express induced changes in the density of states in terms of the properties of the *isolated* subsystems and the coupling between the parts to calculate physical properties of interest; it will be one of the main tools used in this thesis. As well as the fact it is capable of meeting the criteria outlined above, another point in favour of the LFM is that it utilises Green Function (GF) techniques. The usefulness of GF (see Appendix A) techniques lies in the fact that the density of states of a system is intimately related to the trace of the GF. Green functions can be used in disordered systems; GF methods need not rely on the existence of translational symmetries of the system. Since the process of adding a dopant to a carbon nanotube breaks translational symmetry, using GF methods can avoid the need for a supercell representation. Furthermore, within the LFM, we are free to choose whichever electronic structure model is most suited to the problem at hand.

For instance in the case of nanotubes the functional form for the zone-folded Green function matrix elements in real space is well known [37], so it may be attractive to work with this choice of basis set. If, however, it becomes clear that a more sophisticated choice of electronic structure model is necessary, we are free to use our expressions with this more sophisticated model. In this work, we will work on the basis that the details of the isolated subsystems are well known, and view the configuration of the system after the interaction as the desired unknown.

To summarise, this thesis addresses the problem of theoretically describing the doping process in carbon nanotubes. We aim to introduce a mathematically trans-

parent scheme which allows the extraction of both qualitative and quantitative information about the binding process. Moreover, we intend to adopt a formalism which allows the treatment of a diverse range of dopants without major modifications. As such we will apply this method to a range of dopants of interest, such as atoms and small molecules, to investigate the properties of the combined structures so formed.

1.7 Layout of the thesis

In order to enhance the readability of this work, I will here give details of the layout of the remainder of this thesis, which is composed of six chapters. The next chapter will serve to introduce the mathematics and concepts that will be needed to investigate changes induced in the electronic structure of a *general system* due to the introduction of a contact potential. This gives me an opportunity to provide a detailed exposition of the general formalism, which will be the primary goal of the chapter. I will then use to illustrate how the mathematical clarity of the expressions permits the derivation of certain analytical results. Chapter Three will utilise the general formalism presented in Chapter Two, and will be specific to the case of atoms and small molecules adhering to the surface of metallic nanotubes. In this chapter, we will show how it is possible to show correlations between the charge transfer between the parts and the electronic contribution to the binding energy. Furthermore, we will investigate the dependence of the correlation on the details of the atomic structure of the adsorbed atom. We will show how it is possible to utilise the afore-mentioned sum rules to extract details about the detailed structure of the coupling between the parts.

In the fourth chapter, we will consider the case where the perturbing entities are no longer simple molecules, but are polymer strands or DNA molecules, which we view as one dimensional charge distributions. In this chapter we perform calculations that suggest the possibility that a helical ordering may be an energetically favourable

structure, irrespective of the underlying chiral order of the host nanotube. We will also perform calculations to investigate how the changes induced in the electronic structure of the system depend on details such as the strength of the coupling perturbation, the width of the perturbing strand, and indeed the angle at which the one dimensional charge distribution coils.

In the fifth chapter, we will change emphasis somewhat, and focus on an attempt to understand the mechanical properties of non-covalently bonded composites. To this end, we will utilise a simple classical model for the structure of both the nanotube and the coiling polymer, which nonetheless suffices to investigate the interface between the nanotube and the embedding matrix. A possible mechanism for reinforcement in such systems is proposed, and a diameter dependence of the reinforcement is predicted. The final chapter will contain summary and conclusions, and propose further work that can build on my research.

Chapter 2

The Lloyd Formula Method

2.1 Motivation and layout

In order to understand, and ultimately to predict the physical properties of doped carbon nanotubes, it is desirable to have a theoretical formalism based on which these properties can be evaluated. When a system with known properties is perturbed by an external potential, its electronic structure is affected in a way which is reflected by changes in its global density of states. Those physical properties of the system that are directly governed by the total density of states will consequently change. Likewise, a number of ancillary quantities such as total energy, conductance, and occupation, to name but a few, will also be modified. This suggests that a study of how doping impacts on the physical properties of a composite material should include a description of how the total density of states changes in response to such a perturbation.

In this work we are interested in developing a method that is capable of describing the necessary transformation in the density of states in a mathematically transparent fashion. Such a mechanism already exists, and relies on the existence of certain sum rules for changes in the single-particle Green functions induced by an external perturbation. These sum rules provide a simple operator equation that

relates changes in the total density of states to matrix elements of both the Green function of the isolated system and the perturbation matrix itself. It is one goal of this work to adapt this existing formula in such a way that suits the study of doped carbon nanotubes.

For the sake of clarity, it is worth describing the layout of ideas in this chapter. Lloyd's formula in its general form, which gives information about the global density of states of the structure in terms of the Green function of the unperturbed system and a perturbative potential will be introduced in the first section. This will then be adapted to take into account the specific geometry relevant to nanotube doping. We do this by deriving a closed form expression for the variation in the total density of states appropriate to the interaction between initially disconnected sub-systems that are allowed to come into contact. The remainder of the chapter investigates the consequences of the adapted formula, and indicates some uses to which it can be put. Calculations based on the mathematically straightforward case of a perturbed linear chain will be presented for illustration purposes.

2.2 Canonical form of Lloyd's formula

Extensive use has been made of Lloyd's formula in this work. This equation allows one to calculate the change in the total density of states due to a perturbation, and as such is useful in the modeling of doped materials. Initially introduced in the 1960s [38], it has found extensive use in multiple scattering theory, and has recently been put on a rigorous mathematical footing by Zeller [39]. Despite its extensive use in a wide variety of systems since its original derivation, it has only recently been applied to the case of low dimensional systems such as nanotubes. In the last few years it has been used to model the contact induced potential between magnetic atoms and non-magnetic substrates [40] [41], as well as in the study of magnetic coupling between impurities in metallic systems [42] and in nanotubes [37]. Other

uses include modeling of the physical properties of disordered alloys [43].

In its canonical form Lloyd's formula can be written concisely as

$$\Delta\rho(\omega) = \frac{-2}{\pi}\frac{\mathrm{d}}{\mathrm{d}E}\mathrm{Im}\left(\mathrm{Tr}\left(\log(\hat{1} - \hat{g}(E)\hat{V})\right)\right)\Big|_{E=\omega}. \tag{2.1}$$

Here, $\hat{g}(E)$ is the single-particle Green function of the total Hamiltonian before the perturbation is introduced, while $\hat{1}$ is the identity operator. $\hat{V}$ is the perturbation Hamiltonian; it is necessary that this be independent of energy. We will refer to $\hat{1} - \hat{g}(E)\hat{V}$ as the Lloyd matrix. A formal derivation of this expression is included in Appendix B of this thesis. The log function maps linear operators into linear operators according to the definition

$$\log\left(\hat{1} - \hat{g}\hat{V}\right) = -\hat{g}\hat{V} - \frac{\hat{g}\hat{V}\hat{g}\hat{V}}{2} - \frac{\hat{g}\hat{V}\hat{g}\hat{V}\hat{g}\hat{V}}{6} - \cdots \tag{2.2}$$

which echoes the familiar definition of the Log function via the Laurent series for complex numbers [44].

Taking the trace of the logarithm for each energy produces a complex number which makes the trace of the logarithm a complex function of energy. Once we take the imaginary part, we have a simple real valued function of energy, which we must then differentiate. The external factor of $\frac{-2}{\pi}$ gives the correct normalisation of this function, and takes into account spin degeneracy. If spin degeneracy is absent, the external factor is $\frac{-1}{\pi}$, but the matrix will have twice as many rows and columns. We will also use a computationally more convenient form of this equation, which takes advantage of the useful relation

$$\mathrm{Tr}\left(\log\left(A\right)\right) = \log\left(\det\left(A\right)\right) \tag{2.3}$$

which holds for a large class of operators with square matrix A (including all that we have considered in this work). Substituting this into Eq. (2.1), we find an alternative

form of Lloyd's formula

$$\Delta\rho(\omega) = \frac{-2}{\pi}\frac{\mathrm{d}}{\mathrm{d}E}\mathrm{Im}\left(\log(\det\left(\hat{1} - \hat{g}(E)\hat{V}\right))\right)\Big|_{E=\omega}. \tag{2.4}$$

While the logarithm may be regarded as a multivalued function of a complex variable, we will treat it as a single-valued function defined on multiple Riemann sheets in the following fashion. Letting $\det\left(\hat{1} - \hat{g}(E)\hat{V}\right) = r(E)e^{i\phi(E)}$, $r(E) > 0, \phi(E) \in \mathbb{R}$ and fixing $\phi(E) \to 0$ as $E \to -\infty$,

$$\log\left(r(E)e^{i\phi(E)}\right) = r(E) + i\phi(E). \tag{2.5}$$

Having presented the necessary mathematics to utilise Eq. (2.4), it is worth emphasizing its physical usefulness. One point in its favour is that the derivation of Eq. (2.4), as presented in the Appendix, includes multiple scattering events of all orders through the use of the full $\hat{T}$ matrix. Another point in its favour is that Lloyd's formula allows one to derive an expression for the change in the number of particles in a system, by performing an elementary integral over energy. Furthermore, a knowledge of the change in the density of states allows the calculation of physically relevant quantities such as the electronic contribution to the total energy. A final point in its favour is that since the expression is in operator form it is *model independent*, in so far as the same expression holds regardless of the choice of Hamiltonian. For the sake of simplicity, we will often use simple models such as the tight-binding model with Eq. (2.4), but we are by no means restricted to this approach; if it is found that the choice of such a simple Hamiltonian is insufficient for accurate calculations, the same expressions will hold with whichever Hamiltonian is necessary.

One alternative to the use of Eq. (2.4) would be to calculate directly the Green function of the composite system by brute-force. In general, this would require the evaluation of the Green function at each site $|i\rangle$ up to a cutoff N. The disadvantage of

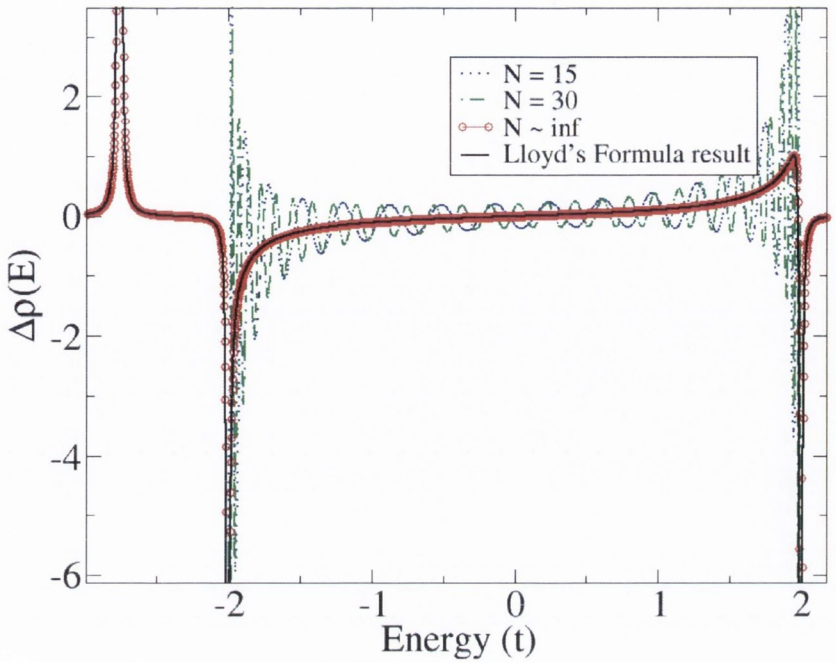

Figure 2.1: Change in the total density of states for a linear chain, whose Hamiltonian is $\hat{H} = \sum_j t|j\rangle\langle j \pm 1|$, subject to a perturbation potential $\hat{V} = \delta_0|0\rangle\langle 0|$, as calculated within the tight-binding model. Different curves refer to different cutoff radii for the brute-force approach (see the text). Here N is the distance from the perturbation site at which cutoff occurs. The continuous black curve (as per Lloyd's formula) agrees with the limit $N \to \infty$ (red circles). In this example $\delta_0 = -1.9t$.

this approach is that the calculation of the composite Green function is a numerically expensive operation which must be done for a large number of sites, due to a large cutoff radius. The need for a large cutoff radius is due to the fact that perturbations tend to have long-ranged effects in low-dimensional systems. This is illustrated in Fig. 2.1, where we display how the results converge on the Lloyd formula result in the case of a diagonal perturbation of a linear chain. While not unexpected, it is worth emphasizing that Eq. (2.4), as evidenced by the continuous black curve, reproduces *exactly* the converged change in density of states, as shown by the red circles.

Another approach would be to directly evaluate the eigenvalues of the Hamiltonian. However, a localized perturbation will destroy the translational symmetry, stopping the wavenumber k from being a good quantum number. Bloch's theorem

cannot then be applied, and in principle the evaluation of the eigenvalues and eigenstates must be done in real space for an infinite dimensional matrix. The standard procedure to get around this in most *ab-initio* calculations is to include periodic repetitions of the perturbation through the use of a supercell. While the size of the supercell is chosen as large to reduce the interaction between impurities within adjacent unit cells, the exact result is only achieved in the limit $L \to \infty$.

In contrast, as shown in Appendix C, to utilise Lloyd's formula in the case of a localized perturbation, we need only work with sub-matrices which involve only those matrix elements connecting states involved in the binding. When combined with the simplicity with which the electronic structure of nanotubes can be described, this method seems to be a promising way of describing the doping process in nanotubes.

2.3 Modeling doping via contact potentials

When a system of known electronic structure is perturbed, the change in the total density of states engenders changes in a number of ancillary quantities (such as electronic binding energy). Here our interest lies in establishing a simple mechanism that allows us to obtain this change in a mathematically transparent way. To this end, we have specialised Eq. (2.4) to deal with the change in the total density of states which occurs when two initially isolated subsystems are allowed to come into contact. We typically label the two subsystems by the indices O (for the *host*) and A (for the *adsorbate*). A schematic of the situation is presented in Fig. 2.2. While this use of language may suggest that the method is applicable only to the case of adsorbed molecules on surfaces, this is not the case; however this will be the most common usage in this work. Usually I will take the host be a single walled carbon nanotube, and the adsorbates to be adatoms, adsorbed small molecules or adsorbed polymers. However this is not the limit of applicability; indeed the contrasting (and yet related) case of substitutional defects can also be addressed within the same

scheme.

Before the interaction, the electronic characteristics of *isolated* subsystems are governed by a total Hamiltonian $\hat{h}$. In the case of an adsorbate, the Hamiltonian before interaction can be written as the sum of the Hamiltonians of the isolated subsystems:

$$\hat{h} = \hat{h}_0 + \hat{h}_A \tag{2.6}$$

where h_0 refers only to the host, while h_A refers only to the adsorbate. If the Hilbert space of states of subsystem O has basis $\{|o_1\rangle, |o_2\rangle, \cdots\}$ and that of subsystem A has basis $\{|a_1\rangle, |a_2\rangle, \cdots\}$ then the Hilbert space of the combined system is assumed to have basis $\{|o_1\rangle, |o_2\rangle, \cdots, |a_1\rangle, |a_2\rangle, \cdots\}$. Such a scheme is well-known from the familiar linear combination of molecular orbitals method, in which the aforementioned states correspond the molecular orbitals of the isolated subsystems. Often, as far as the nanotube is concerned, we will assume that the set of states corresponding to the carbon $|p_z\rangle$ states of graphene will suffice to describe the electronic structure of the nanotube, since these are the states that lie closest to the Fermi level. With reference to Fig. 1.1, we can make the identification $\{|o_1\rangle, |o_2\rangle, \cdots\} = \{|\vec{R}_1, A\rangle, |\vec{R}_1, B\rangle, \cdots\}$, where it is understood that $|\vec{R}_1, A\rangle$ corresponds to the p_z orbital localized about the carbon atom of type A located in the supercell at position $\vec{R}_1$. Furthermore, unless explicitly stated, we will assume that all basis states are orthonormal; this is a reasonably good approximation in the case carbon nanotubes, especially if one is concerned only with the electronic structure *up to* the Fermi level.

In the particular case of a contact potential, we assume that only the states $\{|o_1\rangle, |o_2\rangle, \cdots, |o_n\rangle\}$ (corresponding to those sites in the green region of Fig. 2.2) and $\{|a_1\rangle, |a_2\rangle, \cdots, |a_m\rangle\}$ (corresponding to those sites in the purple region of Fig. 2.2) are involved. In other words, we assume that $\hat{V}|o_i\rangle = \langle o_i|\hat{V} = \hat{V}|a_j\rangle = \langle a_j|\hat{V} = 0$ if $i > n, j > m$. In this case, we can formally write down a perturbation Hamiltonian of the form

$$\hat{V} = \hat{\Delta}_0 + \hat{\Delta}_A + \hat{\Gamma} + \hat{\Gamma}^\dagger. \tag{2.7}$$

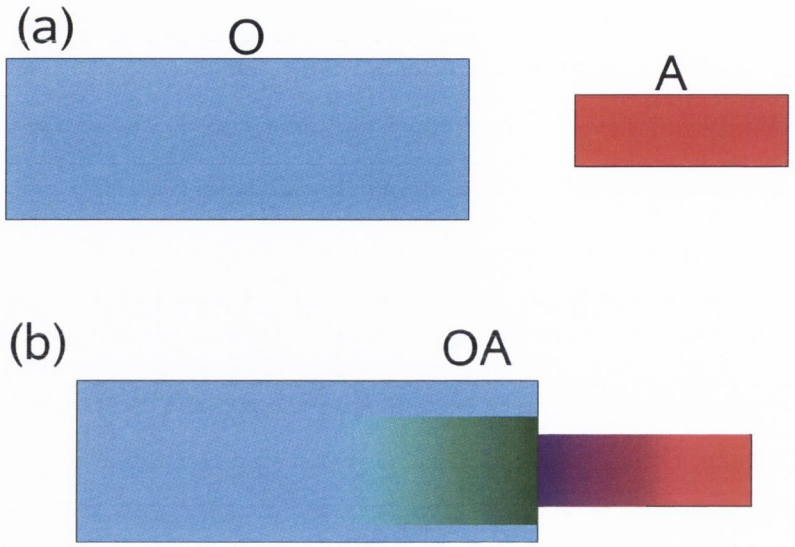

Figure 2.2: Schematic representation of host and adsorbed dopant (a) before and (b) after a contact interaction. Only matrix elements corresponding to sites in the vicinity of the contact are perturbed. The green area denotes the region in sub-system O where the contact induced perturbation is non-zero, while the purple region plays the corresponding role for sub-system A.

Here, the first term corresponds only to changes localized on the system O; the second term corresponds to changes located on system A; while the two remaining terms are responsible for coupling the two initially disconnected systems together. With a tight-binding like Hamiltonian in mind, $\hat{\Delta}_0$ will include any changes to onsite energies for atoms in region O, as well as any induced changes in hopping-integrals between states in O; $\hat{\Delta}_A$ performs an identical role for sub-system A; and $\hat{\Gamma}$ and its Hermitian conjugate directly couple a state from O with one in A. Changes in onsite potentials may be induced by a polarization interaction, while changes in couplings within either system A or O may be necessitated by geometrical rearrangement of atoms. It is worth emphasizing that each of these terms in principle acquires both a multi-site and multi-orbital matrix character, which may also include spin degrees of freedom.

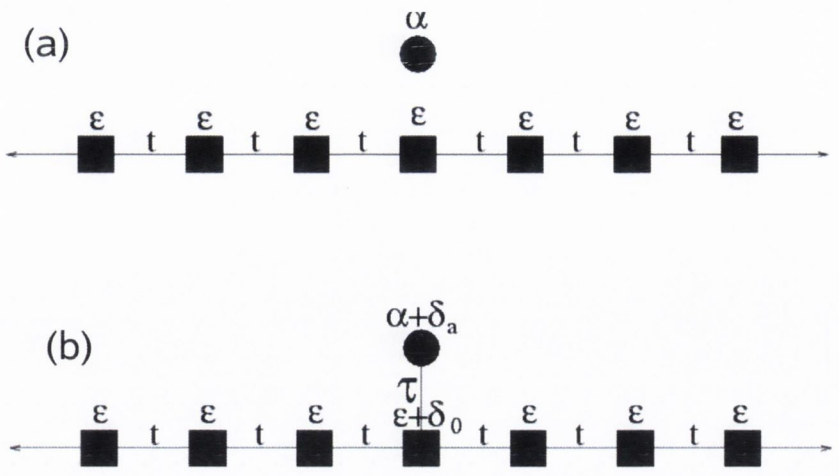

Figure 2.3: Linear chain characterized by onsite ϵ and hopping integral t plus adsorbed single level impurity with characteristic eigenvalue α. Graphical display of tight-binding parameters both (a) before and (b) after the systems are allowed to interact. Within the efficient screening hypothesis (see the text) only those sites on the chain nearest to the atomic impurity undergo a correction to their onsite.

2.4 Using Lloyd's formula: a case study

2.4.1 Linear chain with adsorbed impurity

By way of an introduction to Lloyd's formula, I now present the example of the linear chain perturbed by an adsorbed single level atomic dopant. This pedagogical system may serve as a simple model for interaction between carbon nanotubes and isolated adsorbed impurities. In common with the nanotube, the linear chain is a one-dimensional system, and in the absence of the inclusion of a Peierls distortion is metallic (as are approximately one third of nanotubes). One advantage of this system is that it has a particularly simple Green function (as do the π-bands of nanotubes) that allows us a degree of mathematical transparency. A schematic of the unperturbed system is displayed in Fig. 2.3a, while Fig. 2.3b displays the system after the perturbation.

One of the simplest models for the electronic properties of a solid is the linear chain of identical atoms. The linear chain consists of an infinite sequence of identical

orbitals $|j\rangle$, separated by common distance a, representing atoms bonded together into a long molecule. In the nearest neighbour approximation, the Hamiltonian of the chain is determined by just two characteristic energies ϵ and t, and the total Hamiltonian is given as

$$\hat{H} = \sum_j \epsilon |j\rangle\langle j| + \sum_j t(|j\rangle\langle j+1| + |j\rangle\langle j-1|), \tag{2.8}$$

where j runs over all the sites of the molecule. The eigenvalues of this Hamiltonian are obtained using Bloch's theorem; the corresponding band structure is displayed in Fig. 2.4a.

As far as this work is concerned, we take as an effective definition of the Green function at energy E of a system governed by Hamiltonian $\hat{h}$ the expression

$$\hat{g}(E) = \lim_{\eta \to 0^+} (\hat{1}(E + i\eta) - \hat{h})^{-1}, \tag{2.9}$$

where $i\eta$ is a small positive imaginary number which ensures that the Green function is well defined.

It can be shown that the real space Green function elements for the linear chain are

$$\langle j|\, \hat{g}\, |j'\rangle = g_{00} . e^{-ik_0|j-j'|}, \tag{2.10}$$

where $\cos k_0 = \frac{E+i\eta-\epsilon}{2t}$ and $g_{00}(E) = \frac{i}{2t \sin k_0(E)}$. There are two distinct values of k_0 that satisfy the given equation: they a re negatives of each other. The only one which lies inside the integration contour, and hence by Cauchy's theorem will contribute, is the one with a negative imaginary part. This ensures the selection of the retarded Green function, one matrix element of which is plotted in Fig. 2.4b.

As regards the electronic structure of the isolated atomic impurity, we must specify the position of its energy levels. One way of doing this is to identify the

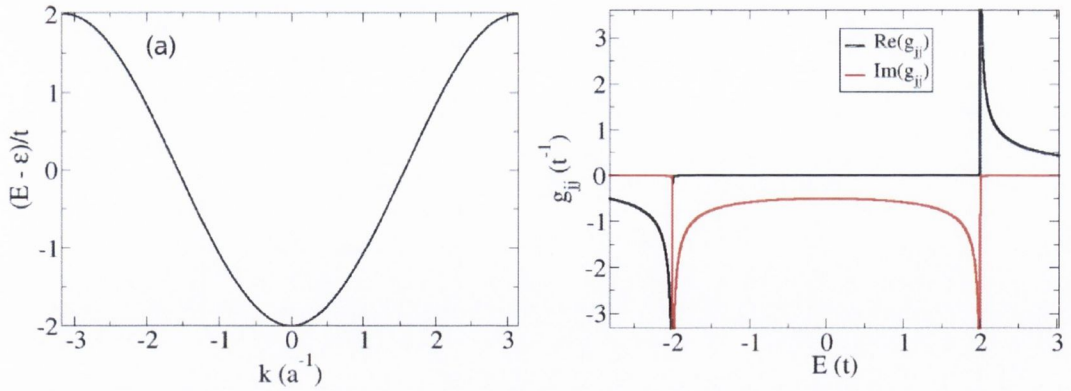

Figure 2.4: (a) Tight-binding band structure of the unperturbed linear chain in the nearest neighbour approximation. The bandwidth is seen to be 4t, and is centred at $E = \epsilon$. (b) Real and imaginary parts of the Green function $\langle 0|\, \hat{g}\, |0\rangle$ of the linear chain. The Green function is seen to be pure imaginary inside the band.

ionization potential (U_I) of the atom (the energy that must be added to the atom to excite its highest energy electron sufficiently to a scattering state). Under the assumption that we can identify a common vacuum level with the host, for whom the work function (W) plays the role equivalent to the ionization potential, we can make the identification that $\alpha = W - U_I$. The relative position of α, E_F and the rest of these parameters is schematically depicted in Fig. 2.5. However, to characterize the atomic impurity we must also give information about the occupancy of that level; we denote the number of particles on the site a in the absence of the perturbation as C_0.

2.4.2 The Lloyd Formula Method

An investigation of the linear chain plus adsorbed single level impurity provides the opportunity to introduce what will be hereafter referred to as the *Lloyd's formula method* (LFM). The utility of the LFM lies in the crucial role that the density of states plays in determining the physical properties of electronic systems. In particular, knowledge of *the change* in the density of states allows the direct calculation of *changes* in global properties of the system, such as the total energy of the sys-

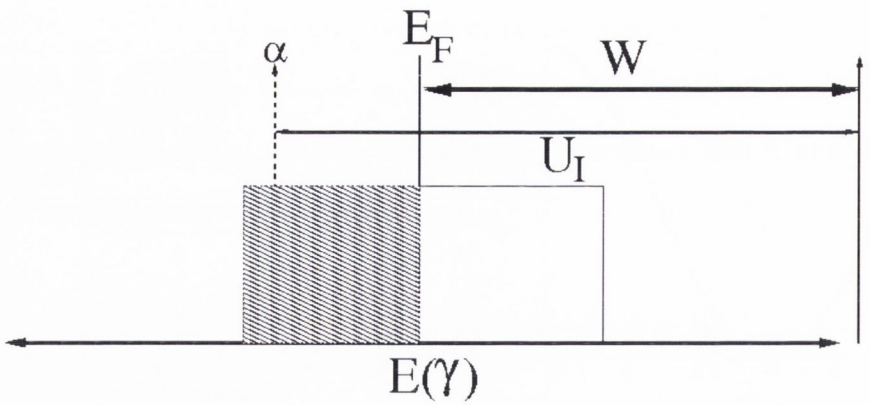

Figure 2.5: Schematic representation of the electronic structure of the unperturbed system. The host is represented by a half-filled band, while the single level is denoted by a delta function. Here W is the work function of the host, E_F its Fermi level and α is the energy level of the isolated impurity which has ionization potential U_I. The relation between the characteristic energies is displayed, which leads to the effective definition $\alpha = W - U_I$.

tem. Combined with the fact that knowledge of the Green function of the composed system allows direct evaluation of the local density of states at each site, a set of non-linear equations can be derived that allows direct evaluation of measurable properties of the system in terms of the elements of the perturbation matrix.

To model the interaction, we allow the initially isolated atom to interact directly with that chain atom at location $j = 0$. The interaction Hamiltonian displayed in Eq. 2.7 in this case specialises to

$$\hat{V} = \delta_0|0\rangle\langle 0| + \delta_a|a\rangle\langle a| + \tau|a\rangle\langle 0| + \tau^*|0\rangle\langle a|, \tag{2.11}$$

where δ_0, δ_a and τ are no longer matrices but now simple scalars. Here δ_0 reflects a change in the electrostatic environment at the site 0; δ_a a corresponding change on the atomic impurity; and the hopping integral τ couples the atomic level directly to site 0 and reflects the possibility of transfer of particles between the parts. In principle, there is no reason that the only onsite on the chain to be altered by the presence of the polarizing entity should be the one which is closest to it, and in general it will not be, as discussed earlier. On the other hand, it is reasonable to

assume that those sites which are closest to the nearest point of contact should be affected the most, since it is a well known characteristic of a metallic system that the charge density of the metal can change in such a way as to screen out extraneous electric fields. While this ability is somewhat suppressed in low-dimensional systems, for the sake of simplicity we will initially assume that the only onsite on the chain that is affected by the interaction is that of the site closest to the impurity. This presumption will later be referred to as the *efficient screening hypothesis*; we will subsequently have to relax this and deal with finite-sized screening clouds when we are considering the case of nanotube-adatom interaction, and wish to compare with *ab-initio* calculations.

In the case at hand, the rank of the perturbation matrix is $n = 2$. In line with what has been outlined thus-far, we must form the 2×2 matrix of Green functions. The Green function of the unperturbed linear chain is given by Eq. (2.10) while the Green function of the bound orbital has a particularly simple form:

$$g_{aa} = \frac{1}{E + i0^+ - \alpha} \tag{2.12}$$

The cross terms g_{0a} and g_{a0} both vanish, since the atomic level is initially disconnected from the host. It is straightforward to show that in the case of the linear chain / adsorbed impurity system, the determinant of the Lloyd matrix is $1 - \delta_0 g_{00} - \delta_a g_{aa} + g_{00} g_{aa} (\delta_0 \delta_a - |\tau|^2)$.

In the light of the foregoing, I now show how a set of non-linear equations can be derived that show the relation between the parameterisation of the perturbation and some quantities that depend on changes in the density of states, in the case that there is initially C_0 electrons with energy α on the doubly degenerate atomic level $|a\rangle$.

2.4.3 The charge neutrality condition

As previously mentioned, the Lloyd formula equations allow us to investigate the increase in the number of particles ΔN due to the presence of the interaction in a mathematically transparent fashion. We consider the linear chain as the host (labelled O) and the dopant as an isolated doubly spin-degenerate single level impurity (labelled a). We assume that the isolated level is characterized by an energy α, and the host is characterized by onsite parameter ϵ and hopping γ. Initially, we assume that $\alpha < E_F$ and that the isolated atomic level is occupied by C_0 particles ($C_0 = 0, 1$ or 2). We allow the atom to come into contact with the chain, and model this interaction by the previously presented perturbation Hamiltonian, as displayed in Eq. (2.11).

Before the parts are allowed to interact, there are C_0 electrons on the atom. The variation in the number of particles due to perturbation, ΔN, is naturally defined as

$$\Delta N := N_{0a} - N_0 - N_a, \tag{2.13}$$

where N_a and N_0 are the initial number of electrons on the adsorbate and the chain respectively, and N_{0a} is the number of particles in the touching system. Due to the fact that the linear chain has in principle an infinite number of sites, this expression contains two numbers that are divergent: N_{0a} and N_0. Concerns about such divergences can be dealt with by considering these quantities in the case of a very long, but not infinite chain. We can then formally form a sequence ΔN_n of values corresponding to the change in number of particles when the chain is of length n atoms. We then put $\Delta N = \lim_{n\to\infty} \Delta N_n$. In this fashion, similar concerns about quantities such as binding energies can also be addressed.

The total number of particles in the system *before* interaction is:

$$N_{before} = C_0 + \int_{-\infty}^{E_F=\epsilon} \mathrm{d}E \; \rho_0(E). \tag{2.14}$$

Since the isolated level is doubly degenerate, and $\alpha < E_F$, we have

$$\int_{-\infty}^{E_F} \mathrm{d}E\ \rho_a(E) = 2 \tag{2.15}$$

$$\Rightarrow \int_{-\infty}^{E_F} \mathrm{d}E\ \rho_a(E) - C_0 = 2 - C_0 \tag{2.16}$$

$$\Rightarrow C_0 = -(2 - C_0) + \int_{-\infty}^{E_F} \mathrm{d}E\ \rho_a(E). \tag{2.17}$$

This expression can be substituted back in to Eq. (2.14) to yield:

$$N_{before} = -(2 - C_0) + \int_{-\infty}^{E_F} \mathrm{d}E\ (\rho_{NT}(E) + \rho_a(E)). \tag{2.18}$$

The number of particles after the interaction is simply given as

$$N_{after} = \int_{-\infty}^{E_F} \mathrm{d}E\ \rho_{tot}(E), \tag{2.19}$$

so the change in the number of particles that results from the introduction of perturbation $\hat{V}$ is

$$\begin{aligned} \Delta N = N_{after} - N_{before} &= (2 - C_0) + \int_{-\infty}^{E_F} \mathrm{d}E\ (\rho_{tot}(E) - \rho_{NT}(E) - \rho_a(E)) \\ &= (2 - C_0) + \int_{-\infty}^{E_F} \mathrm{d}E\ \Delta\rho(E) \end{aligned} \tag{2.20}$$

In this fashion we can write the change in the total number of particles in terms of the change in the global density of states. In the case of the linear chain perturbed by an adsorbed adatom, we can use Lloyd's formula to write

$$\Delta N = (2 - C_0) - \frac{2}{\pi} \int_{-\infty}^{E_F} \mathrm{d}E\ \frac{\mathrm{d}}{\mathrm{d}E} \mathrm{Im}\left(\log\left(1 - g_{00}\delta_0 - g_{aa}\delta_a + g_{00}g_{aa}(\delta_0\delta_a - |\tau|^2).\right)\right) \tag{2.21}$$

Here the external factor of 2 takes into account the different spin channels.

We can pull the "Imaginary part" past the derivative, as the derivative of the

imaginary part is the imaginary part of the derivative, and indeed past the integral, as we are integrating along the real axis, and hence the differential is pure real. So

$$\Delta N = (2 - C_0) - \frac{2}{\pi}\mathrm{Im}\left(\int_{-\infty}^{E_F} \mathrm{d}E \, \frac{\mathrm{d}}{\mathrm{d}E}\log(1 - g_{00}\delta_0 - g_{aa}\delta_a + g_{00}g_{aa}(\delta_0\delta_a - |\tau|^2))\right), \tag{2.22}$$

Applying the fundamental theorem of calculus,

$$\Delta N = (2 - C_0) - \frac{2}{\pi}\mathrm{Im}\left(\log\left(1 - g_{00}\delta_0 - g_{aa}\delta_a + g_{00}g_{aa}(\delta_0\delta_a - |\tau|^2)\right)\right)_{-\infty}^{E_F}. \tag{2.23}$$

The vanishing of the Green function at arbitrarily large negative energies leads to

$$\Delta N = (2 - C_0) - \frac{2}{\pi}\,\mathrm{Im}\left(\log\left(1 - g_{00}\delta_0 - g_{aa}\delta_a + g_{00}g_{aa}(\delta_0\delta_a - |\tau|^2)\right)\right)\Big|_{E_F}. \tag{2.24}$$

Before I move onto the derivation of the next of our equations, I wish to point out one consequence of Eq. (2.24): since allowing two systems to touch cannot change the number of particles in our system, we must demand that $\Delta N = 0$. For this reason, Eq. (2.24) has been referred to as the *charge neutrality equation*. We see that this demand imposes a constraint on the three parameters $(\delta_0, \delta_a, \tau)$

$$\begin{aligned} (2 - C_0) &= \frac{2}{\pi}\,\mathrm{Im}\left(\log\left(1 - g_{00}\delta_0 - g_{aa}\delta_a + g_{00}g_{aa}(\delta_0\delta_a - |\tau|^2)\right)\right)\Big|_{E_F} \\ \Rightarrow \frac{\pi}{2}(2 - C_0) &= \mathrm{Im}\left(\log\left(1 - g_{00}\delta_0 - g_{aa}\delta_a + g_{00}g_{aa}(\delta_0\delta_a - |\tau|^2)\right)\right)\Big|_{E_F}. \end{aligned} \tag{2.25}$$

2.4.4 Electronic contribution to the binding energy

Bearing in mind the preceding discussion on how we will treat quantities that are formally divergent, we can write down immediately a formula for the electronic contribution to the binding energy, defined here as the difference in electronic energy

between the final and initial configurations

$$E_{before} = -(2 - C_0)\alpha + \int_{-\infty}^{E_F} \mathrm{d}E \;\; E(\rho_0(E) + \rho_a(E)). \tag{2.26}$$

The total electronic energy after interaction is

$$E_{after} = \int_{-\infty}^{E_F} \mathrm{d}E \; E \; \rho_{tot}, \tag{2.27}$$

so the total change in electronic energy is given as

$$\begin{aligned} \Delta E &= (2 - C_0)\,\alpha + \int_{-\infty}^{E_F} \mathrm{d}E \; E \; \Delta\rho \\ \Rightarrow \Delta E &= (2 - C_0)\,\alpha + \frac{2}{\pi} \int_{-\infty}^{E_F} \mathrm{d}E \; E \; \mathrm{Im}\left(\log\left(1 - g_{00}\delta_0 - g_{aa}\delta_a + g_{00}g_{aa}(\delta_0\delta_a - |\tau|^2)\right)\right). \end{aligned} \tag{2.28}$$

In Eq. (2.28) we have the second of our LFM equations. It constitutes a second constraint on the values of the parameters $(\delta_0, \delta_a, \tau)$.

2.4.5 Charge transfer to adsorbed atom

Thus far, we have successfully established two relations between the microscopic parameters of the perturbation and a few physical observables. Even if these were linear equations (they are not), we would have an under-determined system of equations. However, a third constraint can be imposed by considering the variation in the number of electrons on the atomic site due to the perturbation, as I now show.

The charge on the atomic site is given as the integral of the local density of states up to the Fermi level. This can in turn be written in terms of the Green function of the composed structure as

$$C_{after} = \frac{-2}{\pi} \int_{-\infty}^{E_F} \mathrm{d}E \; \mathrm{Im}\,(G_{aa}) \tag{2.29}$$

where, as usual, $G_{aa} = \langle a| \hat{G} |a\rangle$ is the relevant matrix element of the Green function for the connected system. The site originally had C_0 electrons on it, so the increase in the number of particles on the site is given as

$$\Delta C = -C_0 + \frac{-2}{\pi} \int_{-\infty}^{E_F} \mathrm{d}E \ \mathrm{Im}\left(G_{aa}\right). \tag{2.30}$$

It can be shown that in the case of a simple adsorbed atomic impurity (see Appendix D), this expression becomes

$$\Delta C = -C_0 + \frac{-2}{\pi} \int_{-\infty}^{E_F} \mathrm{d}E \ \mathrm{Im}\left(\frac{g_{aa}(1 - g_{00}\delta_{00})}{1 - g_{00}\delta_{00} - g_{aa}\delta_a + g_{00}g_{aa}(\delta_{00}\delta_a - |\tau|^2)}\right) \tag{2.31}$$

It is worth emphasizing that while this expression does not utilise Lloyd's formula, it complements it, and allows us to write down three equations in terms of three unknowns. One final point is that the integration involved in Eq. (2.31) will usually have to be performed numerically. In this case, it is often useful to perform the integration in the complex plane. In fact, such an approach is often of use in evaluating Eq. (2.28), where it can be of use in avoiding any complications due to occasional crossings of branch-cuts. The details of such a transformation are displayed in Appendix E.

2.4.6 Uses of the formalism

If we were to choose a triple of parameters at random $(\delta_0, \delta_a, \tau)$, and plugged them into Eqs. (2.28) and (2.31), we would certainly be able to calculate values for the electronic contribution to the binding energy ΔE, and to the increase in the number of electrons on site a, ΔC. This would raise the question whether such an arbitrary choice of parameters leads to a physically allowed configuration. Bearing in mind the charge neutrality condition, Eq. (2.24), we would strongly suspect not. In fact, in the next section, I derive analytical expressions for the constraints on the

triple $(\delta_0, \delta_a, \tau)$ that narrow down the allowed configurations. Such analysis is only possible due to the particularly simple nature of the perturbation potential, and a similar analysis would be much tougher (or at least more tedious) in the case of imperfect screening. However, even in this case, we see that all constraints can be implemented numerically.

To illustrate the numerical implementation of this point, I consider a singly occupied atomic level $\alpha < E_F$, bound to a linear chain. In light of the constraint Eq. (2.24), we postulate δ_a and δ_0, and we allow τ to vary from 0 to an energy far higher than any other characteristic of the problem. For each value of τ we record the value of the change in the number of particles, $\Delta N(\delta_0, \delta_a, \tau)$. Since we have a closed system, the number of particles is a constant, and the perturbation must respect this constraint. If, for a given pair (δ_a, δ_0) it is not possible to find a value of τ such that $\Delta N = 0$, we conclude that such a perturbation represents an unphysical situation and reject it. In Fig. 2.6 we plot a typical function $\Delta N(\tau)$ as a function of the single parameter τ. Here $\epsilon = 0$, $t = 1$, $\alpha = -0.75$, $\delta_0 = -0.40$ and $\delta_a = 0.30$. It is seen that for asymptotically large values of τ (compared to the other microparameters) we have the destruction of one half of one electron. We also see how it is possible to graphically solve this equation to get a unique value for τ that will satisfy charge neutrality. Of course, choosing different values of δ_0 and δ_a will give different values of ΔC and ΔE. In particular, both δ_a and δ_0 may assume values that are inconsistent with the charge neutrality condition; this is illustrated in Fig. 2.7.

In this simple system, we can see that different values of δ_0 and δ_a lead to different values for $(\Delta C, \Delta E)$. It is instructive to follow the map from the "parameter space" (different values of the microstructure parameters) into the "observable space" (different values of the binding energy and the charge transfer). Such a diagram is plotted in Fig. 2.8. The entire unit disk in the δ_a–δ_0 plane was probed, but only a section of the lower half plane is filled in. All other states in the unit disk do not

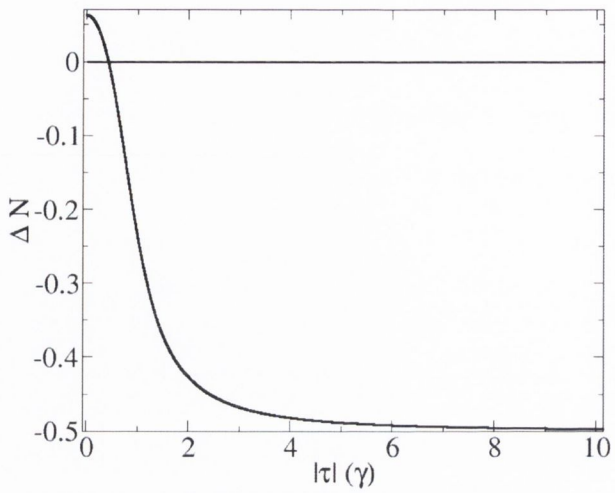

Figure 2.6: Characteristic dependence of the change in the number of particles when a single level impurity binds to a linear chain according to the Hamiltonian in Eq. 2.11, as a function of the microstructure parameter τ. Here $\epsilon = 0$, $t = 1$, $\alpha = -0.75$, $\delta_0 = -0.40$ and $\delta_a = 0.30$. The horizontal line indicates the charge neutrality condition, which is met for $|\tau| = 0.42$.

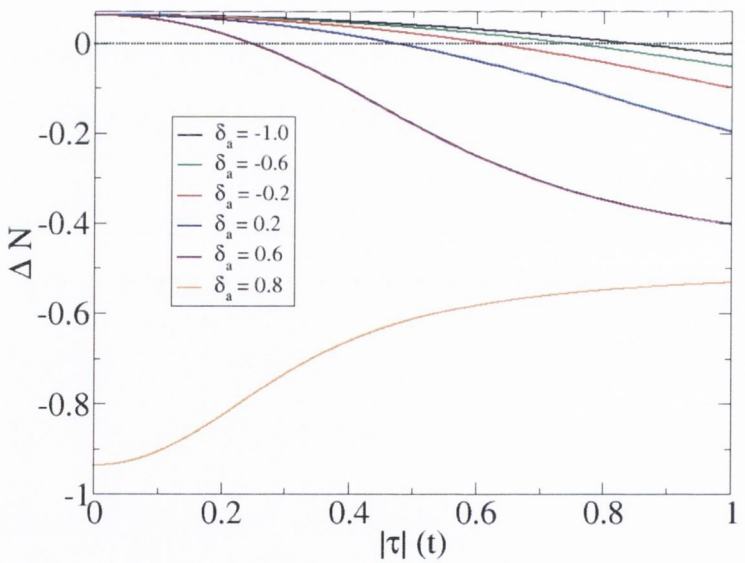

Figure 2.7: Characteristic dependence of the change in the number of particles when a single level impurity binds to a linear chain according to the Hamiltonian in Eq. 2.11, as a function of the microstructure parameter τ. Here $\epsilon = 0$, $t = 1$, $\alpha = -0.75$ and $\delta_0 = -0.40$. The dotted line indicates the charge neutrality condition, which can be met for $\delta_a < 0.75$. Larger values would move the atomic level above the Fermi level.

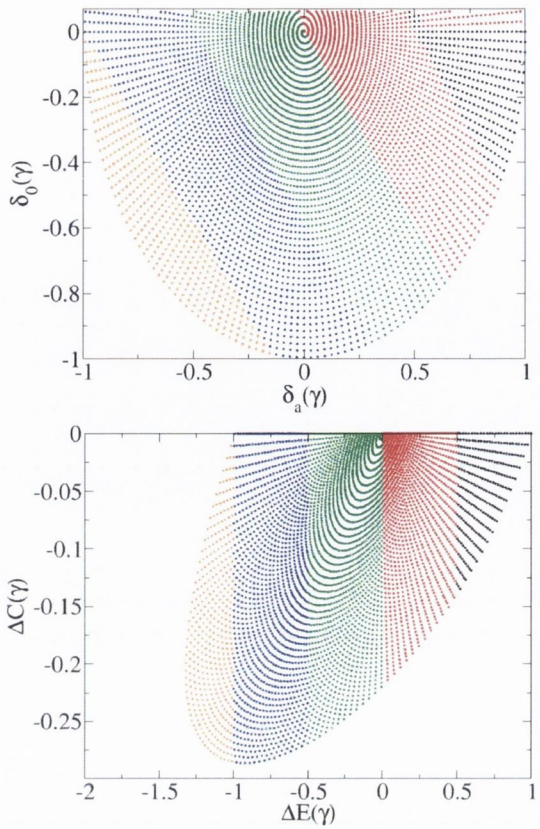

Figure 2.8: Plot of the mapping from the parameter space to the observable space for the case of an adsorbed impurity with $\alpha = -2.5$ bonded to an infinite linear chain ($t = 1, \epsilon = E_F = 0$). Regions of the same colour map into each other. In particular, we see that the green, blue and orange coloured sets correspond to configurations with a negative binding energy.

respect charge neutrality, and thus are disregarded. Such diagrams will be further developed in the next chapter where they will be introduced as $\Delta E - \Delta C$ diagrams, and will be instrumental in extracting information on the interaction between nanotubes and atoms. In this case the host will no longer be a simple linear chain, but rather a metallic nanotube. In the case of the linear chain, we can see that for those values that convergence occurs, that the map is one-to-one.

2.5 Analytic Investigation of the LFM equations

One of the advantages of the LFM as presented is the apparent analytical clarity of the expressions involved. In this section, I demonstrate some of the uses to which this clarity can be put. The first will concern some results derivable from the charge neutrality equation, while the second will be concerned with the physically important case of weak binding between the parts. While the results here presented are for the case of a single level impurity on a linear chain, these results are directly of use in the study of adatoms bound to metallic nanotubes; this is due to the similarity between the Green functions of the linear chain and of armchair nanotubes.

2.5.1 Analysis of the charge neutrality condition

As in the previous sections, we again consider an adsorbed single level impurity on a linear chain. In this case, it is possible to investigate analytically some of the consequences of the charge neutrality equation, as displayed in Eq. (2.25). To do this, I assume that $\alpha < E_F$, and treat separately the cases with different values of C_0.

Case: $C_0 = 1$

If $C_0 = 1$, the LHS of Eq. (2.25) is $\pi/2$. By the properties of the logarithm function, this means that the argument of the logarithm must lie along the positive imaginary axis. Let this number be $r\,i$, where $r > 0$ is a real positive number.

Then

$$ri = 1 - g_{00}\delta_0 - g_{aa}\delta_a + g_{00}g_{aa}(\delta_0\delta_a - |\tau|^2). \tag{2.32}$$

We can now use a fundamental property of the Green functions of the linear chain and that of the isolated atom: the Green function matrix element of the linear chain is purely imaginary at the Fermi level, while that of the atomic level is purely real (this fails when $\alpha = E_F$, a case we will not treat). We can equate real and imaginary

parts of this equation to give two constraints. Firstly, by equating the real parts

$$\begin{aligned} 0 &= 1 - g_{aa}|_{E=E_F}\,\delta_a \\ \Rightarrow \delta_a &= \frac{1}{g_{aa}} \end{aligned} \tag{2.33}$$

which can be seen to be the same as $\delta_a = E_F - \alpha$. On the other hand, equating the imaginary parts gives

$$ri = -g_{00}\delta_0 + g_{00}g_{aa}(\delta_0\delta_a - |\tau|^2)\big|_{E=E_F} \tag{2.34}$$

We can use the first constraint in this new equation to yield

$$\begin{aligned} ri &= -g_{00}\delta_0 + g_{00}g_{aa}(\delta_0\frac{1}{g_{aa}} - |\tau|^2)\Big|_{E=E_F} \\ \Rightarrow ri &= -g_{00}g_{aa}|\tau|^2\big|_{E=E_F} \end{aligned} \tag{2.35}$$

which can be rewritten as $|\tau|^2 = -\frac{ir}{g_{00}(E_F)g_{aa}(E_F)}$. This second equation makes sense for all positive values of r, since $g_{00}(E_F)g_{aa}(E_F)$ is a negative imaginary number, and so the second constraint gives us no new information. For each pair $r > 0$ and $\delta_0 \in \mathbb{R}$, we can find a solution of the above form to the charge neutrality condition. This solution can then be used as the appropriate tight-binding parameters to calculate the charge transfer and the electronic contribution to the binding energy. In this fashion, we can consider τ and δ_0 to be independent parameters, calculate $\delta_a(\tau, \delta_0)$, and then generate a $\Delta E - \Delta C$ diagram, as described in the previous section.

Case: $C_0 = 0$

If $C_0 = 0$, the LHS of Eq. (2.25) is π; as such, the determinant must lie on the negative real axis (note that we can place the branch-cut of the logarithm on the

negative imaginary axis to avoid unnecessary complications). So

$$-r = 1 - g_{00}\delta_0 - g_{aa}\delta_a + g_{00}g_{aa}(\delta_0\delta_a - |\tau|^2), \qquad r > 0. \tag{2.36}$$

Equating real parts:

$$r = g_{aa}(E_F)\delta_a - 1. \tag{2.37}$$

Since $g_{aa} > 0$ (as the level lies below E_F) this is only possible for $\delta_a > \frac{1}{g_{aa}}$.

Equating imaginary parts gives

$$0 = -g_{00}\delta_0 + g_{00}g_{aa}(\delta_0\delta_a - |\tau|^2)\big|_{E=E_F}. \tag{2.38}$$

$g_{00} \neq 0$, so

$$\begin{aligned} \delta_0 &= -g_{aa}(E_F)(\delta_0\delta_a - |\tau|^2) \\ \Rightarrow \delta_0(1 + g_{aa}(E_F)\delta_a) &= g_{aa}(E_F)|\tau|^2 \\ \Rightarrow \delta_0 &= \frac{g_{aa}(E_F)|\tau|^2}{1 + g_{aa}(E_F)\delta_a}. \end{aligned} \tag{2.39}$$

In order to interpret Eqs. (2.37) and (2.39) we note that since $g_{aa} > 0$ (as the level lies below E_F) Eq. (2.39) can only hold for $\delta_a > \frac{1}{g_{aa}}$. So $\delta_0 > 0$. Considering the second constraint we note that the RHS of Eq. (2.39) involves only positive terms. So, given $|\tau|^2 > 0$, we can pick $\delta_a > \frac{1}{g_{aa}}$, and calculate uniquely $\delta_0(\tau, \delta_a)$. Negative δ_0 are not allowed. The triple can then be placed into the Lloyd equations, to yield values for ΔE and ΔC, with the guarantee that $\Delta N = 0$.

Case: $C_0 = 2$

If $C_0 = 2$, the LHS of Eq. (2.25) vanishes; the determinant must lie on the positive real axis. So equating the real part gives

$$r = 1 - g_{aa}(E_F)\delta_a, \qquad r > 0. \tag{2.40}$$

while equating the imaginary part

$$\delta_0 = \frac{g_{aa}(E_F)|\tau|^2}{1 + g_{aa}(E_F)\delta_a}. \tag{2.41}$$

Again, these results require interpretation. Since $r > 0$, Eq. (2.40) can hold only if $1 - g_{aa}(E_F)\delta_a > 0$, or $g_{aa}(E_F)\delta_a < 1$. So we have the constraint

$$\delta_a < \frac{1}{g_{aa}}. \tag{2.42}$$

Given $|\tau|^2 > 0$, we can pick $\delta_a > \frac{1}{g_{aa}}$, and calculate uniquely $\delta_0(\tau, \delta_a)$. Since the numerator of Eq. (2.41) can take arbitrarily large values, and the denominator can take on both positive and negative values, all values of δ_0 are allowed, as computed according to Eq. (2.41).

2.5.2 Weak binding in the Lloyd formula method

The second piece of analytical information that can be extracted from the LFM equations involves the case of weak binding. It is often the case that we will encounter weak binding between the subsystems. Such may be the case for noble gas atoms bound to the surface of nanotubes, for example. Another example may be in the case of a polarizing interaction characterised by a small binding energy. In this case, we expect that the micro-structure parameters δ_0, δ_a, τ will be small (having magnitude $\ll 1$). So we can investigate approximations to $\Delta\rho$ and ancillary quantities. Intuitively, we expect that if the combined system is characterised by given physical property P, while the combined isolated systems are characterised by property P_0, $P \to P_0$ as $(\delta_a, \delta_0, \tau) \to (0, 0, 0)$.

For example, consider the case where P is the total electronic energy and consider

$\Delta P = P - P_0$:

$$\begin{aligned}\Delta P &= \frac{2}{\pi}\left[\int_{-\infty}^{E_F} \mathrm{Im}\left(\log\left(1-\delta_0 g_{00}-\delta_a g_{aa}+g_{00}g_{aa}(\delta_0\delta_a-|\tau|^2)\right)\right)\right. \\ &\left. -\int_{-\infty}^{E_F} \mathrm{Im}\left(\log\left(1-\delta_0 g_{00}\right)\right)-\int_{-\infty}^{E_F} \mathrm{Im}\left(\log\left(1-\delta_a g_{aa}\right)\right)\right].\end{aligned} \tag{2.43}$$

By the property of logs, we have

$$\begin{aligned}\Delta P &= \frac{2}{\pi}\int_{-\infty}^{E_F} \mathrm{Im}\left(\log\left(\frac{1-\delta_0 g_{00}-\delta_a g_{aa}+g_{00}g_{aa}(\delta_0\delta_a-|\tau|^2)}{(1-\delta_a g_{aa})(1-\delta_0 g_{00})}\right)\right) \\ &= \frac{2}{\pi}\int_{-\infty}^{E_F} \mathrm{Im}\left(\log\left(1+\frac{g_{00}g_{aa}(\delta_0\delta_a-|\tau|^2)}{1-\delta_a g_{aa}-\delta_0 g_{00}+\delta_a g_{aa}\delta_0 g_{00}}\right)\right).\end{aligned} \tag{2.44}$$

If $g_{aa}g_{00}$ is small, this term tends to zero as $(\delta_a, \delta_0, \tau) \to (0,0,0)$.

On the other hand, for energies where $g_{aa}g_{00}$ is large, this term is

$$\Delta P \sim \frac{2}{\pi}\int_{-\infty}^{E_F} \mathrm{Im}\left(\log\left(1+\frac{(\delta_0\delta_a-|\tau|^2)}{\delta_a\delta_0}\right)\right). \tag{2.45}$$

But all the terms in the argument of the Logarithm are real, so $\Delta P \sim 0$. In other words, as $(\delta_a, \delta_0, \tau) \to (0,0,0)$, we have

$$\begin{aligned}\int_{-\infty}^{E_F} \mathrm{Im}\left(\log\left(1-\delta_0 g_{00}-\delta_a g_{aa}+g_{00}g_{aa}(\delta_0\delta_a-|\tau|^2)\right)\right) \to \quad & \int_{-\infty}^{E_F} \mathrm{Im}\left(\log\left(1-\delta_0 g_{00}\right)\right) \\ & +\int_{-\infty}^{E_F} \mathrm{Im}\left(\log\left(1-\delta_a g_{aa}\right)\right)\end{aligned} \tag{2.46}$$

Bearing in mind the formulae established for the change in electronic energy, for weak binding, we may write

$$\Delta E \to -(2-C)\alpha + \Delta E_a + \Delta E_0 \tag{2.47}$$

where $\Delta E_a = \frac{2}{\pi}\int_{-\infty}^{E_F} \mathrm{Im}\left(\log\left(1-\delta_a g_{aa}\right)\right)$ is related only to changes on the atom, and $\Delta E_0 = \frac{2}{\pi}\int_{-\infty}^{E_F} \mathrm{Im}\left(\log\left(1-\delta_0 g_{00}\right)\right)$ refers only to changes on the perturbed atom on the chain. In fact, we can go further; there is a general result that states that for a square matrix X with small entries we have the formula

$$\begin{aligned} \det\left(1-X\right) &\simeq 1-\mathrm{Tr}\left(X\right) \\ \Rightarrow \log\left(\det\left(1-X\right)\right) &\simeq -\mathrm{Tr}\left(X\right). \end{aligned} \tag{2.48}$$

In this fashion, we can approximate the Lloyd formula determinant in the case of the adsorbed linear chain as

$$\log\left(1-\delta_0 g_{00}-\delta_a g_{aa}+g_{00}g_{aa}(\delta_0\delta_a-|\tau|^2)\right) \quad -\delta_0 g_{00}-\delta_a g_{aa} \tag{2.49}$$

Integrating up to the Fermi level gives

$$\begin{aligned} \Delta E &= \alpha(2-C_0)+\frac{2}{\pi}\int_{-\infty}^{E_F}\mathrm{Im}\left(\log\left(1-\delta_0 g_{00}-\delta_a g_{aa}+g_{00}g_{aa}(\delta_0\delta_a-|\tau|^2)\right)\right) \\ &\sim \alpha(2-C_0)+\frac{2}{\pi}\int_{-\infty}^{E_F}\mathrm{Im}\left(-\delta_0 g_{00}-\delta_a g_{aa}\right) \\ &\sim \alpha(2-C_0)+\delta_0+2\delta_a \end{aligned} \tag{2.50}$$

This gives an approximate expression for the change in the binding energy as calculated using the LFM. We see that the change is approximately linear in both δ_0 and δ_a. Also, since τ appears only to second order, to first order ΔE is independent of τ.

2.5.3 Linear Chain with substitutional impurity as a limiting case of the adsorbed one

The substitutional impurity on a linear chain is modeled by the particularly simple perturbation Hamiltonian

$$\hat{V} = \delta_0 |0\rangle\langle 0| \tag{2.51}$$

In this case, the rank of the perturbation matrix is 1, and the Lloyd matrix is a simple scalar, identical to its determinant, $\det_s$:

$$\det_s = 1 - \delta_0 g_{00}. \tag{2.52}$$

In the limit of weak coupling, we have seen that quantities such as the binding energy can be approximated as being allocatable to each of the parts separately. In this fashion, if we are concerned primarily with changes induced in the host in the limit of weak coupling, and we neglect any induced changes in the dopant, we see that we can approximate the Lloyd determinant of the adsorbate-host system as $1 - g_{00}$, which is equivalent to the expression for a substitutional impurity.

Use will be made of this observation in Chapter 4, where we treat a polarizing polymer wrapping around a nanotube by considering only its effect on the nanotube, while neglecting any influence the nanotube has on the polymer.

2.6 Conclusions

In this chapter I have introduced a number of concepts that will be of use in the investigation of the properties of doped carbon nanotubes. One of the main thrusts of this chapter is to provide a detailed introduction to the *Lloyd formula method*, a calculational scheme that has been used throughout this thesis. I have used the linear chain model for a one dimensional metal to illustrate the concepts; I have introduced the $\Delta E - \Delta C$ diagram for a given dopant and shown how to generate it in the case of

the linear chain. We see how it can be used in two distinct ways: in the "forward" direction we can use knowledge of the detailed structure of the perturbation we can evaluate quantities such as changes in the local charge density and the binding energy. On the other hand, I have shown that under certain circumstances, it is possible to draw a bijection between the parameter space and the observable space. Accordingly, it is possible to utilise a knowledge of the physical properties of the system to derive appropriate values of the elements of the perturbation matrix. In fact, as will be discussed in the next chapter, such a scheme has already been implemented to provide values of the elements of the perturbation matrix in the important case of impurities binding to carbon nanotubes. In the final part of the chapter, I have performed investigations into the analytical expressions utilised in the Lloyd formula method, and included explicitly contributions due to charge on adatoms. This allowed me to show the existence of general constraints on the allowed combinations of microstructure parameters. While these results have been derived in the pedagogical case of the linear chain, due to the mathematical similarity between the Green function of the nanotube and that of the linear chain, similar results may be utilised in the study of changes induced in the electronic structure of nanotubes by bound adatoms.

Chapter 3

Applications of the general method

3.1 Introduction

3.1.1 Motivation

The use of carbon nanotubes (CN) as components in functional electronic devices is currently a primary focus of the research community and is primarily driven by the miniaturisation strategies of the electronics and computer industries. Hopes run high that nanotubes may prove useful as nanoscale interconnects [45] and even as transistor elements [46]. Such a strategy requires an understanding of transport properties of nanotube-based materials, in order to control them. One route to achieve this is to tune the conductivity of the sample through controlled doping processes. Such a scheme has indeed been the backbone of the conventional semiconductor industry for many years [47, 48]. Substitutional impurities, chemisorbed and physisorbed adatoms, nanoparticles and molecules are some of the examples that have already been considered as possible doping agents for nanotubes, both on the experimental and theoretical fronts [49, 50, 51, 52].

The experimental achievements in this field have indeed been outstanding. To

take one example, nitrogen-doped CNs have been carefully synthesised; these were subsequently characterised by scanning tunnelling spectroscopy [53]. Regarding the doping effect on the transport properties, a strong n-type donor state near the Fermi level was identified as being primarily responsible for altering the conductance of the doped structure from that of the clean structure, in good agreement with theoretical predictions [53]. As regards using nanotubes in actual devices, field-effect transistors with an n-type current have been produced by doping carbon nanotubes with randomly dispersed potassium atoms [54]. Furthermore, the ability to change the conductance of a nanotube exposed to dispersed gaseous molecules is stimulating the research to build extremely sensitive devices capable of detecting minute concentrations of specific substances. The idea here, succinctly, is that if the conductance of a nanotube changes in a manner characteristic of a certain dopant, then the nanotube can be used to check for the presence of such dopants by checking its conductance. Bearing in mind the diversity in the electronic properties of nanotubes of different chirality, and the plethora of different molecules that we may wish to be able to detect, we see the existence of a vast number of different nanotube/dopant systems whose combined electronic characteristics we would like to understand.

As such, it is somehow discouraging that the advances on the computational front have not progressed at a similar pace, mainly due to the large computational complexity of calculations involving doped structures. Whereas modern *ab-initio* techniques based on Density Functional Theory (DFT), which typically scale as the cube of the number of orbitals per unit cell, can achieve a good degree of accuracy to describe the electronic structure of pristine crystalline materials, they are somewhat restricted when dealing with disordered systems. The complexity increase results from the need to include a large number of atoms in the unit cell to investigate disorder, with consequent increased demands both on processor time and on computer memory. For even a limited number of impurity atoms M, the calculation

for the electronic structure of the system, which has N states in the unit cell will typically scale as the cube of this larger number forming an obvious barrier against useful predictions. Typically, today's desktop computers can cope with hundreds of atoms in a given unit cell, with large scale computational research facilities allowing perhaps an order of magnitude increase on this figure. Coupled with the demand to average over a large number of different configurations, to correctly simulate the supposedly random dispersion of dopants over the surface of a nanotube, it is clear that to treat this problem using *ab-initio* methods is a non-trivial task.

In fact, DFT calculations for doped nanotubes have indeed been performed but have always been limited to a very small number of impurities, in order to maintain the low concentration limit. For instance, studies of transition-metal-doped nanotubes investigated their electronic and magnetic properties both in isolation, and in nanotube bundles, but were restricted to a maximum of 3 impurities per unit cell [55]. DFT was again used to investigate the inclusion of Li^+ ions inside nanotubes to assess whether nanotubes could be used as lithium-based batteries; in this case only a single Li atom was considered. Such calculations may give indications of the effects that doping has on certain electronic properties, but as far as the conductance of a doped system is concerned, the limitation to a small number of impurities can be misleading. Multiple scattering events, which naturally reduce the extended character of the electronic wave functions, cannot be fully taken into account if one is restricted to a very few impurities, which suggests that the effect of disorder on the transport properties may be somewhat underestimated in those cases. Even when large unit cells are considered, which in principle allows calculations with an increased number of impurities, the results often bear little statistical significance, since many different configurations are needed to truly represent the statistical ensemble of the disordered system.

The obvious route to overcome this problem is to use less computationally demanding techniques. A combination between tight-binding (TB) methods and *ab-*

initio calculations seems a natural choice. The advantage of this type of combination is in the facility with which one can include scattering effects generated by randomly distributed impurities without major compromises to accuracy. One of the suggested methods for combining the two techniques is by fitting the zone-folded TB band structure to that obtained from DFT calculations [56, 57]. While this is certainly a valid candidate strategy, it may involve fitting eigenvalues above the Fermi energy. Such states do not contribute directly to changes in the ground state energy, which, along with the electronic density, is the quantity known to be the most reliable output in a DFT calculation. Moreover, the fitting may not be unique since it is necessarily dependent on a particular choice of points in the Brillouin zone where the two band structures (the tight-binding and the DFT) must agree.

The somewhat unsatisfactory nature of simple band structure fitting has spurred recent attempts to find an alternative approach. At the time of writing, perhaps the most promising of these is the novel approach taken in [58]. In this work, the authors calculate the transport properties of the disordered system through the use of the Kubo formalism in real space. To do this, they first investigate the effect that a single impurity has on the electronic structure of the doped system by using the SIESTA DFT code. In particular, they parameterise the semi-empirical Hamiltonian used to calculate the transport properties of the disordered configuration, not through the use of band-structure fitting, but rather by directly extracting the value of the induced changes in the onsite potential in the case of an individual impurity.

To the same end, in the next section of this chapter, I suggest another alternative to band structure fitting, which relies on *ab-initio* evaluations for quantities such as the binding energy and the charge transfer, which are subsequently used to provide the appropriate values for the tight-binding parameters. Our scheme is based on the previously introduced Lloyd formula method which relates the change in the total density of states to changes in both the local charge density and in the total energy. By relating all these quantities under a common framework, we can not only obtain

the appropriate tight-binding parameters, but may also see the effects that doping may bring to the physical properties of a nanotube in a transparent fashion.

3.1.2 Layout of this chapter

This chapter, like the next, is essentially divided into two distinct, but yet closely related, parts. The overarching aim of this chapter is to study the interaction between metallic nanotubes and isolated atomic and small molecular impurities, using the Lloyd's techniques that we have developed, and that were introduced in the previous chapter. These techniques are highly efficient in calculating *changes* in the electronic structure, and consequently in calculating those physical properties that are dependent on these changes. One reason for the efficiency of this method it that it can utilise preexisting knowledge of the electronic structure of the isolated parts. Indeed, one of the major advantages in using this method for the systems that we have is the chance to use existing analytic formulae for the Green functions (GF) of armchair and zigzag carbon nanotubes.

The first part of the chapter concerns itself with an exposition of the method for the technologically relevant case of nanotubes which are bound to hydrogen atoms. Relationships between the perturbation Hamiltonian and a number of physical observables, such as the electronic contribution to the overall binding energy (the "electronic binding energy") and the charge transfer between the hydrogen atom and the nanotube are derived. We then use these relationships as input parameters to calculate matrix elements of the perturbation Hamiltonian. For the sake of comparison, we show that the perturbation matrix elements so derived lead to a band structure that bears a striking resemblance to the Kohn-Sham band structure. The final part of the section uses the calculated tight-binding parameters, inside the Kubo formalism, to investigate how the electronic transport characteristics of an armchair nanotube depends on the concentration of randomly distributed hydrogen atoms bound to its surface.

The second part of the chapter moves away from the focus on hydrogen atoms as dopants, and seeks to make general statements about the binding process. Currently, calculations on properties of nanotube / dopant systems are usually performed on an *ad-hoc* basis. That is to say, a certain chirality of nanotube is chosen, a certain species of dopant is chosen, and the properties, such as charge transfer and binding energy, of the combined system are calculated. There are, as of yet, no general guidelines available on which pair (nanotube / dopant) should be chosen, if one wishes to maximise the variation in the physical properties of the system. Since an effective sensor requires large variations to overcome noise, and in light of the usefulness of such a guidelines in the search for a suitable combination that would lead to effective nanoscale sensors, one goal of this work is to implement an *inverse modeling approach* to determine what characteristics a nanotube / foreign object pair must intrinsically possess to make that nanotube a good sensor for that foreign object. To this end, we have looked at the binding between nanotubes and dopants of various different types, such as atoms and some simple molecules. In a similar fashion to Chapter 2, where we showed that the pair ΔE and ΔC were not uncorrelated for the somewhat artificial case of a single level impurity bound to a linear chain, we will show a similar correlation in the case of nanotube / adatom systems through the existence of $\Delta E - \Delta C$ diagrams. When further explored, we show how the use of these $\Delta E - \Delta C$ diagrams can give general guidelines on what properties we should seek in nanotubes and dopants such that a structure composed of these parts will have specified characteristics.

3.2 Modeling the effect of randomly dispersed adatoms on carbon nanotubes

3.2.1 Electronic structure of nanotubes

We start by considering, first, a situation in which a nanotube and a single-atom impurity are initially decoupled. As we shall see, one of the advantages of our method is that it uses information about the electronic structure of the system in its decoupled configuration; this is something which happens to be well known in the case of nanotubes. The decoupled system is described by a Hamiltonian $\hat{H}_0 = \hat{h}_0 + \hat{h}_a$, where $\hat{h}_0$ and $\hat{h}_a$ correspond to the individual Hamiltonians of the tube and the impurity atom, respectively. For the sake of simplicity, we choose to represent the electronic structure of the nanotube by a single π-band Hamiltonian and assume that the states are mutually orthogonal. The π-state is known to be the relevant electronic orbital at the Fermi level, and as such it determines the transport properties of nanotubes. It is worth mentioning that the use of such a simplified Hamiltonian for $\hat{h}_0$ is primarily chosen to ease the presentation of the method and bears no limitation to its applicability. In fact, it is relatively straightforward to generalise the procedure described here to a multi-orbital representation of the nanotube. The Hamiltonian $\hat{h}_0$ is written in operator form as

$$\hat{h}_0 = \sum_i \left[|i\rangle \epsilon_c \langle i| + \sum_j |i\rangle \gamma \langle j| \right] \tag{3.1}$$

where $|i\rangle$ is a Hilbert-space vector representing an electron localised on a carbon atom labelled by the index i, and $|j\rangle$ is a nearest neighbour orbital to atom i. The quantities ϵ and γ are the on-site energy and hopping integral parameters for the carbon atoms of the pristine tube, respectively. The latter is assumed to be real and positive. Since this parameter will only ever appear in equations as $|\gamma|^2$, there is no loss in generality in doing this. The Hamiltonian $\hat{h}_a$ for the isolated atom is

concisely written as $\hat{h}_a = |a\rangle\alpha\langle a|$, where $|a\rangle$ represents the atomic orbital associated with the level α, and follows the same definitions as for the linear chain in Chapter Two. Here we choose to represent the electronic structure of the atomic impurity by a single level, once again for simplicity. This is easily extendable to more levels, where this demand is relaxed.

When decoupled, both nanotube and impurity atom can be accurately described by suitable values for the TB parameters for the Hamiltonians $\hat{h}_0$ and $\hat{h}_a$ that reproduce well the features of their electronic structure [2, 59]. However, changes in those parameters must occur when the two sub-systems are brought into contact. We assume that there is one carbon atom on the nanotube that lies closest to the dopant; furthermore, as a first approximation, we assume that the nanotube is highly efficient in screening any local charge variation and that only the on-site energy of that carbon atom nearest to the impurity is to be affected. I have previously introduced this as the efficient screening hypothesis. Efficient screening is not an essential feature of our method, and will be later relaxed to account for screening clouds of finite radius.

In light of the foregoing, it is reasonable to conclude that the parameters to be corrected should correspond to matrix elements which correspond to states localised in the vicinity of the contact between tube and impurity. Similarly, the on-site potential energy of the impurity atom is also allowed to change. Finally, the direct coupling between tube and the impurity atom is modelled by an added electronic hopping between them. In summary, the coupling between nanotube and impurity is represented by the following contact potential

$$\hat{V} = |0\rangle\delta_0\langle 0| + |a\rangle\delta_a\langle a| + |0\rangle\tau\langle a| + |a\rangle\tau^*\langle 0|, \tag{3.2}$$

where δ_0 and δ_a are the corrections to the on-site potentials on the nearest carbon site (labelled 0) and on the impurity atom (labelled a), respectively. This is a specific

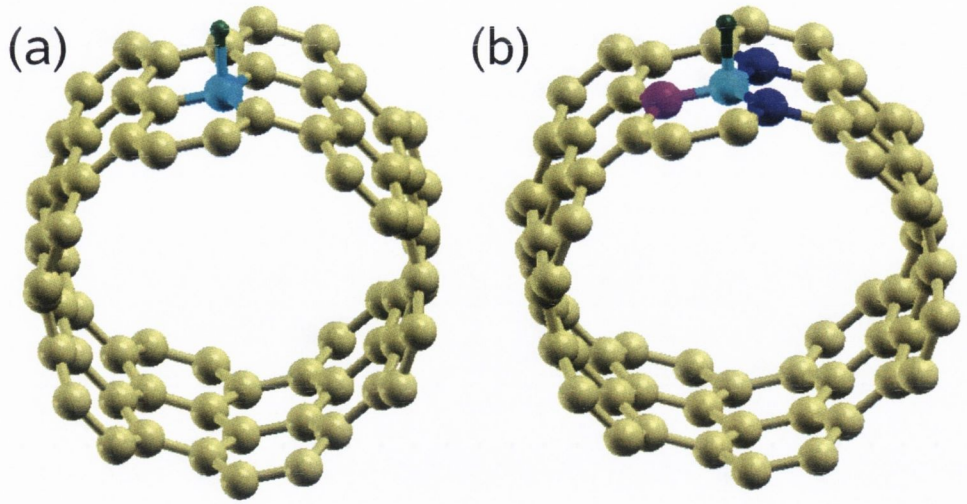

Figure 3.1: Schematic of the binding geometry between a (6,6) carbon nanotube and a hydrogen atom. The hydrogen atom is bonded directly to one single carbon atom, which we refer to as a type-I adsorbate in the text. (a) depicts the case where we assume perfect screening, while (b) relaxes this requirement to allow the onsite energy of the next nearest neighbours to the bonded carbon to change. In this fashion screening clouds of arbitrary size can be included.

case of the Hamiltonian presented in Eq. 2.7, where what were matrices are here simple scalars. I emphasise that this Hamiltonian is for the case when the dopant atom lies directly above one of the carbon atoms, which we will refer to as a type-I dopant. This is for instance the case for H adatoms bound to nanotubes. Other atoms, such as Lithium, preferably bind to a site located in the centre of one of the hexagons. Such an impurity will here be called type-II. The geometry involved in type-I binding is displayed in Fig. 3.1, while that in type-II is shown in Fig. 3.2. The hopping τ is responsible for coupling the nanotube to the impurity atom. It is, in principle, a complex number that has the dimensions of energy. Again, however, examination of the relevant equations later will show us that τ will only appear in our equations in the form $|\tau^2|$. Similarly to γ, we can thus take τ to be a real positive quantity, and I do so. There are no such concerns about δ_0 and δ_a, which correspond to diagonal elements of a Hermitian matrix: they are real energies, and may be either positive or negative.

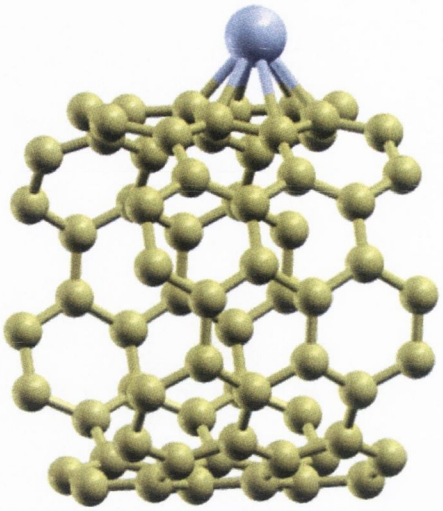

Figure 3.2: Schematic (before structural optimisation) of the binding between the (6,6) carbon nanotube and a type-II adsorbate. The case of perfect screening is illustrated; this can be relaxed through a process similar to that for a type-I defect

Bearing in mind the efficient screening hypothesis, it is clear that the set $(\delta_a, \delta_0, \tau)$ of corrective parameters is the minimal set necessary to take into account any changes in the Hamiltonian. Since it allows the determination of the total Hamiltonian $\hat{H}_0 + \hat{V}$ (and hence its eigenvalues and eigenstates), a knowledge of the perturbing potential fully determines the changes that the coupling brings to the electronic structure of the system, and consequently how it affects the transport properties of the structure. One of the aims of our work has been to introduce a simple procedure to determine this contact-induced perturbation, given knowledge of quantities that can be evaluated by *ab-initio* calculations, such as the binding energy and the charge transfer (for instance).

The binding energy is defined as the difference of total energies between the coupled and decoupled configurations and it reflects the degree of interaction between the two constituent parts. In mathematical terms, the binding energy ΔE is defined as the difference of total energies given by $\Delta E = E_{\mathrm{T}}(\mathrm{NT} + \mathrm{A}) - E_{\mathrm{T}}(\mathrm{NT}) - E_{\mathrm{T}}(\mathrm{A})$, where $E_{\mathrm{T}}(NT + \mathrm{A})$ represents the total energy for the coupled configuration, $\mathrm{E_T(NT)}$ is the total energy for the isolated nanotube and $\mathrm{E_T(A)}$ the total energy for the im-

purity atom. It is clear from the definition above that contributions to the total energy that are common to both configurations play no role in the binding energy because of cancellations. Such a role may be played by low energy core states which are far below the Fermi level, which partially justifies their absence in this treatment. Furthermore, in the so-called tight-binding total energy calculations, the total energy is given as the sum of two terms:

$$E_{\mathrm{T}} = E_{\mathrm{BS}} + E_{\mathrm{R}} \tag{3.3}$$

Here, the quantity E_{BS} is the band structure contribution to the total energy, and E_{R} is a repulsive term. E_{BS} is a negative energy that reflects the fact that electrons are bound to the ionic lattice, while E_{R} is a positive energy. In the framework of the so-called tight-binding total energy methods, one can write the total energy as the electronic structure contribution added to a repulsive energy term [60, 61, 62], in which the latter has been given a formal correspondence with modern density functional theory [63]. Moreover, as shown by Papaconstantopoulos and coworkers [60], this latter contribution can be accounted for by including it in the electronic on-site potential associated with the tight-binding Hamiltonian. In this way, the total energy can be written as a sum over the eigenvalues of the electronic Hamiltonian, which in turn allows us to express the binding energy as a function of $\Delta\rho$, the change in the density of states. In the case of hydrocarbons, it is possible to evaluate the repulsive energy term through the use of a parameterised sum [64]. Calculation shows that this contribution tends to be small enough to neglect. It is also worth emphasising that in all cases we are interested in energy changes, so that terms which are common to both configurations need not be taken into account explicitly.

Instead of using the Hamiltonian explicitly, we will describe all the relevant quantities in terms of the corresponding single-particle Green functions, which we have found to be extremely convenient in dealing with total energy variations. Part

of the reason for this is the existence of rather straightforward analytical (in the case of achiral nanotubes) and semi-analytical (in the case of chiral nanotubes) formulae for the single particle GF in real space. For instance, the Green function g_{ij} between arbitrary sites i and j of a pristine tube is obtained from that of graphene (itself derivable using simple renormalisation techniques based on Dyson's equation) by the imposition of appropriate boundary conditions. This approach is referred to as the so-called *zone-folding* approach. For the sake of completeness, I present the formulae for the Green function matrix elements in the case of armchair tubes; these will be used later in this chapter.

In the case of (n, n)–armchair nanotubes, there are two relevant matrix elements. If the carbon atoms are crystallographically equivalent (both in the same place in the unit cell of Fig. 1.1), then the matrix element at energy E is

$$\left\langle \vec{R}_1, A \middle| \hat{g}(E) \middle| \vec{R}_2, A \right\rangle = \frac{i(E + i\eta - \epsilon)}{4n\gamma^2} \sum_{k_x} \sum_{q_p} \frac{e^{i(k_x R_x + \frac{2q_p}{a} R_y)}}{\cos\left(\frac{ak_x\sqrt{3}}{2}\right) \sin q_p + 2 \sin q_p \cos q_p} \tag{3.4}$$

while if the atoms are inequivalent

$$\left\langle \vec{R}_1, A \middle| \hat{g}(E) \middle| \vec{R}_2, B \right\rangle = \frac{i}{4\gamma n} \sum_{k_x} \sum_{q_p} \frac{1 + 2e^{-iak_x \frac{\sqrt{3}}{2}} \cos(q_p) e^{i(k_x R_x + \frac{2q_p}{a} R_y)}}{\cos\left(\frac{ak_x\sqrt{3}}{2}\right) \sin q_p + 2 \sin q_p \cos q_p}. \tag{3.5}$$

The sum runs over the n distinct values $k_x \in \{0, \frac{2\pi}{\sqrt{3}an}, \frac{2.2\pi}{\sqrt{3}an}, \cdots, \frac{(n-1).2\pi}{\sqrt{3}an}\}$. The sum over q_p runs over those two values of q_i which have a positive imaginary part in the set $\{q_1, q_2, q_3, q_4\}$ where

$$\begin{aligned} q_1 &= \cos^{-1}\left(\frac{-b + \sqrt{b^2 - 4c}}{2}\right) \\ q_2 &= 2\pi - \cos^{-1}\left(\frac{-b + \sqrt{b^2 - 4c}}{2}\right) \\ q_3 &= \cos^{-1}\left(\frac{-b - \sqrt{b^2 - 4c}}{2}\right) \end{aligned}$$

$$q_4 = 2\pi - \cos^{-1}\left(\frac{-b - \sqrt{b^2 - 4c}}{2}\right) \tag{3.6}$$

with

$$\begin{aligned} b &= \cos\left(\frac{ak_x\sqrt{3}}{2}\right) \\ c &= \frac{1}{4} - \left(\frac{E + i\eta - \epsilon}{2\gamma}\right)^2 \end{aligned} \tag{3.7}$$

$\vec{R}_2 - \vec{R}_1 = (R_x, R_y)$ is the relative separation vector of the relevant sites in the unwrapped scheme. Similar formulae exist for the zigzag nanotubes [37]. The Green function for the matrix element $\left\langle \vec{R}_1, A \right| \hat{g}(E) \left| \vec{R}_1, A \right\rangle$ for a $(6,6)$ nanotube is presented in Fig. 3.3. We see that the real part is an odd function of energy (taking the energy zero to be at the carbon onsite). Consequently it must necessarily vanish at $E = \epsilon$. So the Green function is purely imaginary at $E = E_F (= \epsilon)$. This bears a striking similarity to the case of the pedagogical linear chain, whose Green function also has vanishing real part at the Fermi level. On the other hand, the imaginary part of the Green function is even, and purely negative. For the nanotube, there is one electron per carbon atom, so the Fermi level is coincident with the centre of the (spin-degenerate) band. Likewise, the Green function g_{aa} associated with the isolated adatom is a simple expression that results from the definition of the operator $\hat{g} = (E - \hat{H}_0)^{-1}$.

While it is true that such formulae provide a useful shortcut to the evaluation of the GF, it is worth bearing in mind that even in the general case, where no such formula exist, the GF will always be amenable to numerical evaluation. A numerical approach may be more suited to a multi-walled nanotube, for example, or if we require the use of more basis states to represent the nanotube itself.

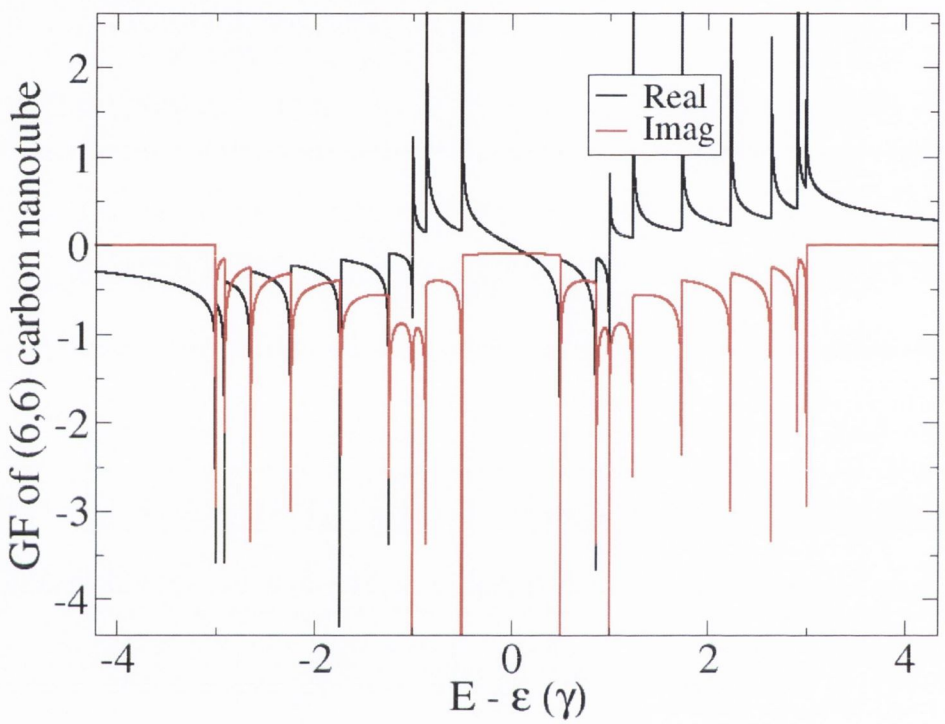

Figure 3.3: Real and imaginary parts of the $\left\langle \vec{R}_1, A \right| \hat{g} \left| \vec{R}_1, A \right\rangle$ Green function of a $(6,6)$ armchair nanotube as calculated using Eq. (3.4). The imaginary part is an even function of energy and is non-zero at the Fermi level ($E_F = \epsilon$), while the real part is an odd function of energy, and so vanishes there.

3.2.2 Evaluation of tight-binding parameters by the Lloyd formula method

The parameters associated with the potential $\hat{V}$ in Eq. (3.2) can be obtained by solving the Lloyd formula equations. This method is based on the existence of special sum rules for the total density of states in the presence of a localised perturbation. In our case, the localised nature of $\hat{V}$ leads to an expression for the variation of the total electronic density of states $\Delta\rho$ that reads

$$\Delta\rho(E) = -\frac{2}{\pi}\,\mathrm{Im}\;\mathrm{Tr}\;\frac{\mathrm{d}}{\mathrm{d}E}\log[\hat{1} - \hat{g}(E)\hat{V}]\;, \tag{3.8}$$

where Tr is the trace operator, which provides us with a complex number, Im takes the imaginary part of that complex number and $\hat{g}(E)$ contains the decoupled Green functions in block-diagonal form for electrons of energy E. While the above formula holds generally, with respect to the ordered basis $|0\rangle, |a\rangle$, in this case the matrix $\hat{g}(E)$ is given by

$$\hat{g}(E) \;=\; \begin{bmatrix} g_{00}(E) & 0 \\ 0 & g_{aa}(E) \end{bmatrix}\;, \tag{3.9}$$

where $g_{00}(E)$ and $g_{aa}(E)$ are the appropriate matrix elements of the unperturbed Green Function $\hat{g} = \lim_{\eta\to+}(E+i\eta-\hat{H}_0)^{-1}$ projected on sites $|0\rangle$ and $|a\rangle$, respectively. In matrix form, Eq. (3.2) is rewritten as

$$\hat{V} \;=\; \begin{bmatrix} \delta_0 & \tau \\ \tau^* & \delta_a \end{bmatrix}\;. \tag{3.10}$$

Making use of the energy derivative in Eq. (3.8), both the total energy variation ΔE and change in the total number of electrons in the system ΔN ("charge variation") are easily derived. The former is obtained by a simple integration by parts

which gives

$$\Delta E = \frac{2}{\pi} \int_{-\infty}^{E_F} \mathrm{d}E \ \mathrm{Im}\,\mathrm{Tr}\log[\hat{1} - \hat{g}(E)\hat{V}] \ , \tag{3.11}$$

whereas the latter is written as

$$\Delta N = \frac{-2}{\pi}\,\mathrm{Im}\,\mathrm{Tr}\log[\hat{1} - \hat{g}(E_F)\hat{V}] \ . \tag{3.12}$$

E_F in the equations above stands for the Fermi level of the system, which is the same as that of the nanotube, since $\alpha < \epsilon$ (in the case considered here). Eqs.(3.11) and (3.12) are two of the fundamental expressions in our method in the sense that they describe the change of two key quantities, namely total energy and total number of particles, as a result of the interaction between the tube and the impurity atom. At this point it is worth reiterating that in the operator form presented here, the above expressions are valid not only for $\hat{h}_0$ and $\hat{h}_a$ defined above but for whichever Hamiltonian is chosen to represent the electronic structure of the system, the only difference being in the precise form of the matrix elements of the operators $\hat{g}$ and $\hat{V}$. The size of the matrices will always be determined as $M \times M$, where M is the number of states, on either the nanotube or the dopant, which undergo a change in occupation number due to the binding (see Appendix C).

Substituting Eqs.(3.9) and (3.10) into Eqs.(3.11) and (3.12) we have

$$\Delta E = \frac{2}{\pi} \int_{-\infty}^{E_F} \mathrm{d}E \ \mathrm{Im}\left(\log\left(1 - g_{0,0}\,\delta_0\right)(1 - g_{a,a}\,\delta_a) - g_{0,0}\,g_{a,a}\,\tau^2\right)\right) \tag{3.13}$$

$$\Delta N = \frac{-2}{\pi}\mathrm{Im}\left(\log\left[(1 - g_{0,0}\,\delta_0)(1 - g_{a,a}\,\delta_a) - g_{0,0}\,g_{a,a}\,\tau^2\right]\right)_{E=E_F} \tag{3.14}$$

As presented thus far, there are not sufficient equations to determine a solution for the tight-binding parameters. However, a third equation may be derived by taking into account the charge transfer between tube and impurity. Dyson's equation allows us to obtain the change in the local density of states on the impurity site, which can be further integrated to express the charge transfer ΔC from the tube to the

impurity as follows:

$$\Delta C = -\frac{2}{\pi}\int_{-\infty}^{E_F} \mathrm{d}E\ \mathrm{Im}\left\{\left[g_{aa}^{-1} - \delta_a - (1 - g_{00}\,\delta_0)^{-1}\, g_{00}\,\tau^2\right]^{-1} - g_{aa}\right\}. \qquad (3.15)$$

The set of equations (3.13), (3.14) and (3.15) relates three basic quantities, namely the binding energy, the change in the total number of particles and the charge transfer, with the parameters δ_0, δ_a and τ associated with the potential $\hat{V}$. If we remember that Eq. (3.14) must reflect the charge neutrality of the system, we must impose that the total charge be conserved, *i.e*, $\Delta N = 0$. Therefore, the knowledge of ΔE and ΔC is in principle sufficient to determine the potential $\hat{V}$. Rather than relying on band structure fitting, which depends on which portions of the Brillouin zone are chosen to be reproduced, here we propose to use *ab-initio*-evaluated binding energies and charge transfers as input values to obtain the correct parameters of the potential $\hat{V}$. In this way, the parametrisation of the perturbing potential is done in a unique fashion since it does not depend on any choice of fitting points.

3.2.3 Results

It is worth noting the similarity of the expressions derived in the last section to those derived in the pedagogical case of a linear chain perturbed by a single atomic impurity. In reality, there is no structure yet discovered that corresponds to the simple linear chain. Even a simple poly-acetylene molecule (which would seem to be the ideal candidate to have its electronic structure described by the linear chain Hamiltonian) suffers a Peierls distortion, leading to a dimerisation of the molecule, which inevitably destroys its metalicity. The fact that nanotubes are known to bind with atoms and simple molecules allows us to test our method.

We have tested the method described above by applying it to the case of hydrogen atoms adsorbed to metallic nanotubes. The geometry of the problem (before structural optimisation) is illustrated in Fig. 3.1a. We start by considering a (6,6)

armchair nanotube in the presence of a single hydrogen atom. This choice of system meets the criterion that the potential be short-ranged (the metallic nanotube is efficient at screening the potential) and allows us to make use of the analytical formula for the Green function of the nanotube previously presented. *Ab-initio* calculations were used to evaluate the binding energy and charge transfer between the tube and the impurity atom. The calculations were performed using the SIESTA code [65, 66] within the LDA approach for the exchange–correlation potential [67]. Norm–conserving pseudopotentials and a split-valence double-ζ basis of pseudoatomic orbitals were used. The unit cell consisted of 73 atoms (72 for the (6,6) nanotube plus the hydrogen atom) was used. This corresponds to three fundamental unit cells for the carbon nanotube. While the code requires that we have a periodic system, the in–plane lattice parameter was chosen to be large enough ($\sim$ 60Å) to ensure a negligible interaction between periodic CN images. The structural geometry was optimised by conjugate gradient methods with a force tolerance of 0.05 eV/Å.

The geometrical optimisation showed that the sp^2 hybridisation (graphene-like) of the carbon atom linked to the hydrogen is converted to an sp^3-hybridisation (diamond-like), calling for a slight distortion of the carbon from its equilibrium position - it gets lifted off the surface of the nanotube. The C-H bond length was found to be 1.149Å, which is similar to that found in typical hydrocarbons such as the methane molecule ($\sim$ 1.10 Å). The calculated values for the total energy variation and the charge transfer to the adatom were $\Delta E = -2.74\,\mathrm{eV}$ and $\Delta C = -0.357\,\mathrm{e}$, respectively. Entering as input values in Eqs. (3.13) and (3.15), and using the appropriate tight-binding Green functions for the component parts, allowed us to obtain the corresponding values of $\delta_0 = -3.02\gamma$, $\delta_a = 3.35\gamma$ and $\tau = 1.95\gamma$ where γ was taken to have a value 2.66 eV. The solution of these highly non-linear equations required the use of an efficient numerical routine package, which was found to converge on a unique solution.

Although the Lloyd's formula method (LFM) does not rely on band structure

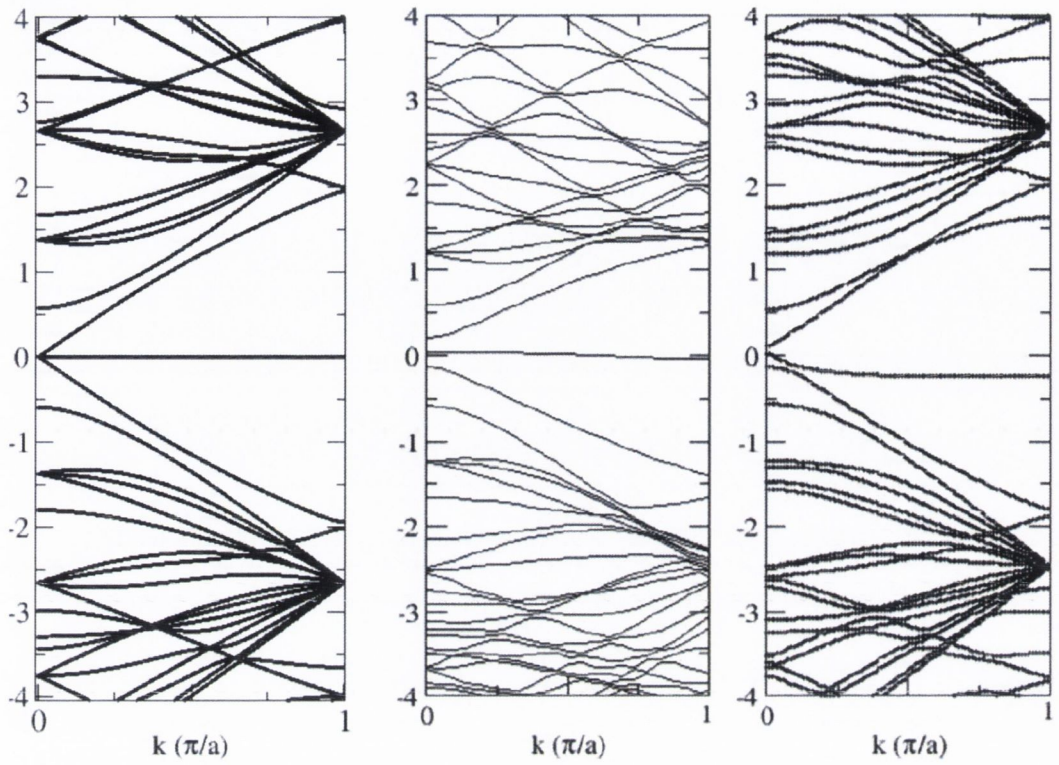

Figure 3.4: Folded band structures for a doped (6,6) nanotube with a single H atom per unit cell. The left and right panels are obtained by the Lloyd's formula method, the former within the efficient-screening assumption and the latter considering a screening cloud up to second nearest neighbours. The middle panel is the *ab-initio* result.

fitting, it is interesting to compare the *ab-initio* energy bands, as per the SIESTA calculation, with those obtained using the tight-binding parameters calculated using our scheme. With the set of parameters δ_0, δ_a and τ fully determined for a single impurity, we can reproduce the periodic boundary conditions used in the DFT calculations and obtain the corresponding energy dispersion. The band structure comparison is shown in Fig. 3.4 in which the DFT band structure (middle panel) is juxtaposed with the energy levels obtained by the Lloyd's formula method (left panel). Both diagrams display unmistakable similarities in the way their energy bands are distributed, which places the efficient screening hypothesis of the Lloyd's formula method as an excellent first approximation to describe the effect of impurity

atoms on the electronic structure of nanotubes. One source of difference between the two band structures could be our neglect of curvature effects, appropriate to such a small diameter nanotube, which would require a non-orthogonal basis set to be taken into account.

Despite the resemblance in the dispersion relations in the left and middle panels, the LFM parameterised bands are unable to reproduce some features of the band structure; the level at the Fermi energy is too flat, and the three-fold degeneracy at the Gamma point remains. Since it is crucial that we correctly treat those electrons at the Fermi level, this is worrying. It is worth recalling that the use of Eq. (3.2) with only three distinct undetermined parameters relies on the assumption of totally efficient screening by the conduction electrons of the nanotube. In other words, it assumes that any charge imbalance in the system due to the perturbing potential is screened, to the extent that only the on-site potential of the atom nearest to the perturbation is affected. Apparently, this is not a good assumption, as indicated by the local charge distribution that results from the DFT calculation. Despite the fact the system is indeed metallic, its low-dimensionality (1D) is one factor that acts to reduce its screening efficiency. In fact, the calculations point to a electronic charge distribution that is not entirely concentrated around a single atom but to one that is spread around a few nearest neighbours in the vicinity of the perturbation. The efficient-screening assumption must therefore be relaxed if we wish to improve the agreement between the band structures.

As already hinted at, imperfect screening can easily be included in our formalism if we consider that the perturbing potential $\hat{V}$ can now take into account changes in the onsite energies of the atoms beyond the nearest neighbours surrounding the contact region. Naturally, the simplest extension to our model is to include those atoms that correspond to *next–nearest* neighbours of the contact carbon atom. Although this increases the size of the matrix $\hat{V}$, Eq. (3.8) is still valid in expressing the change in the total density of states due to the contact between the impurity

and the tube. The potential $\hat{V}$ will now involve two more matrix elements, namely δ_0^1 and δ_0^2, which are corrections to the on-site potentials on the two non-equivalent nearest-neighbour carbon atoms. To comply with the extra undetermined matrix elements, an equal number of additional constraint equations are required. In this case, the two additional equations are expressions for the local charge variations on the nearest-neighbour atoms, which can also be read out from the DFT results. It turns out that the efficient-screening hypothesis is not a limitation of our approach in the sense that we can always consider screening clouds of arbitrary sizes, the only difference being in the number of equations required to obtain the adequate parameters. The set of five equations is straightforwardly derived from Eq. (3.8) but not displayed here for brevity. When solved, the equations provide the following results: $\delta_0 = 1.26\gamma$, $\delta_0^1 = -1.20\gamma$, $\delta_0^2 = -0.25\gamma$, $\delta_a = 0.28\gamma$ and $\tau = 0.76\gamma$, which lead to the band structure displayed in the rightmost panel of Fig. 3.4. Comparing with the results derived in the case of the efficient screening hypothesis, we see that there is an appreciable difference between the two sets of results. Intuitively, one would expect that as one expands the size of the screening cloud, that one would see a gradual convergence of the parameters, somewhat contrary to our findings. One reason for this may be that there exist a number of combinations of the parameters $(\delta_0, \delta_0^1, \delta_0^2, \tau, \delta_a)$ that satisfy all the Lloyd equations simultaneously. This is possible due to the inherent non-linearity of this system of equations. Consequently, we may be converging on a solution on a different branch; that is to say one which is not close to that of the efficient screening hypothesis.

Evidence for this may be garnered by focusing on the details of the behaviour of the bands in the vicinity of the Fermi level. We see that the threefold degeneracy at the Gamma point is indeed lifted. Furthermore, there appears to be a weakly dispersive level in the vicinity of the Fermi level. On the other hand the ordering of the bands seems to be incorrect; the weakly dispersive impurity band near the Fermi level [68] appears to be at too low an energy. The effect of this is to induce

an apparent avoided crossing [69] with the highest of the carbon valence bands. Since the position of this level is largely controlled by the value of δ_a, we see that the far lower value of this parameter found in the case of the imperfect screening may indicate that we are picking out an unphysical solution to our Lloyd formula equations. Nevertheless, bearing in mind that matching the DFT band structure is not a primary aim of this work, we will proceed with the results of the imperfect screening scenario in the remainder of this section.

As mentioned previously, the key advantage of mapping the first-principles results into a tight-binding calculation with a set of corrected parameters is that we do not have to restrict ourselves to a single impurity, and can in principle include a non-zero concentration of adsorbed atoms to model a truly disordered configuration. This allows us to investigate how the transport properties of carbon nanotubes are affected by a given concentration of impurity atoms along their length. Using our scheme for correcting the parameters of the electronic Hamiltonian, we have been able to include a large number of impurities randomly dispersed within a section of the nanotube. Each added impurity requires parameter corrections according to the size of the screening cloud, which here we have not let extend beyond the atoms connected to the binding site. The only constraint in the otherwise random distribution is that impurities are forced to always remain sufficiently far apart to avoid overlap between the screening clouds. If we wish to allow overlap of the screening clouds, new parameters must be calculated according to a procedure which is similar to the one already outlined. In this case, we perform the calculation in the presence of a pair of impurities, and extract tight-binding parameters which are appropriate in the case of a doubly perturbed system.

We have used the parameters $(\delta_0, \delta_0^1, \delta_0^2, \tau, \delta_a)$, derived in the imperfect screening case, to calculate the electrical response of the disordered system according to the Kubo formalism[70, 71]. As regards the geometry of the system, we may conceptualise it in the following fashion. From the left, we have a semi-infinite armchair

carbon nanotube, which terminates with a cleavage plane on the right. This tube extends infinitely far to the left. To the right, we have a similar semi-infinite tube, terminated at the left with a cleavage plane, and which extends infinitely far to the right. The central section corresponds a finite tube and is our scattering region; the perturbation is restricted to this region.

As far as the calculation is concerned, we proceed slightly differently. Here we have only two sections. As before, on the right hand side, we have a semi-infinite tube terminated by a cleavage plane on the left. The other section consists of the clean, semi-infinite tube, considered together with the scattering region.

To use the Kubo formula, we must calculate the appropriate surface Green functions of both the left and the right sections. To calculate the surface Green function of the left hand section, we utilise an adlayer approach. The surface Green function $G_{0,0}$ for a clean tube is a known quantity. We assume that the scattering region can be viewed as consisting of uncoupled rings of carbon atoms (with the ith ring characterised by known Green function $R_{i,i}$) which are coupled together through an appropriate Hamiltonian $T_{i,i+1}$. We proceed to calculate the Green function $G_{1,1}$ of the semi-infinite chain coupled together to the first ring, through the use of Dyson's equation, which yields:

$$G_{1,1} = (1 - R_{1,1}T_{1,0}G_{0,0}T_{0,1})^{-1}R_{1,1}. \tag{3.16}$$

In a similar fashion, it can be shown that

$$G_{i+1,i+1} = (1 - R_{i+1,i+1}T_{i+1,i}G_{i,i}T_{i,i+1})^{-1}R_{i+1,i+1}. \tag{3.17}$$

for $i > 0$.

In the scattering region, we have of the order of 1000 rings, leading to a scattering region of the order of 0.25μm. For each fixed configuration of scatterers, we can

calculate the zero-bias conductance through the use of the Kubo formula

$$\Gamma(E_F) = \frac{2e^2}{\hbar}\mathrm{Tr}\left(\hat{T}_{ab}\mathrm{Im}\left(\hat{G}_{ba}\right)\hat{T}_{ab}\mathrm{Im}\left(\hat{G}_{ba}\right) + \hat{T}_{ba}\mathrm{Im}\left(\hat{G}_{ab}\right)\hat{T}_{ba}\mathrm{Im}\left(\hat{G}_{ab}\right)\right.$$
$$\left. -\hat{T}_{ab}\mathrm{Im}\left(\hat{G}_{bb}\right)\hat{T}_{ba}\mathrm{Im}\left(\hat{G}_{aa}\right) - \hat{T}_{ba}\mathrm{Im}\left(\hat{G}_{aa}\right)\hat{T}_{ab}\mathrm{Im}\left(\hat{G}_{bb}\right)\right). \tag{3.18}$$

Here the index a corresponds to the rightmost ring of the scattering region, while the index b correpsonds to the beginning of the clean tube to the right of the scattering region. Upon averaging over a large number of disordered configurations (with the same concentration of scatterers) we can calculate the conductance as a function of the position of the Fermi level. In Fig. 3.5a such average conductances are displayed for four different concentrations of impurities. As is expected, the clean tube produces a well defined conductance (dotted line) which is always an integral multiple of the quantum of conductance, $2e^2/\hbar$. By symmetry, there is only one unique configuration in the case of a single scattering centre (dashed line). Higher concentrations of impurities are seen to correspondingly reduce the conductance (thick curves).

The concentration dependence of the conductance, as a function of the position of the Fermi level, is displayed in Fig. 3.5b. This shows the logarithm of the average conductance as a function of defect concentration, and indicates how a nanotube responds to H-doping. As expected, an exponential dependence on the impurity concentration is observed at sufficiently high concentrations.

Although the results presented in this section have been based on a highly simplified description for the electronic structure of both the nanotube and the atomic impurity (which nonetheless has been shown to agree well with the results of our *ab-initio* calculation), it is straightforward to generalise our procedure to account for more degrees of freedom. For instance, we may wish to take account of the multi-orbital character of the unperturbed Hamiltonian $\hat{H}_0$. The parameters τ, δ_0 and δ_a acquire a matrix character that reflects the additional degrees of freedom of

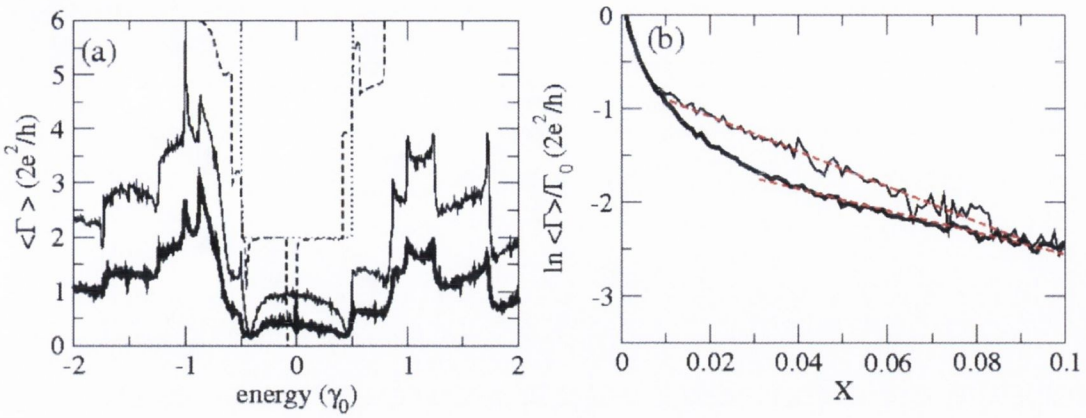

Figure 3.5: (a) Average conductance as a function of the Fermi energy for distinct concentrations of Hydrogen atoms distributed randomly along a (6, 6) carbon nanotube. The dotted line is the average conductance for a pristine tube; the dashed line corresponds to a carbon nanotube with only 1 adsorbed atom, thinner full line corresponds to 1% impurities while the broad full line is for x = 3% of impurities. (b) Logarithm of the average conductance (scaled by the conductance for the pristine tube) as a function of the concentration for distinct Fermi energies: thin (upper) line for $E_F = 0.0$ and broad (lower) line for $E_F = 1.2\gamma$. The dashed red lines correspond to linear fittings in the localised regime. Calculation performed by C. G. Rocha.

the constituent parts. The set of non-linear equations needed to obtain the corrected parameters are still based on the fundamental equations (3.11) and (3.12). Once again, an increase in the number of parameters requires the introduction of more equations, with one for each extra degree of freedom that is introduced. Following the same steps as before, we can use quantities from a simple DFT calculation as input to our set of non-linear equations. In addition to the binding energy and the overall charge transfer, we may require information about how the charge is distributed in their respective degrees of freedom, which again is readily available from DFT calculations.

3.3 An inverse modeling approach to the gas sensor problem

3.3.1 Motivation

Nanotube-based sensors depend on significant conductivity changes induced by doping. Predictions of which nanotube / foreign object (FO) combination provides efficient sensor characteristics tend to be made on an *ad hoc* basis, and involve a study of how a particular nanotube responds to the presence of a specific doping agent. With a multitude of possible combinations, this approach is unable to address questions of a general nature; for instance, what are the necessary features that the components must have, in order to produce certain physical properties in the device? Questions of this nature call for an inverse modeling scheme in which information about the components can be extracted from the knowledge of a few physical quantities demanded by the sensor. In this section we make use of the mathematical transparency of the Lloyd formalism, applying the method to adatoms and simple molecules adsorbed to nanotubes. We obtain a range of possible values for the ionisation potential that an impurity must have to meet specified requirements for the binding energy with, and for the charge transfer to, the nanotube host. Such an inverse modeling scheme allows a reduction in the multitude of possibilities that are generally considered by standard *ad hoc* approaches. We argue that this method can be further extended to provide general guidelines on the absorption process and can be used to narrow the search for the ideal combination of tube and doping agents required to produce efficient nanoscopic sensors.

To do this we explore another use for the Lloyd formula equations, namely, that they indicate the existence of a correlation between binding energy and charge transfer. For a given NT/FO pair, ΔE and ΔC are not independent quantities but are constrained by their respective expressions above. Of course, the actual relationship

between them depends on the specific values of the parameters δ_0, δ_a and τ, which themselves are constrained by the charge neutrality equation, as described in Chapter 2. In what follows, we assume that δ_a will be determined by the global charge neutrality condition $\Delta N = 0$, and view δ_0 and τ as essentially free parameters. If we were to choose those parameters arbitrarily, there is no guarantee that they would provide realistic figures for the binding energy and for the charge transfer. However, by varying the parameters up to maximum values $\bar{\delta_0}$ and $\bar{\tau}$, one finds the corresponding range of possible values for both ΔE and ΔC. In this fashion, a $\Delta E - \Delta C$ diagram can by created, as in the case of the linear chain and adsorbed impurity in Chapter 2. While this may be too broad a range, depending on the choice of $\bar{\delta_0}$ and $\bar{\tau}$, this approach highlights the relationship between those two quantities and, more importantly, points to an even broader range of incompatible combinations for ΔE and ΔC.

3.3.2 Calculations

For the case of adatoms on a (6,6) armchair NT, the relevant Green function elements for the $(6,6)$ nanotube are obtained by setting $n = 6$ in Eqs. (3.4) and (3.5). In the case of a type-I defect, such as an adsorbed Hydrogen atom, the only relevant nanotube Green function is $\langle 0, A| \hat{g} |0, A\rangle = g_{00}$. With type-I defects, the analytical techniques described in Chapter 2 can be used to calculate the allowed range of values δ_a, δ_0, τ. When we consider a type-II defect, however, the Lloyd matrix is much larger: it is a 7×7 symmetric matrix, involving Green function elements between the six sites on the hexagonal ring. In this case, we found it more reasonable to specify values for (δ_0, τ) and numerically solve for δ_a to satisfy the charge neutrality condition.

Calculated ΔE-ΔC diagrams are displayed in Fig. 3.6 for two different adatoms on a $(6,6)$ tube. The left panel displays the results for a H adatom, which is a type-I FO, while the right panel displays the results for a Li adatom, which is a type-II

FO. The shaded region of Fig. 3.6 is the set of values mapped into by the allowed triples $(\delta_a, \delta_0, \tau)$. The boundary of this contiguous region gives ranges containing the binding energies and charge transfers associated with those particular NT/FO pairs. The black dots, representing the corresponding DFT evaluations of both ΔE

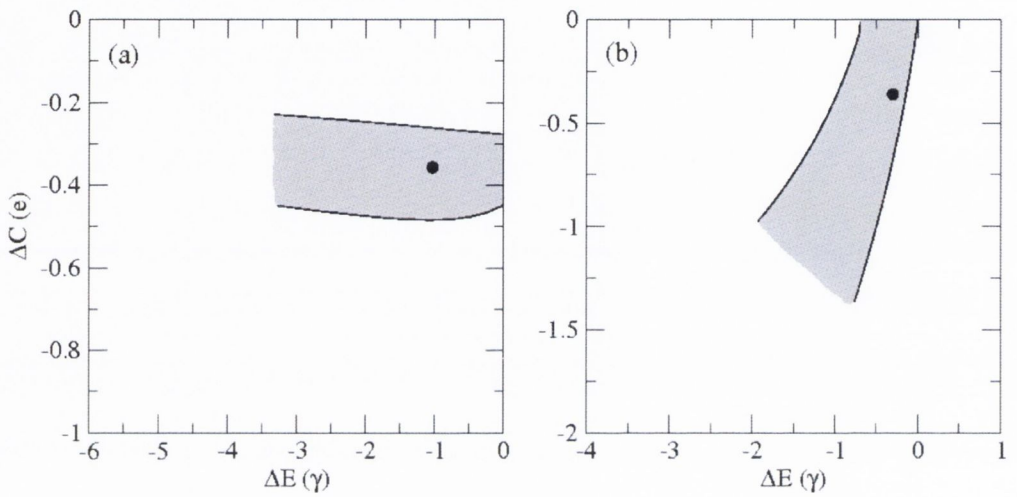

Figure 3.6: $\Delta E/\Delta C$ graphs displaying the regions of allowed values for the binding energy and charge transfer for (a) a Hydrogen adatom and (b) a Lithium adatom, both on a (6,6) NT. In plotting Fig.3.6, the thick lines were obtained by selecting $\bar{\delta_0} = 2.0\gamma$

and ΔC, lie within the predicted range.

The shaded regions of Fig. 3.6, are delimited by curves whose equations can be described by $\Delta C_u = U(\Delta E)$ and $\Delta C_l = L(\Delta E)$, where the functions $U(x)$ and $L(x)$ describe the upper and lower limit of the charge transfer for a energy change x, respectively. By knowing the functions U and L one can easily determine the whole range of possible values for ΔE and ΔC. Furthermore, assuming either of the two quantities is known, possibly by an isolated measurement, one can use the functions L and U to predict the range of allowed values that the other quantity may have. For instance, if only the charge transfer ΔC is known for a given NT/FO pair, the range of possible values for the corresponding binding energy is delimited by $L^{-1}(\Delta C)$ and by $U^{-1}(\Delta C)$, where F^{-1} is the inverse of function F. Likewise, if

only the binding energy ΔE is known, the corresponding charge transfer is certain to fall within the range delimited by $L(\Delta E)$ and $U(\Delta E)$. Since the curves are clearly smooth, both L and U can be approximated by polynomial functions of ΔE, described by $\Delta C_l = \sum_j l_j(\Delta E)^j$ and $\Delta C_u = (\Delta E)^j$ for the lower and upper limit, respectively. For the cases depicted in Fig. 3.6 the non-zero coefficients l_j and u_j are $l_0 = -0.28, l_1 = -0.01, l_2 = 5.00 \times 10^-4$, $l_3 = 2 \times 10^-4$, $u_0 = -0.45, u_1 = 0.10, u_2 = 0.14, u_3 = 0.12$ for the hydrogen bonding, while $l_0 = -0.02, l_1 = 2.43, l_2 = 0.88$, $l_3 = 0.80$, $u_0 = 7.78$, $u_1 = 10.58$, $u_2 = 5.30$, $u_3 = 1.27$ for the Lithium atom.

The results of Fig. 3.6 are of course only valid for the specific NT/FO pairs considered, i.e., H and Li adatoms on a (6,6) NT. A different pair will indeed lead to a different $\Delta E - \Delta C$-diagram. However, it is here that the mathematical transparency of Eq. (3.13), (3.14) and (3.15) becomes really useful. Because both equations are given not only in terms of the $\hat{V}$-parameters but also in terms of g_{00} and g_{aa}, which carry specific information about the NT and the FO, respectively, changes in either component of the pair will have a predictable effect on the relationship between ΔE and ΔC, and therefore on their corresponding diagram. Put in another way, the functions $L(\Delta E)$ and $U(\Delta E)$ can be described by polynomial functions whose coefficients depend on specific features of the NT/FO pair. By determining how the coefficients depend on those features, we can not only predict how the $\Delta E - \Delta C$ diagram changes but, more importantly, establish which features our pair must have to meet specific requirements regarding their binding energy and/or charge transfer.

To illustrate this point we assume the same NT as used in Fig.3.6 but this time we consider a type-I dopant with a variable energy level α. Bearing in mind our earlier definition, this corresponds to considering foreign objects with different ionisation potentials. The α-dependence of the coefficients l_j and u_j indicates, through the functions L and U, how the ΔE-ΔC-diagram changes as different FO are considered. More specifically, by determining the coefficients $l_j(\alpha)$ and $u_j(\alpha)$, we are able to work out the respective functions $L(\Delta E)$ and $U(\Delta E)$, thus predicting the allowed range

of values for their binding energy and charge transfer.

It is natural to compare the predicted ranges with the actual values of binding energies and charge transfers obtained by separately evaluated ab-initio results. In addition to the H and Li adatoms already presented in Fig. 3.6, a number of additional FO were considered, among which a variety of other adatoms as well as a few simple molecules.

FO	Type	α	ΔE	ΔC	$L^{-1}(\Delta C)$	$U^{-1}(\Delta C)$	$L(\Delta E)$	$U(\Delta E)$	$\frac{\Delta\rho(E_F)}{\rho(E_F)}$
H	I	-5.04	-1.03	-0.357	–	–	-0.491	-.266	0.44
Xe	I	-4.49	0.07	-0.010	0.949	-0.163	-0.076	0.003	0.017
Ar	II	-5.84	0.03	-0.011	1.945	-0.493	-0.070	0.000	0.012
Li	II	-1.99	-0.30	-0.360	-0.134	-0.973	-0.693	1.095	1.86
Na	II	-1.90	-0.08	-0.170	-0.043	-0.972	-0.334	6.102	2.33
N_2	II	-5.77	-1.2	-0.011	1.901	-0.407	-0.038	0.031	0.097

Table 3.1: Table of the ionisation potentials (α), binding energies (ΔE), charge transfer (ΔC), and $\Delta E - \Delta C$ diagram parameters for various foreign objects in the vicinity of a carbon nanotube. Energies are given in multiples of γ and charges in multiples of the magnitude of the electron charge. The final column lists the fractional change in the DOS for each configuration.

Table 3.1 shows those results for ΔE and ΔC associated with all the listed NT/FO pairs. It is remarkable that despite the simple description of the electronic structure of the separate parts, all results lie well within the predicted ranges.

At this point we are ready to answer some of the general questions posed earlier regarding the type of FO necessary to meet certain requirements. We can ask what features a FO must have to produce a specific set of binding energy ΔE^0 and charge transfer ΔC^0. The answer to such an inverse problem is now straightforward and follows from the solution of $\Delta C^0 \leq U(\Delta E^0)$ and $\Delta C^0 \geq L(\Delta E^0)$, which gives a range of possible values for α.

For instance, if one is looking for a FO on a (6,6) NT for which the binding energy is around $\Delta E^0 = -0.16\gamma$ and has $\Delta C^0 = -0.10$e, our method suggests that good candidates are type-II foreign objects whose ionisation potentials are in the range $-1.24\gamma > U_I > -2.36$. This range reduces the universe of possibilities one

would have to try by the forward modeling approach. The values of ΔE^0 and ΔC^0 listed above correspond to those found in the case of a potassium adatom adsorbed to a (6,6) NT. Being a type-II FO, the ionisation potential of $U_I = -1.63\gamma$ naturally meets the above requirements.

Moreover, although we have varied the parameter that characterises the FO, we could also change the parameters defining the NT. In this case, both the diameter d and the chiral angle θ of the NT host can be varied through the GF g_{00}. A similar analysis would follow, this time providing a set of values for θ (and subsequently d) that meets the specific requirements of binding energy and charge transfer.

Finally, it is worth mentioning that having written $\Delta\rho(E_F)$, ΔE and ΔC under a common framework, these quantities are no longer evaluated in a disconnected fashion. Eqs. (3.8), (3.13), (3.15) and (3.14) are able to relate the DOS change with the respective values of binding energy and charge transfer. Listed as a percentage of the unperturbed original DOS, Table 3.1 makes use of Eq. (3.8) to express how $\Delta\rho(E_F)$ is affected by the presence of each FO, indicating Na as the one causing the largest variation. Bearing in mind that changes in the physical properties are intrinsically associated with changes in the DOS, this procedure indicates how effective a FO is in altering the NT transport properties, which in turn determines how good a sensor the NT/FO pair may turn out to be.

3.4 Chapter summary

This chapter dealt with two facets of the binding between carbon nanotubes and localised molecular impurities. In the first part, we have presented a method that provides a simple way of accounting for disorder effects on the transport properties of doped nanotubes. *Ab-initio* evaluations of the electronic structure of a nanotube with a single doping atom have been used as inputs to generate the corresponding changes to the tight-binding-like parameters in the vicinity of the impurity. Our

method makes use of special sum rules for the single-particle Green functions that provide a closed-form expression for the variation of the total density of states, which in turn can be used to relate the desired parameters with quantities like binding energy and charge transfer. These latter quantities, when evaluated by first principles, give a direct way of determining the unknown parameters. It is worth stressing that unlike band structure fitting, we do not depend on the choice of Brillouin zone points to be matched against. On the contrary, a finite number of equations give unique solutions to the parameters that can be used to evaluate the corresponding conductances. By averaging over a large ensemble of disordered configurations, we can obtain results with statistical significance that are likely to reproduce measurable results.

In the second part, we have expressed the DOS variation $\Delta\rho$, the electronic binding energy ΔE and the charge transfer ΔC that result from the interaction between a metallic carbon nanotube and an unspecified molecular foreign object under a common framework. Written in terms of a set of *undetermined* perturbation parameters, these expressions establish a constraint between those quantities, in particular the latter two. By varying the potential parameters up to selected maximum values we are able to find a limited range of permitted values for both ΔE and ΔC. Separately evaluated ab-initio results for a number of foreign object lie within the predicted ranges. Furthermore, the mathematical transparency of our expressions allows us to distinguish the contributions coming from both parts involved in the interaction, enabling us to trace how the predicted range of values changes with variations of the nanotube/foreign object pair. This can be used to solve the inverse problem of finding foreign object meeting specific requirements on their binding energy and charge transfer. In the cases of simple atomic adsorbates, this leads to a range of values for the ionisation potentials that indicates possible candidates for desirable doping agents. More importantly, this method can be useful to provide general guidelines in the search for ideal nanotube-based sensors.

The work presented in this chapter has been published, and can be found in references [72], [73] and [74].

Chapter 4

Modeling helically ordered perturbations of nanotubes

4.1 Introduction

4.1.1 Motivation

Nanotubes are one example of low-dimensional nanoscopic structures that have been at the forefront of intensive scientific investigation for more than a decade. As well as their remarkable *intrinsic* physical properties and enormous potential for technological applications, *doped nanotubes* have also been in focus due to the possibility of engineering desirable characteristics in nanotube-based devices.

Typically, impurities are randomly dispersed in relation to the nanotube; as such they are spatially uncorrelated and are responsible for multiply scattering the electrons that travel across the structure. As a result of this scattering, the amplitude of the transmitted wave functions are reduced and so, as a consequence, is the overall conductance of the material. This is the case, for instance, in conductance modulation of nanotubes through both atomic and molecular doping as has been reported by a number of authors [57, 56, 58]. To give a concrete example of one way of utilising this effect, the ability to change the conductance of a nanotube exposed

to certain gaseous molecules is driving the research to build sensitive nanodevices capable of detecting minute concentrations of specific substances [75].

Of a very different nature, geometrically ordered doping agents can also affect the conductivity of a host material but examples are not as plentiful and common as their disordered counterparts. Having nanotubes as hosts, the list of examples in which impurities are spatially ordered is even more limited. Although the underlying lattice remains the same, in this case the spatially ordered perturbing potential that acts on the nanotube due to the impurities may follow a different geometrical arrangement. Depending on the strength of the perturbation as well as on its spatial geometry, this can in principle lead to interference effects, both constructive and destructive, that must affect the overall band structure of the material. Rather than a purely abstract and speculative hypothesis, here we argue that this may actually occur with nanotubes helically wrapped by linear charge distributions.

Among a plethora of possible doping agents, charged 1-dimensional-like structures such as polymers and DNA molecules are known to interact with nanotubes and to produce unusual physical properties: the former affecting the mechanical [24], thermal [18, 17] and electronic [76] properties of nanotube-polymer composite materials and the latter being used as a technique to separate nanotubes of different nature [77]. As a result of this interaction, these molecules can sometimes coat the walls of a nanotube. One common feature observed in the coating morphology is the fact that the molecules tend to wrap around the tubular structures in a helical fashion [78, 79, 80, 81], as displayed in Fig. 4.1. Despite previous suggestions that this helicity should follow the chirality of the nanotube [82], there have been suggestions that these bulky molecules are not capable of resolving the atomic structure of the underlying lattice [28]. Therefore, a physical mechanism that favours chiral order without depending on the underlying atomic structure is a possible candidate to explain the helical wrapping of molecules. It is our goal to show that the electronic contribution to the total energy is one such possible mechanism.

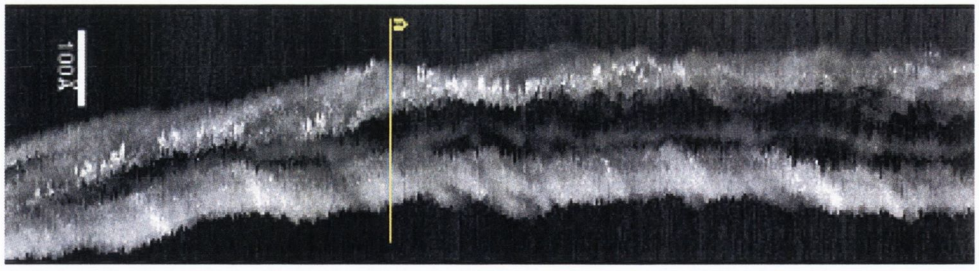

Figure 4.1: A STM image of PmPV-coated single wall nanotubes [78]. There is a notable ordering in the PmPV coating in the lower tube, with an obvious helicity to the coating. The wrapping angle is well defined, and is about 19° to the nanotube axis. These SWNTs are found to be coated with only 1 or 2 layers of PmPV.

While the DNA and some of the polymer molecules may have many differences, they share the common characteristic of being classifiable as quasi-linear charge distributions. Motivated by this commonality, I have investigated the energetics of helically ordered 1-dimensional-like charge distributions around nanotubes. It is worth emphasising that this geometry must result from the favourable balance between the entropic, elastic and electronic contributions to the free energy of the system [83, 28]. However, under the assumption that the latter two are the dominant contributions to the energy balance [28], especially at low temperatures, we are particularly interested in the electronic part of the total energy. Our investigations have shown that this contribution can lead to the existence of energetically-favourable wrapping directions that result from quantum interference patterns between different sections of a wrapping strand.

Rather than providing an exact quantitative description for the full energetic balance, in this research we focus on simple models for the electronic structure of both the cylinder and the linear charge distribution with the purpose of highlighting qualitative features that must also appear in more quantitatively accurate methods. Furthermore, since the total energy evaluated here is based on the electronic structure of the system under investigation, this study may be of help to understanding some of the electronic properties of DNA- and polymer-wrapped nanotubes.

4.1.2 Layout of this chapter

This chapter can be considered as consisting of two distinct, but closely related parts. In the first part, we start off by considering a one-dimensional free electron gas and show that a periodic perturbation of localised scatterers induces an energy change that depends non-monotonically on the common spacing of the scatterers. We do this by calculating a formula for the relevant Green function element in a mixed basis, and utilising the Lloyd's formula method, as has been introduced in previous chapters. We also consider the similar case of a two dimensional free electron gas perturbed by a series of line delta functions. We show how this problem can be viewed as being equivalent to a series of one-dimensional problems. Again, we utilise the Lloyd's formula method as an efficient way of calculating the energy change due to the perturbation. We then show how the problem that we ultimately wish to solve, that of a free electron gas cylinder wrapped by a polarising potential, can be considered as a limiting case of the two dimensional free electron gas perturbed by a series of line delta functions, albeit with the inclusion of appropriate boundary conditions. The energy change due to different coiling angles is calculated, and the existence of favourable inter-scatterer distances, and thus favourable coiling angles is shown.

In the second part, we treat the nanotube within the tight-binding model and treat the influence of the charged coiling perturbation on the nanotube by considering various coiling square well potentials on the nanotubes surface. I again show that there is a non-monotonic dependence on binding energy for different coiling angles, when this more realistic model for the electronic structure of the nanotube is utilised. Investigations have been performed into the effects that such a perturbation has on the electronic structure of the tube, as characterised by parameters such as the size of perturbation-induced mini-gaps and the energy of the first optical transition, in terms of parameters which characterise the perturbation, such as amplitude, width of the well, and coiling angle. The work in this chapter is based in

part on work done with Mauro S. Ferreira, and has been published in [84] and [85].

4.2 Modeling nanotube polymer interaction via free electron gas

4.2.1 Overview

My overall aim in this portion of the work was to model the nanotube as a 2-dimensional free electron gas closed into an infinitely long cylinder of nanoscale radius R, and investigate what effect a helical charge distribution would have on the electronic structure of the cylinder. Due to the extremely high aspect ratio of most nanotubes, it is quite a good approximation to take the length as tending to infinity. Because the presence of a charge distribution near the tube (such as that carried on the backbone of a wrapping DNA molecule) will polarise the electron density in its proximity, we include a helically symmetric potential to reproduce this effect. Considering metallic nanotubes, we assume that the electron gas is highly efficient at screening electric fields due to extra charge appearing in the system, which suggests that a short-ranged potential is appropriate. Taking the most extreme limit of this, we have assumed a delta-function potential. While this may not be the most convincing model for the effect of a wrapping molecule, it does allow us to evaluate the key quantities analytically, bringing a degree of transparency to our results. I wish to emphasise that perfect screening is not an essential ingredient in our model, and can be relaxed by assuming a longer-range potential, such as a square well potential. In fact, as will be seen later in this chapter, when we move to a tight-binding model, we find that this brings no qualitative difference to neither our results nor conclusions.

With these simplifications, we have mapped the problem of a helical charge distribution surrounding the surface of a nanotube into that of a cylindrical electron

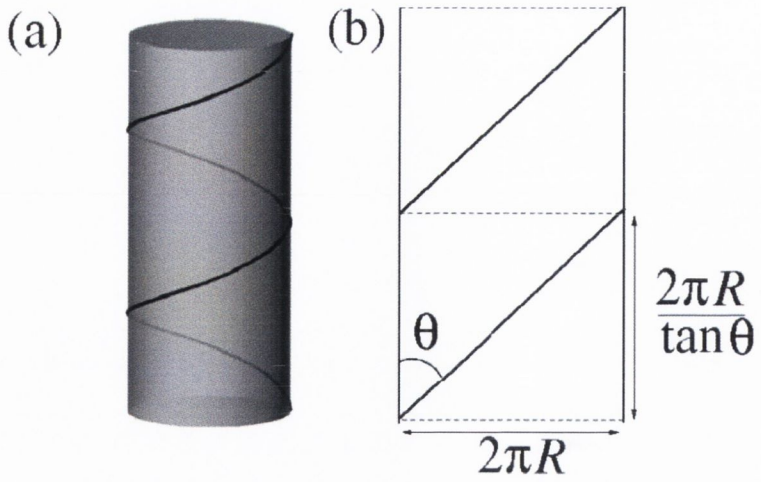

Figure 4.2: Schematic diagram of the geometry involved in helical wrapping. (a) A single strand is assumed to wind around an infinitely long cylinder of radius R at a constant angle θ. (b) In the two dimensional depiction, the unwrapped tube is represented by a stripe of free electron gas of width $2\pi R$. The coiling angle θ defines a unit cell of length $2\pi R/\tan\theta$. Equivalence of the two representations is established by demanding that the value of the wavefunction at the left hand boundary of the rectangle matches that on the point on the right hand side, at the same height.

gas subject to a helically-symmetric delta-function potential. Fig. 4.2a shows the geometry of the potential in three dimensions, while Fig. 4.2b displays the corresponding unwrapped version in the plane. The process by which the electronic structure of the tube can be extracted from that of the unwrapped periodic case is described later in the chapter, and is in the same spirit as the zone-folding approach to extracting the band structure of nanotubes from that of a graphene sheet. By calculating the energetics of this system our aim was to root out preferential wrapping angles which minimise the total electronic energy of the system, and thus show that even if we neglect the detailed geometry of the nanotube, it is possible for a coiling perturbation to coil preferentially at certain angles.

To calculate the electronic energy levels of a given material, the choice of a suitable coordinate system that reflects the underlying symmetry of the problem under investigation is usually called for. Here, given the coiling geometry of the problem, one would expect the use of a helical coordinate system to solve the single particle Schroedinger equation. However, treating the system in its unwrapped form, as

shown in Fig. 4.2b, avoids this. Usefully, in this form we can see that the helical potential is equivalent to an array of equally-spaced line delta functions embedded in a 2-dimensional electron gas, under the imposition of appropriate boundary conditions on the electronic wave function. There is a striking similarity between this representation and the familiar Dirac-comb potential (one limiting case of the more general Kronig-Penney model) where electrons experience a periodic potential formed by equidistant delta functions. In that case the total energy depends non-monotonically on the scatterer separation, suggesting the existence of preferential spacings. The basic idea of this research is to investigate this similarity and show that the total electronic energy of the helical charge distribution displays similar non-monotonicities as a function of the separation D (see Fig. 4.2b), and consequently as a function of the wrapping angle θ.

4.2.2 Perturbed Free Electron Gas in 1D

Finite Number of Scatterers

We start with the well known text-book problem [86] of a 1-dimensional electron gas, perturbed by a single delta function, weighted by a parameter $V(x) = \lambda\,\delta(x - x_0)$. The unperturbed system is a free electron gas in one dimension, and we investigate only one spin channel. We assume that the gas is confined to a circle of length $Na, N \to \infty$ (periodic boundary conditions). If we denote the eigenstates of position by $|x\rangle$, it is well known that the eigenstates of the Hamiltonian are the completely delocalised states $|k\rangle$, where

$$|k\rangle = \frac{1}{\sqrt{Na}} \int_{-Na/2}^{Na/2} e^{ikx} |x\rangle, \tag{4.1}$$

The state k has crystal momentum $\hbar k$ and energy eigenvalue $\frac{\hbar^2 k^2}{2m}$.

In principle, to calculate the total energy for this system requires the calculation of the spectrum of the Hamiltonian and summing over the occupied energy levels.

However, we are interested only in *changes* in the total energy, a quantity that gives an idea of how energetically favourable this interaction is. In terms of Green functions (GF), this calculation becomes extremely simple due to the localised nature of the perturbing potential. Up to now, I have only used Lloyd's formula (as in chapters 2 and 3) with reference to a discrete system, such as that of the linear chain of atomic orbitals. However, the form of Lloyd's formula holds also for the continuum case, which after all can be viewed as the same as a cellularised space in the limit of vanishing cell size.

Indeed, it is straightforward to show that the effect of the delta function on the total density of states of the non-interacting single-spin electron gas is fully accounted for by Lloyd's formula [39],

$$\Delta\rho(E) = -\frac{1}{\pi}\frac{\mathrm{d}}{\mathrm{d}E}\mathrm{Im}\left\{\log\left(1 - \lambda\left\langle x_0\right|\hat{g}\left|x_0\right\rangle\right)\right\}. \tag{4.2}$$

$\Delta\rho(E)$ is the variation in the total density of states ρ for electrons with energy E, $\hat{g}(E) = ((E + i0^+)\hat{1} - \hat{H})^{-1}$ is the GF operator associated with the free-electron Hamiltonian $\hat{H}$, and the quantum basis $|x\rangle$ labels the eigenvectors of the position operator.

A simple integration by parts provides the total energy variation $\delta\epsilon_1$ due to the presence of a single delta function impurity. It is given by

$$\delta\epsilon_1 = \frac{1}{\pi}\int_{-\infty}^{E_F}\mathrm{d}E\ \mathrm{Im}\log\left(1 - \lambda\ \left\langle x_0\right|\hat{g}\left|x_0\right\rangle\right). \tag{4.3}$$

The Green function matrix element appearing in Eqs. (4.2) and (4.3) is derived in Appendix F, and is given by:

$$\left\langle x_0\right|\hat{g}\left|x_0\right\rangle = -i\sqrt{\frac{1}{2(E + i0^+)}}, \tag{4.4}$$

where $\hbar = 1, m_\mathrm{e} = 1$ and $i0^+$ is a small positive imaginary energy that ensures we

select the retarded Green function. The quantity E_F is the Fermi level and regulates the electronic occupation of the system; at zero temperature, all states with energy lower than E_F are fully occupied, while those above are empty. As energy reference we choose the total energy of the perturbation-free electron gas, which means that the total electronic energy of the system with a single perturbation is given by $\delta\epsilon_1$. The quantity λ is the weight of the associated delta function.

We can then study how the total energy of a system of N identical localised perturbing potentials depends on their common separation, D. In this case, due to quantum interference effects, the total energy of the system $\delta\epsilon_N(D)$ will differ from $N\delta\epsilon_1$ in general. To be precise, we should have $\lim_{D\to\infty}\delta\epsilon_N(D) = N\delta\epsilon_1$. It is simple to generalise Eq. (4.3) to express the energy variation due to the introduction of N perturbations. With the perturbing potential now described by $V(x) = \lambda\sum_{j=1}^{N}\delta(x - jD)$, the total energy change reads

$$\delta\epsilon_N(D) = \frac{1}{\pi}\int_{-\infty}^{E_F} \mathrm{d}E\ \mathrm{Im}\left(\log\left(\det\left(\hat{1} - \lambda\hat{M}\right)\right)\right) \tag{4.5}$$

In the equation above, $\hat{1}$ is the identity matrix and $\hat{M}$ is a $N \times N$ matrix whose elements are $[M]_{\ell,m} = \langle \ell D|\, \hat{g}\, |mD\rangle$, the kets and bras being eigenstates of the position operator. Having given the relevant expressions in the case of a finite number of scatterers, I now develop similar results in the case of an infinite array of scatterers.

Infinite Number of scatterers

Having given the relevant expressions in the case of a finite number of scatterers, I now develop similar results in the case of an infinite array of scatterers. The system now undergoes a periodic perturbation, so we can utilise Bloch's theorem. The perturbation Hamiltonian is given as

$$\hat{V} = \lambda \lim_{N\to\infty}\sum_{j=0}^{N} |ja\rangle\langle ja|, \tag{4.6}$$

where λ is a continuous parameter that determines the strength of the perturbation. This corresponds to a weighted Dirac comb potential in real space.

If we cellularise the system according to the rule

$$x' = ja + x \tag{4.7}$$

where j labels cells and x is an intra-cell index, then we can write the perturbation Hamiltonian as

$$\hat{V} = \lambda \lim_{N\to\infty} \sum_{j=0}^{N} |j,0\rangle\langle j,0|, \tag{4.8}$$

where

$$|j,x\rangle := |ja + x\rangle. \tag{4.9}$$

Here j is an intercell index, while x is an intracell index. We introduce the *mixed basis* $|k,x\rangle$, where

$$|k,x\rangle = |k\rangle|x\rangle \tag{4.10}$$

and

$$|k\rangle = \lim_{N\to\infty} \frac{1}{N} \sum_{j=0}^{N} e^{ijka} |j\rangle. \tag{4.11}$$

Here k is a wavenumber; since we have (discrete) translational symmetry, we can apply the Bloch theorem. The quantity x labels the points inside a single unit cell.

With this definition a little algebra leads to

$$\hat{V} = \lambda \lim_{N\to\infty} \sum_{k=0}^{\frac{2\pi}{a}} |k,0\rangle\langle k,0|, \tag{4.12}$$

where

$$\Delta k = \frac{2\pi}{Na}. \tag{4.13}$$

In the special case that we can write both the Green function of the unperturbed

system and the perturbation Hamiltonian in the form

$$\hat{O} = \sum_k \hat{O}_k, \tag{4.14}$$

where

$$\hat{O}_k := \langle k| \hat{O} |k'\rangle \, \delta^k_{k'} \tag{4.15}$$

is a partial projection of the relevant operator, we can write the Lloyd formula as

$$\Delta\rho(E) = \sum_k \frac{-1}{\pi} \mathrm{Im} \left(\frac{\mathrm{d}}{\mathrm{d}E} \left(\log \left(\det \left(\hat{1}_k - \hat{g}_k(E) \hat{V}_k \right) \right) \right) \right). \tag{4.16}$$

In the present case, it is possible to show that both $\hat{g}$ and $\hat{V}$ can be written in the form of Eq. (4.15), where

$$\hat{V}_k = \lambda |k, x_0\rangle \langle k, x_0| \tag{4.17}$$

and

$$\hat{g}_k = \int_0^a \mathrm{d}x |k, x\rangle \, \langle k, x| \, \hat{g} \, |k, x\rangle \, \langle k, x|. \tag{4.18}$$

Furthermore, as has been discussed in chapter 2 in the case of a single impurity, the determinant collapses to the simple scalar function $1 - \lambda \, \langle k, x_0| \, \hat{g} \, |k, x_0\rangle$. So the change in the density of states is given as

$$\Delta\rho(E) = \sum_k \frac{-1}{\pi} \mathrm{Im} \left(\frac{\mathrm{d}}{\mathrm{d}E} \left(\log \left(1 - \lambda \, \langle k, x_0| \, \hat{g} \, |k, x_0\rangle \right) \right) \right). \tag{4.19}$$

To evaluate the quantity $\langle k, x_0| \, \hat{g} \, |k, x_0\rangle$, we start with the observation that the real space matrix element of the Green function of a free electron gas in one dimension is given by the formula

$$\langle x| \, \hat{g} \, |x'\rangle = \langle x_0| \, \hat{g} \, |x_0\rangle \, e^{ik_p(E)|x - x'|}, \tag{4.20}$$

where $g_{00} := \langle x_0| \, \hat{g} \, |x_0\rangle$ has already been introduced in Eq. (4.4), and $k_p(E) =$

$\pm\sqrt{2E+i0^+}, \mathrm{Im}\,(k_p) > 0$. By Eq. (4.11) and presumed orthonormality of the real space kets,

$$\langle j, x|k, x_0\rangle = \frac{e^{ijka}}{\sqrt{N}}\delta(x - x_0). \tag{4.21}$$

With this result we can calculate $\langle k, x_0|\,\hat{g}\,|k, x_0\rangle$:

$$\begin{aligned}
\hat{g} &= \int_0^{Na} \mathrm{d}x \int_0^{Na} \mathrm{d}x' |x\rangle\langle x'| g_{x,x'} \\
&= \sum_{j,j'} \int_0^a \mathrm{d}x \int_0^a \mathrm{d}x' |j, x\rangle\langle j', x'|\,\langle j, x|\,\hat{g}\,|j', x'\rangle \\
&= \sum_{j,j'} \int_0^a \mathrm{d}x \int_0^a \mathrm{d}x' |j, x\rangle\langle j', x'| g_{00} e^{ik_p|(j-j')a+x-x'|}
\end{aligned} \tag{4.22}$$

This can be projected down to yield:

$$\begin{aligned}
\langle k, x_0|\,\hat{g}\,|k, x_0\rangle &= \sum_{j,j'} \int_0^a \mathrm{d}x \int_0^a \mathrm{d}x' \langle k, x_0|j, x\rangle\langle j', x'|k, x_0\rangle g_{00} e^{ik_p|(j-j')a+x-x'|} \\
&= \sum_{j,j'} \frac{e^{iak(j'-j)}}{N} g_{00} e^{ik_p a|(j-j')|} \\
&= \frac{g_{00}}{N} \sum_{j,j'} e^{iak(j'-j)} e^{ik_p a|(j-j')|}
\end{aligned} \tag{4.23}$$

which by shifting the index (in the limit that $N \to \infty$) is the same as

$$\begin{aligned}
\langle k, x_0|\,\hat{g}\,|k, x_0\rangle &= g_{00} \sum_{j=-\infty}^{\infty} e^{iakj} e^{ik_p a|j|} \\
&= g_{00} \left(\sum_{j=-\infty}^{-1} e^{iakj} e^{ik_p a|j|} + \sum_{j=1}^{\infty} e^{iakj} e^{ik_p a|j|} + 1 \right) \\
&= g_{00} \left(\sum_{j=1}^{\infty} e^{-iakj} e^{ik_p aj} + \sum_{j=1}^{\infty} e^{iakj} e^{ik_p a|j|} + 1 \right) \\
&= g_{00} \left(\frac{e^{ia(k_p-k)}}{1 - e^{ia(k_p-k)}} + \frac{e^{ia(k_p+k)}}{1 - e^{ia(k_p+k)}} + 1 \right)
\end{aligned}$$

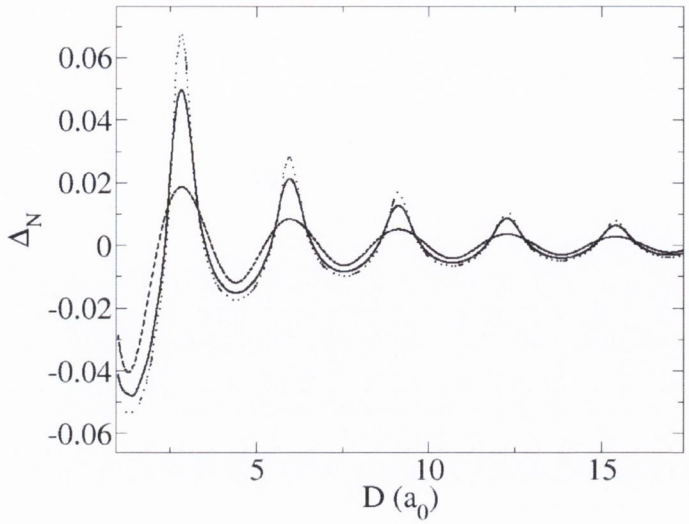

Figure 4.3: Relative energy change per perturbation for a one-dimensional free electron gas perturbed by a series of equally spaced delta-function scatterers for (i) 2 scatterers (dashed line), (ii) 7 scatterers (continuous line), (iii) Infinite number of scatterers (dotted line). Δ_N is a dimensionless quantity, and is defined in Eq. (4.25). The amplitude of the scattering potential is $\lambda = -0.3$ in all cases. The distance between successive minima (maxima) is $\frac{\pi}{k_F}$, where k_F is the Fermi-wavenumber of the gas.

$$
\begin{aligned}
&= g_{00}\left(\frac{e^{iak_p}}{e^{iak}-e^{iak_p}}+\frac{e^{iak_p}}{e^{-iak}-e^{iak_p}}+1\right)\\
&= g_{00}\left(\frac{e^{iak}}{e^{iak}-e^{iak_p}}+\frac{e^{iak_p}}{e^{-iak}-e^{iak_p}}\right).
\end{aligned}
\tag{4.24}
$$

Results and interpretation

To illustrate the separation dependence of the total energy for a given configuration, we study the dimensionless quantity $\Delta_N(D)$ defined as

$$
\Delta_N(D) = \frac{\delta\epsilon_N(D) - N\delta\epsilon_1}{N|\delta\epsilon_1|}. \tag{4.25}
$$

Fig. 4.3 plots this quantity as a function of the spacing D for different values of N. Also depicted is the limiting case for $N = \infty$. In this case, the expression for

$\delta\epsilon_\infty$ becomes

$$\delta\epsilon_\infty(D) = \frac{D}{2\pi^2}\int_{-\frac{\pi}{D}}^{\frac{\pi}{D}} \mathrm{d}k_x \int_{-\infty}^{E_F} \mathrm{d}E \ \mathrm{Im}\left(\log\left(1-\lambda\left\langle k_x,0\right|\hat{g}\left|k_x,0\right\rangle\right)\right). \quad (4.26)$$

As anticipated previously, the total electronic energy depends non-monotonically on the perturbation spacing D and each curve for $\Delta_N(D)$ shows a series of regularly spaced minima. This non-monotonicity points to the existence of preferential separation values for which the total electronic energy is minimised. The overall trend of damped oscillations corroborates the expected result that only in the asymptotic limit of infinitely large separation D does the total energy $\delta\epsilon_N(D)$ agree with $N\delta\epsilon_1$. If we choose units such that $m_e = \hbar = 1$ the Fermi vector of the host gas is given by the equation $E_F = \frac{k_F^2}{2}$. The hypothesis that these oscillations result from quantum interference effects that reflect the electronic characteristics of the embedding electron gas is supported by the fact that neighbouring energy minima are separated by $\frac{\pi}{k_F}$, k_F being the Fermi wave vector of the gas, a quantity independent of the details of the perturbation.

4.2.3 Perturbed Free Electron Gas in 2D

Next, we extend the above argument to deal with 2-dimensional perturbations. This is an intermediate step in our calculation, that should serve as a limiting case to model a tube of infinite radius. As shown in Fig. 4.2, a helically symmetric delta function potential surrounding an infinitely long nanotube can be represented by an array of equally spaced line delta functions spanning the finite-width stripe that one obtains from unwrapping the tube. To characterise a tube, this unwrapped representation must include periodic boundary conditions, equivalent to juxtaposing identical stripes (as per Fig. 4.2b). This gives a 2-dimensional array of infinitely long linear delta functions that can be mathematically expressed as $V(x,y) = \lambda\sum_j \delta(x - jD)$.

Similarly to the one-dimensional case, we calculate the total energy variation due to the introduction of a single line delta function, and then generalise to an infinite number of equally spaced perturbations. In the single line case, the major difference with the 1-dimensional case lies in the utilisation of a Fourier transform along the translationally invariant y-direction. This leads to a new mixed representation $|x, k_y\rangle$ in which the y direction is treated in reciprocal space while the x direction remains in real space. Adopting the same notation as before, it is straightforward to show that the energy variation per unit length of perturbation due to a single line delta function located at $x = x_0$ becomes

$$\delta\epsilon_1 = \frac{1}{2\pi^2}\int_{-\infty}^{\infty} \mathrm{d}k_y \int_{-\infty}^{E_F} \mathrm{d}E \,\mathrm{Im}\log\left(1 - \lambda \left\langle x_0, k_y\right| \hat{g} \left|x_0, k_y\right\rangle\right). \tag{4.27}$$

One major difference between this expression and that in Eq. (4.3) is that this value is the energy per unit length of perturbation. The other substantiative differences are in the appearance of an integral over k_y and also in the new GF matrix element $\langle x_0, k_y| \hat{g} |x_0, k_y\rangle$.

For the case of an infinite number of line delta functions separated by a common distance D, the total energy change $\delta\epsilon_\infty$ per length of perturbation is given by the similar expression

$$\delta\epsilon_\infty = \frac{D}{4\pi^3}\mathrm{Im}\int_{-\frac{\pi}{D}}^{\frac{\pi}{D}} \mathrm{d}k_x \int_{-\infty}^{\infty} \mathrm{d}k_y \int_{-\infty}^{E_F} \mathrm{d}E \,\log\left(1 - \lambda \,\left\langle k_x, 0, k_y\right| \hat{g} \left|k_x, 0, k_y\right\rangle\right) \tag{4.28}$$

where the first index of the ket $|k_x, 0, k_y\rangle$ corresponds to the discrete symmetry in the x-direction, the second the $x-$position of the perturbation inside the uit cell, while the third reflects the continuous symmetry in the $y-$direction. It is straightforward to show that the GF in this new basis reads the same as Eq. (4.4), albeit with E

replaced by $E - \frac{k_y^2}{2}$:

$$\langle x_0, k_y | \, \hat{g} \, | x_0, k_y \rangle = -i \sqrt{\frac{1}{2(E + i0^+ - k_y^2/2)}}. \tag{4.29}$$

The integration limits for the k_x integral in Eq. (4.28) reflect the periodicity along the x direction whereas those for the integral over k_y reflects the free-electron character in the direction parallel to the perturbation.

Again $\Delta_N(D)$, as per Eq. (4.25) is useful to elucidate the distance dependence of the total energy as a fraction of the overall interaction. Shown in Fig. 4.4a for $N = \infty$, the expected non-monotonicity of $\Delta_\infty(D)$ is confirmed, again hinting at the existence of preferential values for the spacing D. Such preferential spacings should correspond to preferential wrapping angles θ, as the two quantities are directly related.

This speculation can be tested only if boundary conditions appropriate for helically wrapped tubes are imposed. This requires the following quantization conditions for the variables k_x and k_y:

$$k_y = -\left(\frac{1}{\tan\theta}\right) k_x + \frac{m}{R \sin\theta}\,, \tag{4.30}$$

where m is an integer, and $\theta \neq 0$. Each value of m defines a different straight line in reciprocal space that labels the possible electronic states in the system. The slope of those lines is evidently θ-dependent and the spacing between them is inversely proportional to the tube's radius. Rather than spanning an infinite-long stripe of finite width, the integration over k_x and k_y appearing in Eq. (4.28) must then be performed under the constraint imposed by Eq. (4.30), that is, k_x and k_y vary over a set of discrete lines. Our speculation is finally confirmed after $\Delta_N(D)$ is evaluated with the aforementioned quantization constraints and still displays similar non-monotonic behaviour in the separation-dependent total energy. Fig. 4.4b

plots Δ_∞ as a function of D for a tube of radius $R = 5a_0$ and two arbitrary values of E_F. The periodicity of $\Delta_\infty(D)$ depends on the Fermi level but all curves display several minima at specific values of D. Following Fig. 4.2b, the relation $D = 2\pi R\cos\theta$ means that preferential values for the spacing D correspond to energetically favourable wrapping angles θ. This is confirmed in the inset of Fig. 4.4 that shows how the total energy scales with the angle θ.

As far as the electronic contribution to the total energy is concerned, the existence of preferential coiling angles does not determine the final wrapping direction of one-dimensional strands surrounding a nanotube. This must obviously be weighed against other energy contributions such as the elastic cost of folding the strands as well as other geometrical factors [28]. Only the balance from all these contributions can determine the overall favourable alignment. In fact, according to Fig. 4.4b, the optimal angle that minimises the total electronic energy is close to $\theta = \pi/2$. This wrapping angle would bring significant costs in terms of elastic energy. A compromise angle is likely to arise as a result of the adequate balance that accounts for the different contributions to the energy. Although the simplicity of our model is not capable of addressing the precise weights in this balance, it serves the purpose of pointing this contribution as a possible mechanism that favours chiral order without depending on the underlying atomic structure.

Generally, the electronic structure of carbon nanotubes is poorly described within a free electron gas model. However, the electronic structure of nanotubes is known to be well described by the simple single-orbital tight-binding model. To test whether the non-monotonicities of the total energy also appear in such more realistic models, we have performed similar calculations within the tight-binding model, which I present in the next section.

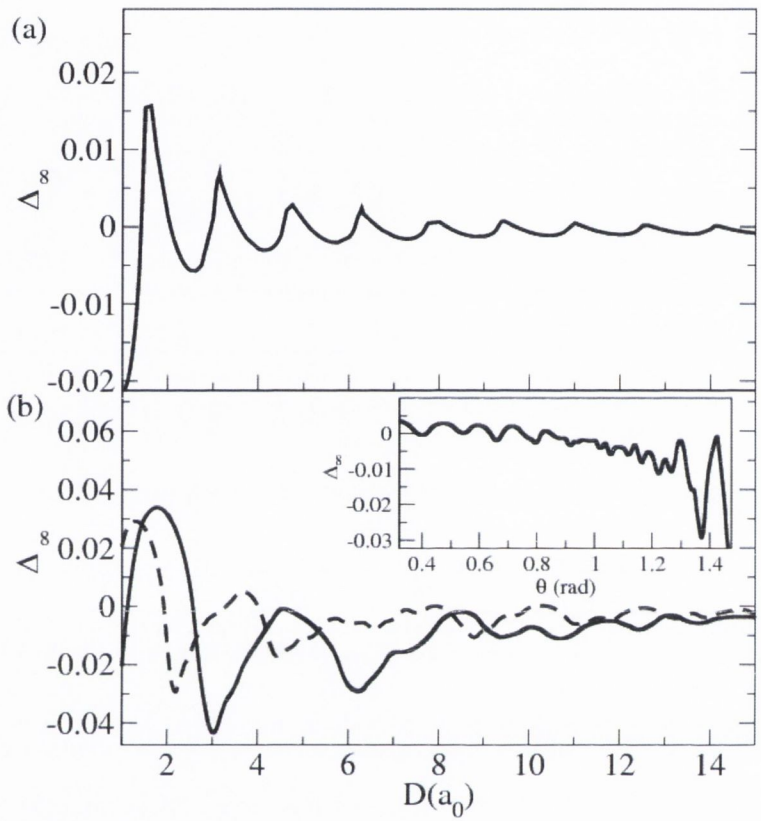

Figure 4.4: Dimensionless relative energy change, as defined in Eq. (4.25), taken per unit length of perturbation for (a) a two-dimensional free electron gas perturbed by an infinite array of equally spaced delta-function scatterers ($E_F = 2.0$) and (b) a free electron gas cylinder in the presence of a coiling perturbation for two separate Fermi levels ($E_F = 0.5$, solid line and $E_F = 1.0$, dashed line). A series of energy minima is obtained, indicating the existence of energetically favourable coiling angles. Inset in (b) is a graph of Δ_∞ as a function of the coiling angle θ. The amplitude of the scattering potential is $\lambda = -0.3$ in all cases. The distance between successive minima (maxima) is again seen to be $\frac{\pi}{k_F}$, where k_F is the Fermi-wavenumber of the gas.

4.3 Tight binding studies

While the preceeding section details one mechanism whereby chiral order can be introduced into a system where none previously existed, there is still the strong suspicion that such a simple model may miss some important underlying features. In this section the detailed atomic structure of the underlying tube is assumed to be important, and the electronic structure is no longer treated as an electron gas. Again, we consider the case of a coiling charged polymer, whose presence is accounted for by assuming that what lies in its neighbourhood becomes polarised. In this case, it polarises some of the carbon atoms on the tube. The polarised atoms will follow the same helical path as the charge distribution and thus acquire a different on-site energy to their non-polarised counterparts.

Under the initial assumption that these bulky molecules cannot resolve the atomic structure of the underlying lattice [28, 84], the tubes may then be exposed to two different helical pitches: the intrinsic chirality of the nanotube and that associated with the wrapping potential. For simplicity's sake, we treat the wrapping molecule as a continuous charge distribution of uniform width wrapped around the nanotube at a constant angle θ, as depicted in Fig. 4.5. We assume that the induced polarisation represented by the perturbing potential in Eq. (3.2) affects all carbon atoms immediately below the charged stripe in an identical fashion. The lateral dimension of the wrapping molecule, together with the distance of the molecule from the tube, determines the width W of this stripe. In principle, the angle θ may bear no direct relation to the chiral angle α of the underlying nanotube, and we treat these two parameters as both being independent. It is our goal here to investigate the effect that this combination of chiralities may have on the nanotube band structure and, in particular, on its electronic density of states (DOS).

In this model, nanotubes are described by the following effective tight-binding

Hamiltonian

$$\hat{H}_0 = \sum_{j,j'} |j\rangle\gamma\langle j'| \ , \tag{4.31}$$

where $|j\rangle$ represents the π-orbital centred at atom j, $|j'\rangle$ is a nearest-neighbour orbital centred on atom j', and γ is the nearest-neighbour electronic hopping, which we will choose to be our energy unit. The total Hamiltonian is given as $\hat{H} = \hat{H}_0 + \hat{V}$, where

$$\hat{V} = \sum_{m} \lambda |m\rangle\langle m| \tag{4.32}$$

accounts for the polarisation of the perturbed atoms under the stripe. Here, m labels those atoms affected by the proximity to the wrapping molecule and λ represents the corresponding shift in their on-site potential due to the induced polarisation. λ can in principle be determined in accordance with the measured binding energy between the nanotube and its wrapping molecules. Also, the fact that ionic doping agents can affect the amount of charge carried on the DNA backbone suggests that we may consider a range of values for λ, which we will for the moment regard as a free parameter.

To assess how the electronic structure of a nanotube is influenced by the wrapping potential, I have performed a systematic study of how the electronic DOS is affected as some of these different parameters are varied. In particular, we will take advantage of the fact that the quasi-one-dimensional nanotubes have densities of states containing several distinctive van Hove singularities (VHS). These are located at values of energy for which an arbitrarily large number of electrons can be in states of the same energy. Consequently, allowed transitions between van Hove singularities is a key feature of the optical absorption spectrum. By locating these singularities and tracking how they evolve as the aforementioned parameters are varied, one can view, at least from a qualitative point of view, how nanotubes respond to such perturbations. Such response could, in principle, be tracked by comparing the optical absorption spectrum of coated nanotubes with that of pristine tubes.

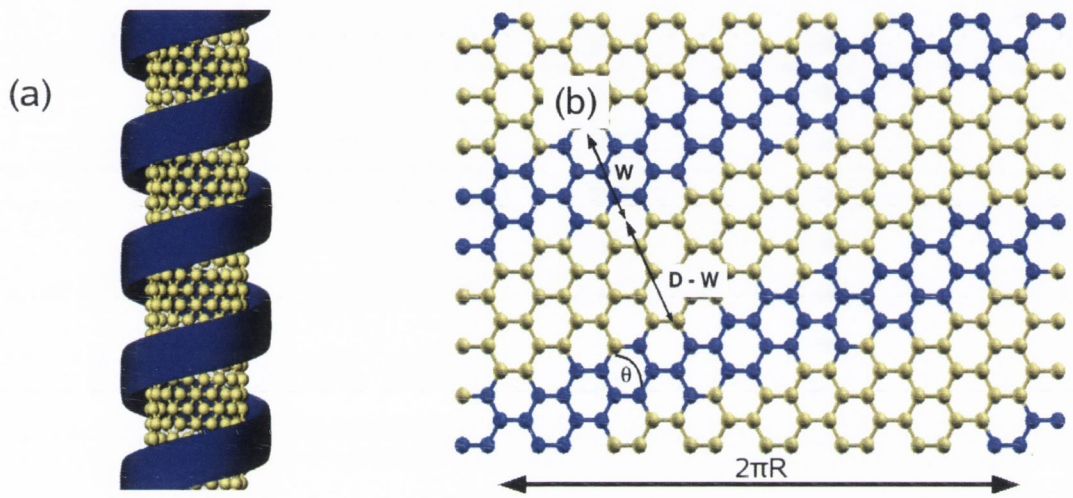

Figure 4.5: Schematic representation of a helically wrapped nanotube. In (a) we display a polymeric molecule represented by a continuous charge distribution of constant width W coiling at an angle θ around the surface of the nanotube. In (b) we display the corresponding geometry in the unwrapped representation. The atoms to be perturbed are indicated by the dark (blue) balls, while the unperturbed atoms are the light (yellow) balls. D is defined in the picture as the distance between equivalent atoms of neighbouring stripes. Also depicted is the circumference of the nanotube ($2\pi R$) where R is the nanotube radius.

The sequence adopted in this section is as follows: in the next section, we discuss the details of our calculations, as well as defining some useful concepts; in the following section, we present results for the dependence of a few physical observables on the microstructure parameters λ, θ and W; and in the final section we present conclusions and discussion.

4.3.1 Calculational details

To calculate the electronic structure of the system in the nearest neighbour tight-binding model, we have directly solved the Schroedinger equation in reciprocal space, which requires the introduction of a repeating unit cell. We assume that the perturbing potential makes P full twists in the space of Q primitive unit cells of the nanotube, and that P and Q are positive integers with no common factor. Then if $\vec{T}$ is the translational vector of the nanotube's unit cell, the perturbed structure is periodic along the tube axis (chosen as our $z-$axis), with period $Q|\vec{T}|$. As a concrete example, the system depicted in Fig. 4.5b has $P = 2$, $Q = 9$, and $\vec{T} = a\hat{z}$, where a is the distance between two crystallographically equivalent atoms in a graphene lattice, and $\hat{z}$ is a unit vector along the tube axis. The coiling angle is given by the formula

$$\theta = \arctan\left(\frac{P|\vec{C}|}{Q|\vec{T}|}\right), \tag{4.33}$$

where $\vec{C}$ is the chiral vector of the tube. While it is conceivable that the perturbation could follow an incommensurate configuration ($\frac{P}{Q}$ irrational), it is also clear that the coiling angle appropriate to that system will lie arbitrarily close to that of a commensurate system, provided we allow P and Q to be sufficiently large.

Since we have now constructed a periodic system, we can apply Bloch's theorem to write $\hat{H} = \sum_k \hat{H}_k$, where k is the wave number in reciprocal space. If there are N electronic states in this supercell, for each value of $k \in [0, \frac{2\pi}{Q|\vec{T}|})$ we must diagonalise the square matrix $\langle l| \hat{H}_k |m\rangle$ to obtain the N eigenvalues ω_{jk}.

To construct the density of states per atom, $\rho(E)$, we use the eigenvalue representation for the single particle Green function as discussed in chapter 2:

$$\rho(E) = \frac{-Q|\vec{T}|}{2\pi^2}\mathrm{Im}\left(\int_0^{\frac{2\pi}{Q|\vec{T}|}}\mathrm{d}k \sum_{j=1}^{N}\frac{1}{(E+i\eta)-\omega_{jk}}\right). \tag{4.34}$$

Once we have the DOS per atom, we can calculate auxiliary quantities such as the Fermi level of the composite material, determined by demanding that

$$\int_{-\infty}^{E_F}\rho(E) = 1 + \Delta C \tag{4.35}$$

This last follows from the observation that there should be one p_z electron per carbon atom on the average, while allowing the possibility that the interaction causes some charge to be transferred from the wrapping molecule to the nanotube. Since the perturbation is spatially extended, the Fermi level of the composed system will in principle differ from that of the unperturbed system, in contrast to the case of a localised perturbation. While we have not here considered charge transfer between the sub-systems, such a constraint can easily be relaxed in our approach by appropriately modifying the RHS of Eq. (4.34) as described.

Of particular interest to us is the behaviour of the DOS. The DOS of a semiconducting nanotube in the absence of a perturbation can be characterised by a diameter dependent energy gap, together with a series of van Hove singularities. For perturbation free metallic tubes, similar peaks are separated by a flat, dispersion-less region about the Fermi level. However, it can be shown that the metallic character of these tubes is sensitive to various perturbations. Perhaps the most famous of these is the fact that zig-zag nanotubes, which otherwise would be considered as metallic, display curvature induced mini-gaps. The cases we have considered have proved no different: in every case tested, we have seen an induced mini-gap due to the helical perturbation. However, we will show that under certain circumstances, these gaps are so small that it is likely that this effect will be masked by thermal

effects, or perhaps by charge transfer between the parts. Even so, it is important to quantify the size of these gaps, so that we can identify at what temperature such effects will become apparent. The characterisation of these mini-gaps as a function of the perturbation parameters has been one aim of this work. More specifically, we have investigated how the VHS (and thus indirectly the optical transitions) change in response to the three independent parameters that characterise the perturbation, θ, λ and W.

4.3.2 Location of van Hove singularities

It is well known that the VHS associated with a SWNT have a simple geometric interpretation. The Brillouin zone of graphene corresponds to a hexagon in reciprocal space, and the effect of wrapping a graphene sheet into a nanotube confines the electronic wavefunction in the circumferential direction. This leads to a quantization of the circumferential component of the wave vector. Accordingly, the electronic structure of the resulting nanotube is obtained by considering only those states which lie in a series of discrete equally spaced lines overlaid on the Brillouin zone of graphene. If one plots the iso-energy surfaces for the graphene sheet for different energies, one sees that the VHS in the DOS of the nanotube correspond precisely to those energies where the allowed wave vector lines touch the iso-energy surfaces tangentially.

One can apply the same reasoning in the case of our perturbed system. In this case, however, the Brillouin zone will be contained in a parallelogram, due to the oblique shape of our real space unit cell. Again, the spatial confinement of the electronic wavefunctions induces a wave vector quantization. Unsurprisingly, the VHS of the composed system can be tracked in the same fashion as in the case of the unperturbed system, as the points of tangency of these quantized lines to the iso-energy surfaces appropriate to the perturbed system. It is worth stressing that the constant-energy surfaces are no longer determined by the electronic structure of a simple graphene sheet. In this case, it corresponds to the electronic states

associated with a sheet of hexagonally ordered atoms whose on-site potentials display the striped geometry depicted in Fig. 4.5b. This is illustrated in Fig. 4.6. On the left panel, Fig. 4.6a, we plot the DOS of a (4,4) nanotube perturbed by a helical potential defined by $\theta = \pi/3$rad, $W = 2.0$ Åand $\lambda = -0.3\gamma$. Two vertical dashed lines are also included, one at $E = 0.0$ and another at $E = 0.63\gamma$. The former (thick line) marks the on-site energy of the unperturbed carbon atoms and the latter (thin line) coincides with a VHS displayed in the DOS. The right panel, Fig. 4.6b, shows the corresponding constant-energy plots in reciprocal space superimposed with equally spaced lines representing the allowed wave vectors that the electronic states can have. Once again the thick-line iso-surface corresponds to $E = 0$ whereas the thin-line curves are associated with $E = 0.63\gamma$. It is evident that, for $E = 0$, the iso-surface intersects (non-tangentially) the quantized wave vector lines indicating the existence of extended electronic states at that energy, also confirmed by the finiteness of its DOS. In contrast, for $E = 0.63\gamma$, the thick-line iso-surface tangentially intersects the quantized lines, proving that the geometrical interpretation mentioned above is also valid for the nanotube in the presence of the helical perturbation. With such a simple geometrical picture, one can easily trace how the VHS positions are affected by the helical potential. Bearing in mind that optical transitions are usually dependent on the distance between neighbouring VHS, this picture seems useful to study how the electronic structure of a nanotube is affected by the wrapping perturbation. In what follows we adopt the standard notation of $M_{j,j}$ and $S_{j,j}$ for the separation between the j^{th} VHS for metallic and semiconducting tubes, respectively. Following a similar notation, we represent the perturbation-induced mini-gaps in metallic tubes by the quantity m_{11}.

4.3.3 Width dependence of perturbation

The effect of the helical potential on the nanotube atoms can be separated into two disjoint contiguous subsets: a stripe of polarised atoms, and another in which the

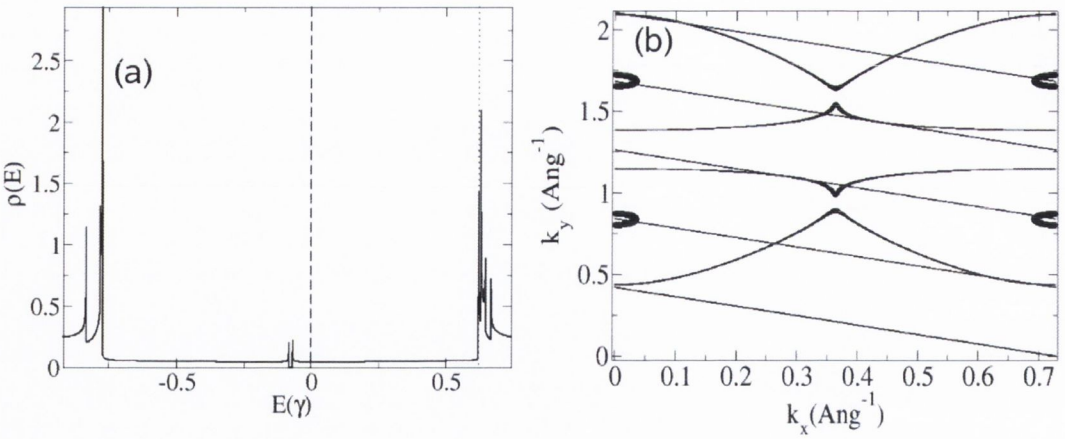

Figure 4.6: (a) The DOS for a (4,4) armchair nanotube perturbed at an angle of $\theta = \frac{\pi}{3}$rad by a 2.0Å wide stripe of amplitude $\lambda = -0.3\gamma$. The dashed line corresponds to the onsite energy of the unperturbed nanotube, while the dotted line marks the maximum of the first VHS above the Fermi level. (b) The corresponding energy iso-surfaces in reciprocal space for a graphene sheet perturbed by a series of equally spaced stripes. The straight lines depict the quantized wave vectors that are permitted due to the boundary conditions. Two distinct iso-energy surfaces are presented, corresponding to the two energies highlighted in (a). The iso-surface corresponding to the VHS energy is seen to touch the lines of quantization tangentially, in contrast to that of the lower energy.

atoms are unperturbed. W is an upper bound for the perpendicular distance between any two perturbed atoms, as measured normal to the direction of the perturbation. Following Fig. 4.5b, we define D as the distance between two equivalent atoms of neighbouring stripes. It follows from these definitions that W must range between 0 and D. It is worth noting that stripe widths such that $W/D \approx 0$ (low coverage) are somewhat equivalent to the cases of nearly full coverage in which $W/D \approx 1$. In each of these limiting cases, we expect the shape of the DOS to approach that of the uniform tube, albeit in the second case with a rigid shift of its centre of mass from $E_F = 0$ to the value $E_F = \lambda$. Despite the fact that W can take any value in the range $[0, D]$, the dependence of the quantities of interest as a function of W must acquire a step-like quality. This is because for any value W, there is a minimum quantity ΔW that the stripe must be widened by in order to contain a new perturbed atom. This is illustrated in Fig. 4.7a where we show how m_{11} depends

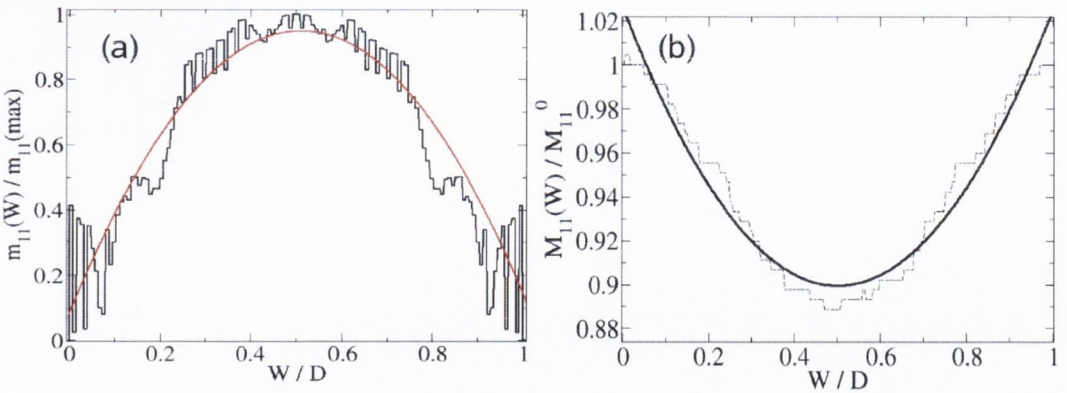

Figure 4.7: (a) Dependence of the m_{11} on the width W for an (18,0) nanotube coiled by a uniform stripe at angle $\theta = 0.978$rad and $\lambda = -0.3\gamma$. The maximum value of m_{11} occurs at $W/D = 0.5$ and is used here as a reference. The smooth solid line is a quadratic fitting. The overall trend is of a non-monotonic increase in the perturbation-induced mini-gap. (b) Dependence of the transition M_{11} on the width W for the (18,0) nanotube (dashed, black curve) together with a quadratic regression (continuous curve) in units of the unperturbed transition $M_{11}^0 = 0.57\gamma$. $\lambda = -0.3\gamma$ in all cases. The overall trend is towards a red-shifting of the transition, with a energy change of at most about 11%.

on W for an (18,0) nanotube with $\lambda = -0.3\gamma$ and $\theta = 0.978$rad. Plotted in units of m_{11} for $W/D = 0.5$, which is the maximum value for the mini-gap ($m_{11} = 0.0056\gamma$), we see that the mini-gap scales approximately quadratically with the ratio W/D. The locations of the main VHS are also affected by the perturbation. In this case, the energy distance between the first VHS on either side of the Fermi level, here labelled M_{11} by analogy with the unperturbed tube, is plotted in Fig. 4.7b as a function of the width W for the same set of parameters, in units of the unperturbed transition energy M_{11}^0. Once again the step-like behaviour of the calculated results are smoothed by fitting the curve to a quadratic regression to the data points. The overall trend is towards a red-shifting of the transition, with a maximum change of approximately 11%. The duality between the unperturbed and the perturbed atoms is highlighted by the degree to which the curve is symmetric about the point $W/D = 0.5$.

4.3.4 Angular dependence of perturbation

An interesting question to ask is what is the qualitative behaviour of the quantities of interest when the angle θ is varied. In our scheme, the coiling angle is given by the formula

$$\theta = \arctan\left(\frac{P|\vec{C}|}{Q|\vec{T}|}\right), \tag{4.36}$$

where $\vec{C}$ is the chiral vector of the tube. While it is conceivable that the perturbation could follow a truly incommensurate configuration ($\frac{P}{Q}$ irrational), it is also clear that the coiling angle appropriate to that system will lie arbitrarily close to that of a commensurate system, provided we allow P and Q to be sufficiently large. Since we must have a periodic system, θ cannot be varied continuously, but must increase in discrete steps, similarly to the width-dependence results presented above. We have investigated the angular dependence of these quantities for an $(18, 0)$ zigzag nanotube. Such a tube is an ideal candidate for these investigations since the fundamental unit cell is only $\frac{2a}{\sqrt{3}}$ in length, but $18a$ in width, where a is the lattice parameter of the graphene structure. This allows one to consider a wide range of angles. Holding both the width of the stripe $W = 6.7$ Å and the amplitude of the perturbation $\lambda = -0.3\gamma$ constant, Fig. 4.8 shows both m_{11} and M_{11} transitions as a function of the coiling angle. Panel (a) displays m_{11} in units of γ for various coiling angles and panel (b) does the same for M_{11} in which it is expressed in units of the unperturbed transition M_{11}^0. Each graph has a smoother curve acting as a guide to the eye which reflects the overall trend of the above quantities and how they depend on the coiling angle. What is evident from panel (a) is that the stepwise fluctuations that surround the smooth curve becomes much more pronounced at values of θ corresponding to coiling angles that are perfectly commensurate with the high symmetry directions of the nanotube. In those cases the perturbation-induced mini-gaps can be as large as 40 meV. As far as the M_{11} transition is concerned, one can clearly see in panel (b) that at low coiling angles there is a noticeable blue-

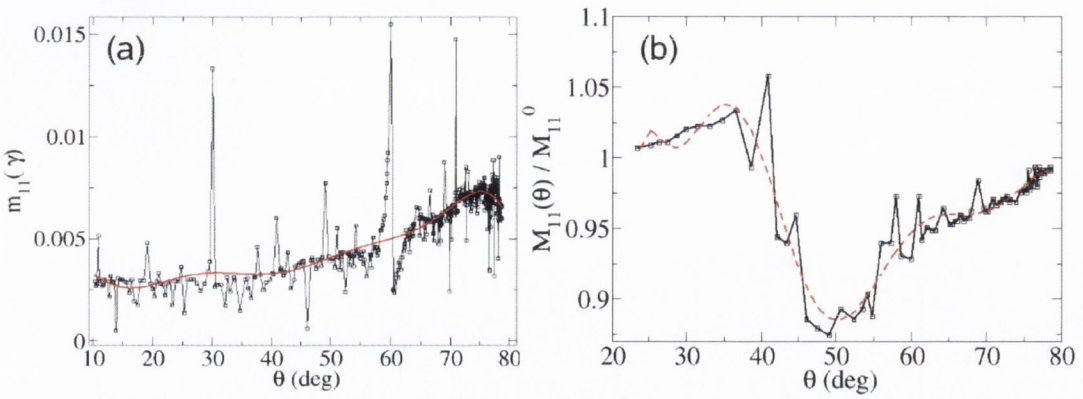

Figure 4.8: (a)A plot of m_{11}, for various coiling angles (full line, with points). This plot is in units of γ. (b) A plot of the energy difference between the two VHS on either side of the Fermi level for an (18,0) zigzag nanotube (corresponding to the M_{11} transition in the pure tube) for different coiling angles. The plot is normalised to the size of the transition for the clean tube M_{11}^0). The amplitude of the perturbation is held constant at -0.3γ, and so is the width of the perturbation at $W = 6.7$ Å. The smooth lines corresponds to a high order polynomial approximation to the curve, and are intended as a guide to the eye.

shifting of the transition, whereas at mid to high coiling angles there is a decrease in the transition energy. Such a non-monotonic behaviour in the angle-dependent electronic structure has been reported for the case of helical short-range potentials in cylindrical geometries [84].

4.3.5 Amplitude dependence of perturbation

Intuitively, one expects that the features of the DOS investigated here will vary continuously as a function of the parameter λ, in contrast to the discontinuous behaviour found as a function of W and of θ. This would mean that the VHS separations should vary continuously as a function of the perturbation amplitude. As depicted in Fig. 4.9, we indeed find that they depend continuously on the amplitude of the perturbation λ. In the case of the $(6, 0)$ zigzag and $(6, 6)$ armchair nanotubes which are metallic in the absence of a perturbation, we find that for small perturbation amplitudes, the mini-gaps grow monotonically as we increase the magnitude of the perturbation. In contrast, for the semiconducting (7,0) tube,

we see the opposite trend in S_{11}. In this case, the gap decreases as a function of λ. This shows that as we increase the strength of the helical perturbations, metallic tubes are driven into becoming more semiconducting-like; whereas the originally semiconducting tubes undergo a reduction in the size of their gaps.

The systematic study carried out above shows how the DOS may respond to a coiling perturbation that represents the effect of helically wrapping molecules surrounding a nanotube. Two characteristic features of the DOS were investigated, namely the perturbation-induced mini-gaps m_{11} as well as those associated with the transitions M_{11} and S_{11}. They were shown to depend on the characteristic features of the perturbing potential such as the wrapping angle θ, the polarising width W and the strength of the polarising potential λ. More than a purely academic exercise, this is a valuable point to assess how some physical quantities may respond to the presence of a wrapping charge distribution.

For the sake of illustration, rather than treating λ as a free parameter, it is instructive to estimate its value by equating the perturbation-induced change in total energy to the measured binding energy between the wrapping molecules and nanotubes. While the polarisation interaction is certainly not the only component of the measured binding energy, under the assumption that other contributions such as the elastic energy and the van der Waals interaction are small, it will be the dominant contribution. This allows us to estimate how strongly bound the parts must be before any perceptible change occurs in the DOS. Following Fig. 5a, absent any charge transfer, we find that to open a gap comparable to room temperature requires a value of λ of about 1eV in the case of a wrapped (6,6) nanotube, and that larger mini-gaps require monotonically larger λ. For the case of organic polymers, [87] we find the magnitude of λ to be too small to produce a mini-gap of this magnitude. Likewise, for the case of undoped DNA molecules [88] it is also not sufficiently strong to produce significant alterations in their electronic structure features. These examples seem too weakly bound to produce dramatic changes in the electronic

structure of the host nanotube. This suggests that extra charge must be required on the backbone of the wrapping molecule to increase its polarising effect and, in turn, its binding energy. In fact, ionic doping has been reported to affect the optical response of DNA-nanotube composites [89] by increasing the amount of charge on the DNA backbone, which seems consistent with our findings.

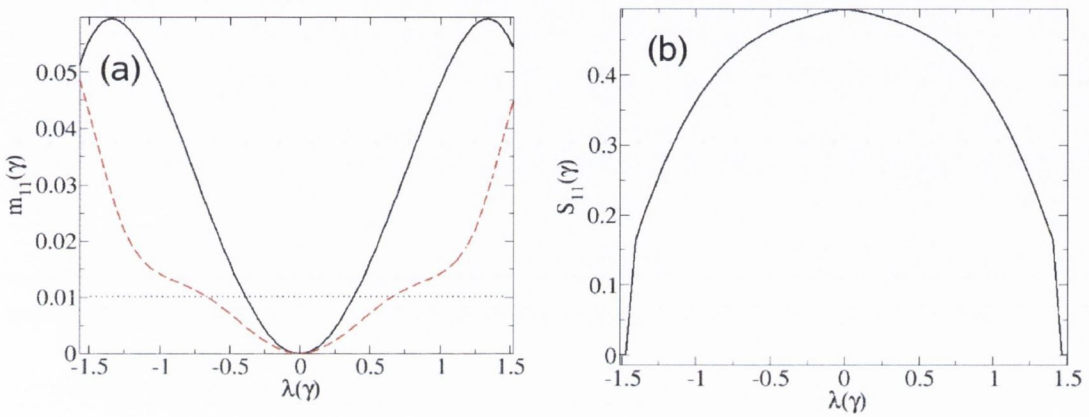

Figure 4.9: (a) A plot of the size of the mini-gap m_{11} as a function of the polarisation strength parameter λ for two different chiralities and coiling angles. The solid (black) curve corresponds to a (6,6) nanotube perturbed by a stripe at an angle of 64.3°, while the dashed (red) curve corresponds to a (6,0) nanotube subject to a stripe at an angle of 34.7°. The dotted line indicates where the mini-gap energy is equivalent to room temperature. In (b) we plot the fundamental semiconducting transition as it depends on the perturbation amplitude for a (7,0) nanotube wrapped by a stripe at angle 39.0°. A monotonic red shifting of the gap is observed in the range of interest. In all cases the width of the perturbation is 5.33Å.

4.3.6 Angular dependence of change in electronic energy

Similarly to the electron gas case, we can use the variation in the density of states to evaluate the energy variation due to the introduction of such a polarising perturbation. Fig. 4.10 shows the results for the tight-binding calculations of a (9,0) zigzag nanotube wrapped by a thin charge distribution that form an angle θ with the tube axis. The non-monotonicity in the angular dependence of the total energy can also be seen in this case, proving that it is not an exclusive feature of the electron gas model. It is worth noting that in addition to a non-monotonic smooth curve

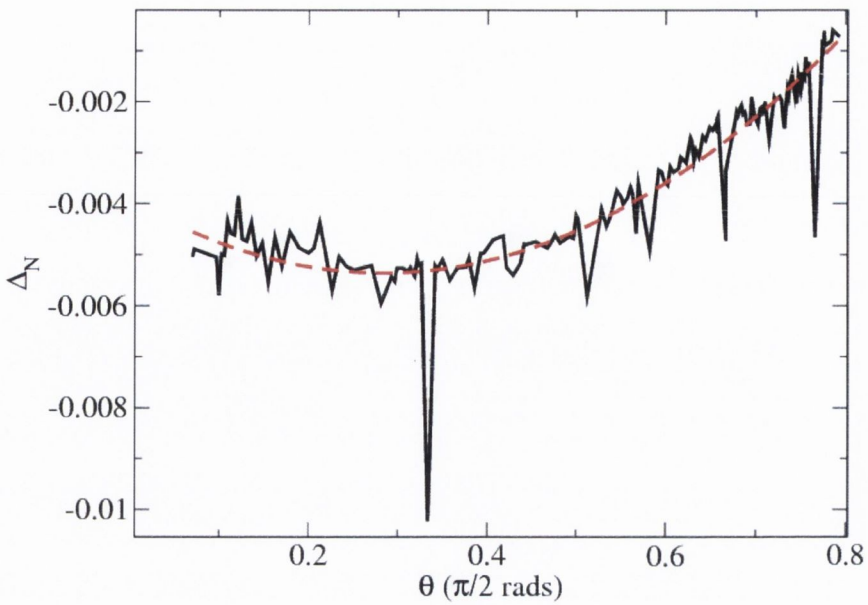

Figure 4.10: Angular dependence of the relative energy change Δ_N for helical wrapping on a (9,0) zigzag nanotube. An overall non-monotonic trend depicted by the dashed line is superimposed by strong fluctuations that correspond to high-symmetry angles of the perturbation, as well as the discontinuous nature of the change in the perturbation.

depicted by the dashed line, strong fluctuations are also identified which are most pronounced at the high-symmetry angles of the tube. Although these narrow-angle fluctuations may be reduced, for instance by increasing the width of the linear charge distribution, we have found that the smooth behaviour depicted by the dashed line is robust enough to remain in other geometries and configurations.

4.4 Chapter Summary

We have performed a systematic study of the effect of a coiling, polarising potential on the electronic structure of carbon nanotubes. Utilising Lloyd's formula, we have shown that the electronic contribution to the total energy of nanotubes wrapped by helical continuous charge distributions displays a non-monotonic behaviour as a function of the wrapping angle, using both a free electron approach and a tight binding one. The origin of these oscillations can be understood as a result of the

formation of an interference pattern in the electronic wave functions. Following an analogy drawn with the Kronig-Penney model, it is simple to understand the origin of these total energy oscillations on a helically-wrapped nanotube. The proximity of the continuous linear charge distribution polarises the nanotube and induces a localised short-range potential that affects the electronic structure of the tube. These localised potentials produced by different sections of the wrapping strand generate a quantum interference pattern that appears in the electronic wave functions of the underlying nanotube. Such a pattern is therefore responsible for the occurrence of the size-dependent oscillations of the total energy.

We have also investigated the dependence of the induced changes in electronic structure on the details of perturbation. The perturbation characterised by the wrapping angle θ, the polarising width W and the polarisation strength λ introduces an additional geometrical chirality that may not necessarily coincide with the intrinsic chiral angle of the nanotube. While the largest changes are seen to occur in cases where this additional chirality is commensurate with the chiral angle of the tube, even when this chirality bears no relation to that of the tube, changes occur. Features of the electronic density of states such as the perturbation induced mini-gaps and the VHS transitions were seen to depend on θ, W and λ with different degrees of sensitivity. Regarding the VHS, a geometrical representation similar to the one used for pure nanotubes was used to trace how those singularities evolved with changes of the perturbation parameters. Furthermore, we have estimated a minimum binding energy between the tube and the wrapping molecules to generate a perceptible change in the electronic DOS. Finally, we found that while it is in principle possible to alter the electronic structure of nanotubes by wrapping a charge distribution around them, noticeable changes tend to occur for the cases in which the binding energy molecules are more strongly bound to the nanotubes. We argue that changes in the optical response induced by ionic doping on DNA-nanotube composites may be one such example.

Chapter 5

Mechanism for mechanical reinforcement in nanotube-polymer composites

5.1 Introduction

The material presented in this chapter is in a somewhat different vein to the rest of the work presented thus-far. While the primary focus of my research has been into the *electronic* properties of nanotube-based hybrid structures, one other interesting area that I have carried out research in has been the mechanical properties of such composites. In particular, work has been carried out into what effect the presence of a nanotube has on the ability of a bonded polymeric molecule to stretch in response to an external stress, and the consequences that this has for the Young's modulus of the composite. While slightly different in thrust, this work still falls within the scope of my thesis on the physical properties of nanotube composites, and as such will be presented here.

While the focus thus-far has been on the electronic properties of nanotubes, another interesting quality that they possess is immense physical strength as well as

near world-record stiffness. In fact, these properties were predicted as a consequence of the particularly strong hybridised bonds between the carbon atoms in the lattice, combined with the cylindrical geometry of the nanotube. In the last few years, careful experiments on individual nanotubes have borne out such predictions.

The possibility of utilising these exceptional mechanical properties at the macroscale is indeed a tantalising prospect. In the previous chapter, I have already mentioned that the nanotube-polymer interaction is one example that illustrates how effectively nanotubes can transform the physical attributes of a composite structure. Mechanically very strong and good conductors of thermal and electronic currents, it is not surprising that nanotubes make excellent fillers in polymeric composite materials and can substantially improve their mechanical, electronic and thermal responses.

One particular area where experiment shows a significant enhancement is in the increase in the Young's modulus of nanotube-polymer composites. This increase is often correlated with the formation of an apparently crystalline layer of polymers surrounding the nanotubes. The evidence for this crystallinity lies in high-resolution microscopy and in differential scanning calorimetry experiments. These last display a so-called melting peak that corresponds to a transition from the ordered to disordered phase. Although the increase in the Young's modulus has been attributed to an improved stress transfer between the stiffer nanotubes and the softer polymer matrix, the actual physical mechanism for this improvement is still unclear. To clarify this matter, we have modeled the polymer-nanotube composite by harmonic chains interacting with a rigid periodic potential, an extension of the so-called Frenkel-Kontorova model. We have identified a possible origin of the reinforcement with the occurrence of a templating transition, in which a fraction of polymers are constrained by the periodic potential of the underlying nanotube.

Concerning the mechanical properties, nanotube/polymer composites provide order-of-magnitude increases in strength and stiffness of thin films when compared to

typical carbon-fibre/polymer composites. Stress-strain measurements in nanotube-polymer composite films find that their Young's modulus can be increased by a factor 4 when less than 1% of nanotubes are added to the polymer matrix [27]. The appearance of large values of reinforcement with such a minute amount of nanotubes has been directly correlated with the formation of a crystalline layer of polymer surrounding the immediate vicinity of the nanotube surface. Further evidence for this correlation is given by the fact that similar nanotubes in the presence of non-crystalline polymers display much lower levels of reinforcement [26]. Concerning the morphology of this crystalline layer, experimental observations at low coverage show that polymers tend to coil at well-defined angles to the nanotube axis. This is consistent with molecular dynamics simulations [77] and agrees with the mathematical concept that strings constrained within a cylindrical geometry are optimally packed in a helical orientation [83]. In fact, a recent macroscopic model describing the basic mechanisms for this type of crystallisation points to a range of preferential coiling angles that polymers may follow when coating the walls of a nanotube [28].

Despite the experimental evidence, there is little convincing theoretical support for the correlation between crystallinity and mechanical reinforcement in polymer-nanotube composites. Based on purely macroscopic arguments, the physical origin of the mechanical reinforcement is commonly attributed to the improved stress transfer that results from the formation of a crystalline coating surrounding the nanotubes. In other words, the rigidity of the embedded carbon nanotubes can only be probed in the composite structure if stress is efficiently transferred across a well-ordered nanotube-polymer interface. Although this must be a relevant factor, it is not sufficient to provide a quantitative description of reinforcement. This is confirmed by the fact that the so-called rule-of-mixtures, displayed in Eq. (5.1), a traditional method for calculating the mechanical response of macroscopic composite structures, overestimates the Young's modulus of nanotube-polymer composites by more than

one order of magnitude.

$$Y_c = Y_a v_a + Y_b v_b \tag{5.1}$$

Here Y_c, Y_b and Y_a are Young's moduli of composite, species a and species b respectively, and v_i is the fraction of species i by volume.

This failure results from the erroneous assumption of perfect stress transfer between the different constituent phases of the composite material. Without a way of quantifying the stress transfer across the nanotube-polymer interface we cannot reproduce the observed levels of reinforcement in a reliable manner.

This does not seem possible in a simple continuum elastic macroscopic formalism and calls for an alternative approach that involves the microscopic structure of the component parts. With such a motivation, in this chapter I have proposed a model that is able to bridge this gap between the micro- and macroscopic scales, giving a quantitative estimate of the stress transfer across the nanotube-polymer interface. As a result, the physical mechanism for the enhanced mechanical response in composite materials is clarified. In addition to reproducing the general trends observed in reinforcement experiments, the model points to a non-monotonic reinforcement dependence on the nanotube diameter. Such a non-monotonic behaviour indicates the possibility of predicting the adequate combination of materials to optimise the mechanical reinforcement in such structures.

As regards layout, this chapter is divided into three sections. The first section describes the geometry of the problem, as well as introducing the calculational method. The second section contains the details of our calculational scheme, as well as an example of a typical calculation, while the third and final section deals with the interpretation of these results. The work presented in this chapter has been published, and can be found in [90].

5.2 Modeling the interaction

5.2.1 Geometry of the problem

We start by modeling the polymer-coated nanotubes as infinitely long cylindrical graphene sheets of radius r wrapped around by semi-flexible strands. Since we are interested in the stress transfer across the polymer-nanotube interface, it seemed sufficient to study this transfer for a single monolayer of polymer coating, under the assumption that there is essentially perfect stress transfer both within each separate phase and between any further interfaces. The polymer strands are represented by monomers separated by harmonic springs of natural length l_0 and lie on a cylindrical surface of radius $R = r + dr$, where dr is the van-der-Waals distance to the tube surface, hereafter considered to be constant ($dr = 3.5$Å). Following experimental evidence [91], we assume that the polymers coil around the nanotube surface at a well-defined angle θ relative to the axial direction, as schematically shown for a single strand in Fig. 5.1. The geometry of this problem is similar to that met in chapter 4. The atomic structure of the nanotube is depicted by the hexagonal lattice both on the cylindrical wall Fig. 5.1a and on the flat surface that results from unwrapping the nanotube Fig. 5.1b.

The effect that the hexagonal potential, produced by the underlying nanotube, has on the ability of the polymer strands to stretch has been investigated to address the issue of stress transfer in crystalline composite materials. Were it to have no effect on their ability to stretch, the polymers which encase the nanotube would bear all of the brunt of a Young's modulus type experiment, and the inherent stiffness of the nanotube would not be probed. In this scenario, no stress would be transferred across the interface. Under those circumstances, the nanotubes would not be able to provide any contribution to the reinforcement, and would contribute only indirectly to the Young's modulus of the composite - perhaps by promoting the formation of a crystalline layer which has itself a Young's modulus higher than that of the

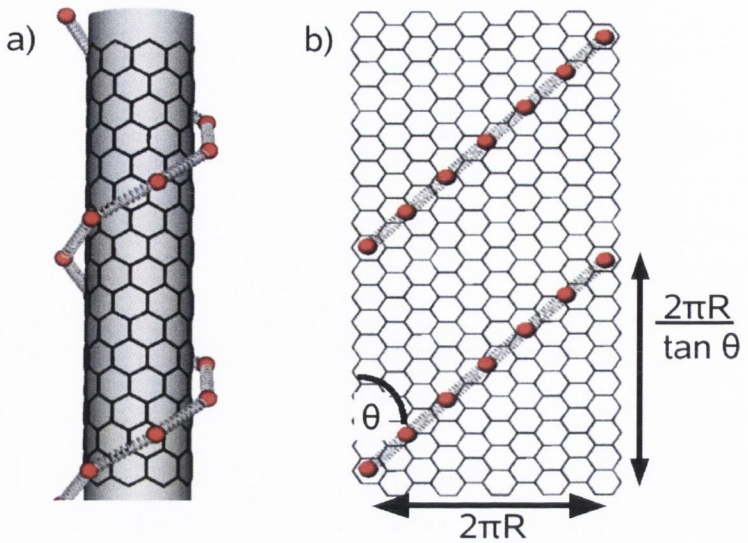

Figure 5.1: Schematic representation of a single polymer strand coiling along the nanotube axis at an angle θ. The strand is represented by monomers connected by elastic springs. In the two-dimensional depiction, the unwrapped tube is represented by a stripe of width $2\pi R$ and the coiling angle θ defines a unit cell of length $2\pi R/\tan\theta$.

amorphous polymeric gel.

5.2.2 Nanotube-polymer interaction and the Frenkel-Kontorova model

With the preceding geometric set-up, the dependence of the Young's modulus of the composite can be investigated and contrasted with that of the polymer matrix. The definition taken of the Young's modulus is the initial slope of a stress-strain curve. That is,

$$Y = \frac{\sigma l_0}{\Delta l}, \tag{5.2}$$

where l_0 is the original length of the sample and Δl is the change in length associated with a stress σ. Accordingly, the higher the Young's modulus of an object, the stiffer it is.

We must then find how the stress-induced strain experienced by a polymer strand is affected by the presence of the hexagonal potential of the underlying nanotube

lattice. A suitable model that accounts for the effect of this potential is the so-called Frenkel-Kontorova model, traditionally used for describing an adsorbed monolayer on an atomically flat surface. In its original form, which describes a harmonic chain of atoms interacting with a periodic one dimensional potential, the model's Hamiltonian takes the form

$$H = \sum_j \left\{ \frac{k}{2}(x_j - x_{j-1} - l_0)^2 + V(x_j) \right\}. \tag{5.3}$$

Taking $V(x_j) = U(1 - \cos(2\pi x_j/\lambda))$, the Hamiltonian represents a one-dimensional system of monomers interacting via harmonic springs, in the presence of an external sinusoidal potential of wavelength λ and corrugation depth U.

The ground state features of this model have been extensively studied in which the static equilibrium configuration of the system results from the interplay of the two characteristic length scales (l_0 and λ), the confining potential U and the resistance to stretching k. It is intuitively obvious that the natural monodisperse distribution of interparticle distances of an isolated chain must be altered by the presence of the external potential, but despite local fluctuations of these distances, the total length of the chain can be fully described by the average inter-particle separation, which will hereafter be denoted by ω.

This quantity can be evaluated by finding the ground-state configuration of the system, for which we used two different approaches; firstly via a force equilibrium approach, and secondly the method of effective potentials due to Griffiths and Chou [92].

5.2.3 The force equilibrium approach

The force equilibrium method relies on the fact that the condition for an equilibrium solution $\{x_j\}$ of Eq. (5.3) is

$$\frac{\partial H}{\partial x_j} = 0 \qquad \forall j. \tag{5.4}$$

Performing the differentiation, it is found that the condition for equilibrium is:

$$x_{j+1} = 2x_j - x_{j-1} + \frac{2\pi U}{k\lambda} \sin\left(\frac{2\pi x_j}{\lambda}\right). \tag{5.5}$$

This gives a recipe for generating equilibrium configurations – pick any two values for x_1 and x_2 (say), and calculate the rest of the x_j recursively using Eq. (5.5). To find a global minimum energy configuration, subsequently evaluate the energy of the configuration using the Hamiltonian function. Performing a two parameter search over x_1 and x_2 to find the pair that minimised the energy function should thus give the ground state configuration.

This algorithm was implemented numerically, but was found not to yield true ground-state configurations. The problem is that the set $\{x_j\}$, generated by this algorithm, is numerically unstable. For example, in the case that $l_0 = \lambda = a$, the ground state solution is, by inspection, $x_j = aj \quad \forall j$. The filtering outlined above was unable to reproduce even this simple case. The reason for this is that the map above is an area-preserving dynamical map which is inherently unstable against round-off error. Consequently, this method had to be shelved, and another approach sought. Thankfully, the method of Chou and Griffiths (described in the next section) provides a computationally efficient way of obtaining the equilibrium positions for the particles that are subjected to the external periodic potential, from which we can then derive the value of ω.

5.2.4 Method of effective potentials

Chou and Griffiths [92] have developed an ingenious method (the so-called "method of effective potentials") of deriving the ground state of a wide range of Hamiltonians similar to that of Eq. (5.3). In the cited paper, they outline an algorithm to find the ground state of the system, through the solution of a non-linear eigenvalue problem. They do this by finding a quantity which they refer to as the "effective potential"

that a monomer feels due to the total potential (internal + external potential energy). The so-called method of effective potentials has by now become a standard tool used to study the ground state of Hamiltonians similar to Eq. (5.3) [93], [94], [95]. A computer program, adaptable to whatever periodic external potential is necessary, was written to implement their algorithm. Their algorithm, which amounts to solving a non-linear eigenvalue problem on a finite real-space grid, is still seen as the most computationally efficient method to find the ground states of Eq. (5.3).

Since we are interested in the mechanical response of the chain in the presence of the periodic potential, we need to investigate how the value of ω depends on the stretching force. The effect of this force can be mapped into an increase of the natural bond length l_0, which makes the function $\omega(l_0)$ the relevant quantity to be investigated. As has been stated before, the ground state configuration gives a value for the so-called winding number, ω, the average distance between monomers in the ground state. Since the effect of applying an external tensile force F at both ends of the chain is to increase the natural bond length of the chain, the dependence of ω on l_0 was the quantity to be investigated.

As has been highlighted by other authors, two distinct cases can be identified: either the polymer is incommensurate with the underlying lattice, or it is commensurate with the lattice [96]. The polymer is said to be *commensurate* with the lattice if and only if there are integers m and n such that $m\omega = n\lambda$, where λ is the wavelength of the potential. This means that m monomers are to be found for every n complete cycles of the potential, with the pattern repeating periodically. If the polymer is not commensurate, it is said to be *incommensurate*. For the case of incommensurate distribution, it has been shown that the ground state value for ω can be infinitesimally shifted by a gradual increase of the bond length l_0. This means that despite small rearrangements of the particles, the average particle distance increases linearly with the length l_0 and should reflect the intrinsic stiffness of the atomic chain. In the commensurate case, on the other hand, the particles are

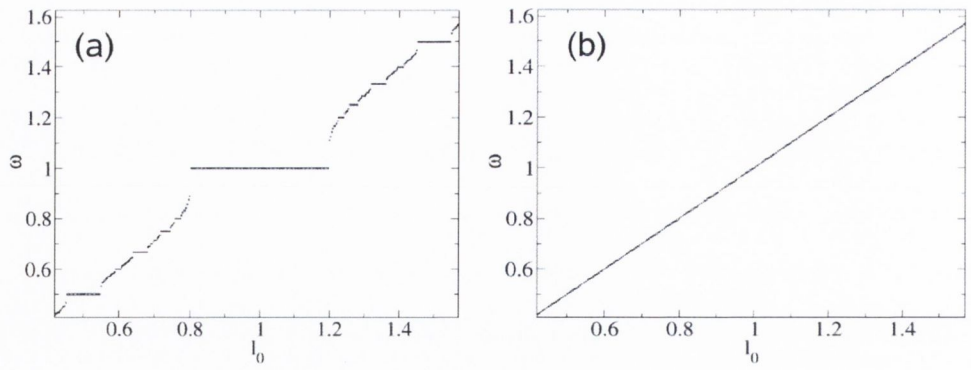

Figure 5.2: A plot of two limiting cases of the $\omega(l_0)$ diagrams for a sinusoidal potential. (a) Plots the case of extremely deep minima (U/k = 1). In this case the diagram is composed of a series of large plateaus, and the system should not respond well to stress. (b) Plots the case of vanishing potential corrugation. No plateaus are observed, and the chain is free to move in response to a stress.

trapped by the minima of the external potential. In this way, there is a range of values of l_0 for which the average separation ω does not change. This corresponds to the case in which the chain follows the same periodicity as the external potential and will be referred to as being templated by the potential.

There are a few special cases that are worthy of investigation – in the limit of very stiff springs (or shallow potentials, which amounts to the same thing), it has been found that the percentage of the graph which is taken up by plateaus tends to zero. On the other hand, for deep minima, it is found that the graph becomes almost completely step-like. I have utilised my program to investigate these limits and found results in agreement with [96], among others, and gives confidence that the implementation of the algorithm used is accurate. The resulting graphs for these limiting cases are displayed in Fig. 5.2.

If l_0 has a value such that for small Δl_0, $\omega(l_0 + \Delta l_0) = \omega(l_0 - \Delta l_0) = \omega(l_0)$ i.e. $\omega(l_0)$ is in a plateau, then the application of an external tensile force (which acts to change l_0) is unable to change the *average* inter-monomer distance. It is thus not possible to probe the Young's modulus of the polymer, and rather it is the Young's modulus of the host substrate which is probed (which is modeled by the

rigid potential).

This can be seen in Fig. 5.3 where the average equilibrium inter-particle distance ω of an atomic chain is plotted as a function of the bond length l_0 for the sinusoidal potential depicted in the inset. Plateaus in the l_0 curve corresponding to the commensurate regime are surrounded by linearly varying regions that characterise the incommensurate case. Also known as (an incomplete) Devil's staircase [97], this diagram provides information about the templating capacity of the potential. Bearing in mind that the chain ultimately represents a polymer strand and that the potential is the result of the interaction with the nanotube lattice, in the templated regime the strand displays not its intrinsic elastic response but that associated with the underlying nanotube. In other words, the plateaus of the Devil's staircase represent the situation in which the polymers experience the significantly superior stiffness of the nanotube. Therefore, by identifying the conditions for the appearance of the plateaus in the corresponding Devil's staircase, one can in principle control the reinforcement levels in a composite material. Although this argument was based on results for 1-dimensional chains in the presence of sinusoidal potentials, it can be easily extended to the case of polymer strands adsorbed onto the walls of a nanotube.

In the case of polymer strands coiling around the nanotube walls, it is convenient to visualise the polymer strands on top of the unwrapped nanotubes, as seen in Fig. 5.1b. Rather than simple sinusoidal potentials, the interaction with the hexagonally symmetric nanotube atoms generates periodic potentials with more than one Fourier component, which will be described in the next section.

5.2.5 Details of interaction potential

In the case of a polymer interacting with a carbon nanotube, it is assumed that the interaction is via the van der Waals force only. This is justified by the fact that carbon nanotubes are known to be very chemically inert, and do not readily form covalent bonds with other species. It is worth stressing that no account is

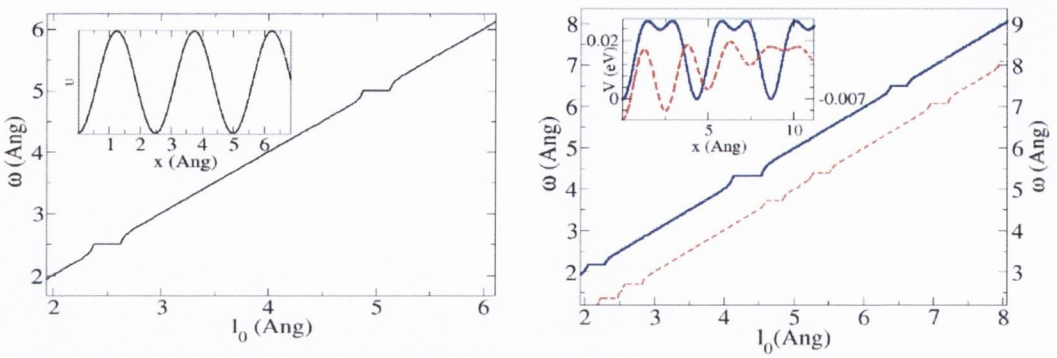

Figure 5.3: Average particle separation ω as a function of the natural bond length l_0 displaying a typical Devil's staircase found in the Frenkel-Kontorova model. Both quantities are expressed in Angstroms. The commensurate phases represented by the plateaus are surrounded by linearly varying sections characterising the incommensurate ones. This is seen to be a case intermediate to those found in Figs. 5.2a and 5.2b. The inset depicts the sinusoidal potential in equivalent units to those used in generating the staircase. (b)Similar Devil's staircases obtained for strands coiling around a $(5,0)$ zigzag nanotube (lattice parameter $a = 2.45$Å) at different coiling angles ($\theta = 0°$ for the continuous blue line and $\theta = 74°$ for the dashed red line). The inset shows the corresponding potentials. Continuous (dashed) lines are read on the left (right) vertical axis.

taken of a possible polarisation interaction, an assumption that would fail if the bound polymer is charged. Under the assumption that it is the carbon backbone of the polymer strand which interacts with the nanotube, a carbon-carbon potential that has the requisite amplitude for the interaction (about 30 meV, according to [98]), as well as the requisite hexagonal symmetry, can be derived by using the first few Fourier components of the Lennard-Jones 6-12 potential for carbon binding to graphite. The detailed form of such a potential can be calculated by introducing appropriate Lennard-Jones parameters and summing over the contributions due to each pair. In principle, there is nothing to stop such a calculation, but this is not the approach that we took.

Irrespective of the fine details of the potential, we do know about its spatial symmetries. The potential that would be felt by one monomer interacting with an ideal graphene sheet must have the same symmetry as the hexagonal array of atoms.

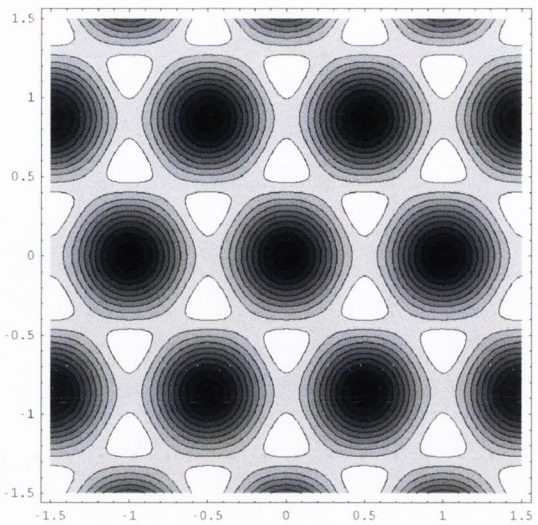

Figure 5.4: Contour plot of the potential as per Eq. (5.6). Darker regions correspond to the regions where the potential well is deep, while lighter regions are where it is shallow.

We assume that the atoms are most strongly bound when they are directly above the centre of a hexagon (in the same position as a type II impurity, as described previously in chapter 3 of this thesis). In terms of the usual Cartesian coordinates, a suitable potential which satisfies this description is given by:

$$V(x,y) = V_0 \left\{ 3 - \cos\left[\frac{2\pi}{a}\left(\frac{x}{\sqrt{3}} + y\right)\right] - \cos\left[\frac{2\pi}{a}\left(\frac{-x}{\sqrt{3}} + y\right)\right] - \cos\left[\frac{4\pi x}{\sqrt{3}a}\right] \right\}. \tag{5.6}$$

This potential has the correct corrugation, and takes values in the range $[0, 4.5V_0]$. Assuming that V_0 is positive, we see that the potential minima lie at the points $m\vec{a}_1 + n\vec{a}_2$ where $m, n \in \mathbb{Z}$, $a_1 = (a, 0)$ and $a_2 = (\frac{a}{2}, \frac{\sqrt{3}a}{2})$.

Since experimental evidence indicates that the polymer strand coils at a definite coiling angle, we fix the angle θ. To do this, we assume that the strand passes over two distinct minima of the potential, $(0, 0)$ and $m\vec{a}_1 + n\vec{a}_2$. This engenders a one dimensional periodic potential, $U_\theta(x)$, where θ is given by simple geometry as

$$\tan(\theta) = \frac{\sqrt{3}n/2 + m}{n/2} = \frac{\sqrt{3}n + 2m}{n} \tag{5.7}$$

We then solve for the ground state configuration of the polymer strand embedded

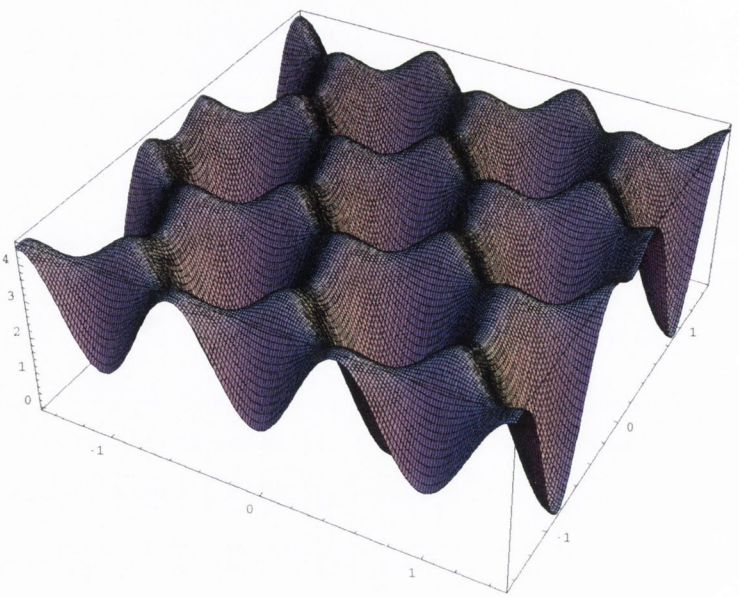

Figure 5.5: 3D plot of the potential as per Eq. (5.6). The preferential binding sites are seen to correspond to the centre of the hexagons.

in this one dimensional potential, giving the winding number ω. To calculate the fraction of cases for which templating occurs, hereafter referred to as the *templating fraction* and denoted by T_f, we perform the calculation for a large number of distinct pairs (n, m), chosen such that the resulting set of $\theta(m, n)$ is uniformly distributed between 0 and $\frac{\pi}{2}$ radians. In fact, a non-uniform angular distribution can be introduced by the simple expedient of an angle dependent weighting factor.

While this analysis suffices for the case of polymer strand interacting with a uniform graphene sheet, a similar analysis is possible in the case of nanotubes, albeit with a subtlety. In this case, we embed the potential onto a cylinder of radius appropriate to the chiral indices of the tubes. The chirality of the nanotube can be taken into account by rotating the potential. We then project this rotated potential onto a second concentric cylinder of radius $r + dr$, where dr is the van der Waals radius, assumed to be 3.45Å throughout. In practice, the only effect this has on the calculation is a stretching of distances in the radial direction.

5.2.6 Results and discussion

As a result of the symmetry of the hexagonal potential, the effective potential experienced by the polymer strands has more local minima within a given period than a simple sinusoidal potential, which by construction has only one local minimum per period. Such a higher density of local minima is likely to enhance the density of commensurate phases and consequently the templating capacity of the potential (provided the local minima are sufficiently deep). Such suspicions are confirmed by Fig. 5.3b, which shows two distinct calculated Devil's staircases associated with their respective potentials (shown in the inset). Such potentials correspond to different slices of the previously discussed potential.

Both the staircases and the potentials have been displaced along the vertical axis for the sake of distinction but each individual curve corresponds to a different coiling angle. Since the appearance of plateaus indicate that strands are being templated by the underlying periodic potential, it is useful to calculate the frequency with which these plateaus appear for a given type of nanotube. By averaging over all possible coiling angles for a fixed natural bond length, we define a templating fraction T_f that gives the fraction of polymer strands experiencing the stiffness of the nanotube. In this way, rather than assuming that all polymer strands surrounding the nanotube display perfect stress transfer, as implied by the standard rule-of-mixtures, we can quantify the fraction of cases for which this optimal transfer takes place.

To calculate the mechanical reinforcement of the composite material one has to consider not only the Young's modulus of the hybrid cylinder made of a nanotube coated by a crystalline layer of polymer, but also the fact that this hybrid structure is embedded in a matrix of amorphous polymer. For the purposes of the present work, it is sufficient to focus on the reinforcement of the hybrid structure, thus disregarding the effect of the surrounding matrix. Certainly, any reinforcement produced in the hybrid will lead to an enhancement in the mechanical response of the entire composite material. The Young's modulus Y_h associated with the hybrid

structure can then be expressed as

$$Y_h = V_f Y_{NT} T_f + (1 - V_f) Y_p, \tag{5.8}$$

where Y_{NT} and Y_p are the Young's modulus of the nanotube and the polymer, respectively, and V_f is the fractional volume taken by the nanotube. It is worth mentioning that the only difference to the usual rule-of-mixtures expression for the Young's modulus of composite structures is in the introduction of the templating fraction T_f in the first term on the right-hand side of the equation. This always serves to *reduce* the calculated Young's modulus, and as such reflects the imperfect stress transfer.

One immediate consequence of this expression is that the Young's modulus of the hybrid structure scales linearly with the volume fraction of nanotubes, a feature that is also observed in measurements of the elastic moduli of polymer-nanotube composite structures. It is evident from the expression above that the larger the templating fraction, the larger the Young's modulus of the hybrid structure, which means that a reliable way of calculating the templating fraction is important to provide a good estimate for the mechanical reinforcement induced by the nanotubes.

For a given polymer with a well-defined bond length l_0, the obvious way of calculating T_f consists of selecting a large number of coiling angles. Inside this formalism, a value for T_f can be derived by fixing a value of l_0 (which in effect fixes the polymer), and obtain the ground state configuration for each individual angle and count the fraction of cases for which the polymer lies inside a templating plateaux for a large range of coiling angles (assuming implicitly that each angle is as probable as any other).

This counting-by-inspection procedure is slow and computationally intensive since reliable results for T_f requires a large number of angles. Furthermore, the graph so obtained is quite noisy, but displays definite trends. The results of such a

calculation are displayed in Fig. 5.6a. In particular, there are a number of readily observable peaks that stand out.

5.2.7 Graphical method for the templating fraction

It is clear from Fig. 5.3b that the occurrence of plateaus in the staircases correlates with the existence of a high concentration of local minima, which suggests that there might be a way of obtaining the templating fraction by associating it with the distribution of those minima. In fact, analysis of a few Devil's Staircase graphs yielded a geometric interpretation that simplifies the counting procedure. It consists of projecting the hexagonal lattice of the nanotube of radius r onto a cylinder of radius $r + dr$. Simple geometry shows that while distances in the axial direction are unchanged, projected distances in the circumferential direction are scaled by a factor $1 + \frac{dr}{r}$.

I must emphasise that the plateaus do not occur randomly; rather they are correlated with the positions of the potential minima of this 1D section of the projected lattice. More precisely, the plateaus appear every time a polymer atom lies in the proximity of a potential minimum, that is, in the proximity of an edge of the projected lattice. How close the polymer atoms must be to the local minima depends on the size of the corresponding templating plateau. Therefore, by superimposing the polymer strands (at a given bond length l_0) onto the projected hexagonal lattice one can graphically check whether or not the former is templated by the latter, a much simpler procedure than the counting-by-inspection method. This suggest that for a given angle we can construct a pseudo-staircase, which approximates the real one. Such staircases will have plateaus at those values of l_0 that correspond to local minima for that angle.

Despite the tremendous simplification, the agreement between the two counting methods is remarkable, as shown in Fig. 5.6a, where the templating fraction calculated by both methods is plotted as a function of the bond length l_0. Except

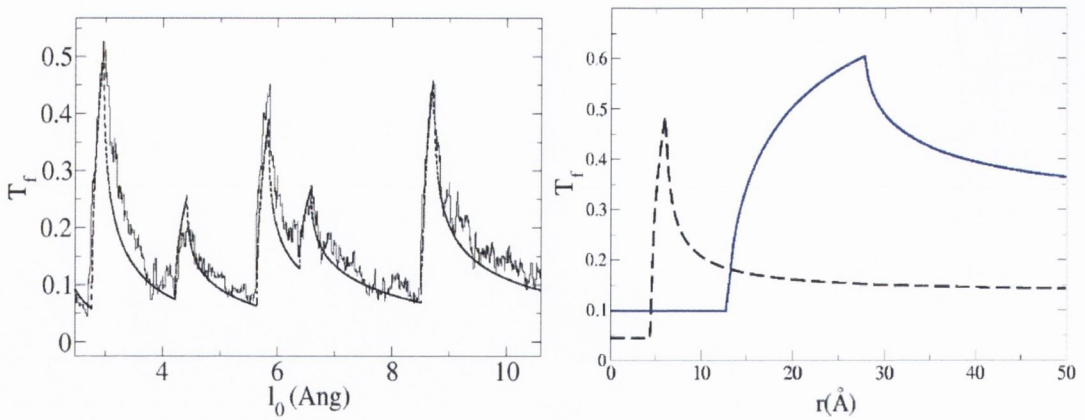

Figure 5.6: (a) Templating fraction T_f as a function of the bond length l_0 (in Å). The full line displays T_f calculated by averaging over a large number of possible coiling angles and counting the fraction of cases in which a given value of l_0 lies inside a plateaux. The dashed line is obtained by the graphical method (see text). Despite small fluctuations, the agreement is evident. (b) Templating fraction as a function of nanotube radius (zigzag) for two different values of $l_0 = 2.45$Å for the full line and $l_0 = 3.0$Å for the dashed lined. The elastic constant was chosen to be $k = 21$ eV/Å^2, in accordance with estimated values for poly-vinyl alcohol.

for small fluctuations, the full line representing the counting-by-inspection method agrees with the graphical method represented by the dashed line. The figure shows that the templating fraction reaches periodical maximum values, which indicates that the right choice of polymer parameters might lead to increased levels of reinforcement. Unfortunately, such set of parameters cannot be varied in a continuous fashion due to the limited number of polymer types.

5.2.8 Diameter dependence of the reinforcement

A more controllable quantity that can be continuously varied is the nanotube diameter. By plotting the templating fraction (obtained by the graphical method) as a function of the nanotube radius, we show in Fig. 5.6b that T_f also behaves non-monotonically. Maximum values of the templating fraction at certain diameters predict that an adequate selection of diameters is capable of optimising the level of mechanical reinforcement in polymer-nanotube composites. Different types of polymers lead to distinct optimal diameters indicating that it is possible to select a right

combination of materials to maximally enhance the mechanical properties of these composites.

It should perhaps be noted in passing, that while it is not possible to continuously vary the radius of zig-zag nanotube, that the difference between the radii of zig-zag tubes of adjacent radii is $\frac{a}{2\pi}$, where a is the lattice constant of a nanotube: 2.45Å. This means that the radius can be varied in steps as small as 0.4 Å, thus justifying the treatment of the variable r as continuous. Realistic parameters $k = 21\text{eV/Å}^2$ and corrugation 30 meV were used, and the results are displayed in Fig. 5.6b.

Finally, we can test our model by comparing the estimated value of Y_c with experimental data available in the literature. It is important to stress that we have chosen a system with a thin crystalline phase. Thicker crystalline coatings are expected to affect the degree of reinforcement but would require an extension of the present model to include the volumetric contribution of this phase. Fig. 5.7 shows the measured Young's modulus of nanotube/poly-vinyl alcohol (PVA) composites as a function of the volume fraction, V_f, of inserted nanotubes. Arc discharge multiwalled nanotubes (diameter 24 nm) were blended with poly-vinyl alcohol with volume fraction V_f ranging from 0% to 0.16%. The full line is the standard rule of mixtures expression and clearly overestimates the observed levels of reinforcement represented by the points. The dashed line representing our results with the calculated templating fraction $T_f = 0.2$ for a nanotube of corresponding diameter obtained from Fig. 5.6b displays significant improvement in the comparison with the measured values. The disagreement between our results and the observed values may be explained by the fact that a small but finite thickness for the intrinsically tougher crystalline phase enhances the reinforcement of the system.

5.2.9 The effect of crystallinity

Of course, increasing thicknesses of crystalline polymer will increase the strength of the composite, if for no other reason than the higher Young's modulus of the

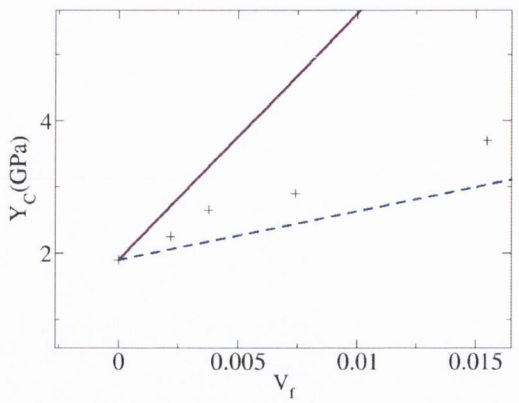

Figure 5.7: Young's modulus of nanotube-polymer composites for small loadings of nanotubes. Prediction based on the rule of mixtures (assuming perfect stress transfer) is given by the continuous (purple) line. The experimental results are marked by the crosses, while our prediction based on $T_f = 0.2$ (see the text) is given by the dashed (blue) line.

crystalline phase, as compared to the amorphous phase. Recent investigations [99], sparked by our prediction of a non-monotonic diameter dependence of reinforcement, into polyvinal-alcohol carbon nanotube composites have, however, suggested that the crystallinity may in fact play a more direct role in the increase in Young's modulus than our model allows. In this case, a stiffer and stronger region of ordered polymer is formed in a roughly cylindrical shell about the tube, of non-negligible thickness. Their conclusions point to this stiffer shell being the primary mechanism for reinforcement, and conclude that the interfacial stress transfer does not play a significant role. If this is the case, this puts a limit on the utility of the method that we have developed. While our method should be of quantitative use in the case of a monolayer of ordered coating about the nanotube, the formation of a third phase of significant thickness would require that we take this directly into account. It is worth noting that one finding of this work is that of an apparent Young's modulus of the nanotube of 71GPa, albeit with a large margin of error. This is substantially lower than quoted values for the Young's modulus of arc discharge grown nanotubes, for example. They conclude that there is poor load transfer from the ordered matrix to the nanotube. Our model accounts for poor load transfer between the phases.

5.3 Summary and conclusions

In summary, we have presented a model describing how the interaction of crystalline polymers surrounding the carbon nanotubes may affect the mechanical properties of nanotube-polymer composites. Rather than assuming full stress transfer between the different phases of the composite, the model suggests that only a fraction of the polymer layers are templated to the underlying nanotube lattice. This fraction of templated polymers experiences the significantly larger stiffness of the nanotube and is responsible for the enhancement of the mechanical response of the composite. Furthermore, the model predicts that by tuning the nanotube diameter one can optimise the templating fraction for each type of polymeric material, thus maximally enhancing the mechanical properties of the composite. In other words, we suggest that an appropriate set of polymers and nanotubes diameters can be combined to maximise the mechanical response of the structure.

Chapter 6

Conclusions

6.1 Summary of work undertaken

In this thesis, I have presented the work undertaken over the course of the last four years. The primary focus of my research has been in studying doped carbon nanotube structures through the use of simple models, with the aim of shedding light on the properties that composed structures have been shown to possess. The motivation for this research is that if we wish to utilise the remarkable properties of nanotubes through their interaction with foreign objects, we should be able to predict and understand the properties of so-formed hybrid structures. In this work I have investigated theoretically the physical properties of a wide range of technologically interesting composite systems, including carbon atoms bound both covalently and non-covalently to simple adatoms and adsorbed small molecules, as well as polymer strands adsorbed on the surface of a nanotube.

6.1.1 Overview of chapter one

In the first chapter, I have presented a introduction to the field of nanotubes. I highlighted their superlative intrinsic physical properties of these nanoscopic molecules, both predicted and found experimentally, and discussed possible routes to best utilise

them in useful materials. I also outlined the desirability of a scheme to model the interaction between carbon nanotubes and foreign objects, and summaries some features that such a formalism which is capable of predicting and explaining the properties of hybrid nanotube based structures should possess.

6.1.2 Overview of chapter two

In chapter 2, I have presented the details of such a formalism. Based on Green function methods, and utilising the well-known Lloyd sum rule, the method was introduced in its general form. I have shown how we have specialised the scheme to deal with the case of contact potentials, appropriate to modeling the interaction that occurs when a foreign body is introduced into the vicinity of a host. This method is predicated on the fact that the electronic structure of the isolated components is well known; in the case of carbon nanotubes that happens to be the case. The pedagogical case of a linear chain which is perturbed by a simple atomic level was presented to illustrate what I have referred to as the Lloyd formula method (LFM), and an analytical treatment was performed to investigate imposed constraints on the matrix elements of the tight-binding perturbation.

6.1.3 Overview of chapter three

In chapter 3, we have considered doped metallic nanotubes by utilising the LFM. This chapter was essentially divided into two parts. In both sections, we modeled the electronic structure of single walled carbon by using the zone folded tight-binding approach. In the first section, we considered the special case of externally adsorbed hydrogen atoms in contact with the surface of the nanotube. By modeling the interaction between the nanotube and the perturbing hydrogen atom through a contact potential similar to that introduced in chapter 3, we were able to show that it is possible to extract information about the underlying tight-binding parameters that characterise the coupling, when given knowledge of a few properties of the combined

system. To this end, we utilised a density functional theory code to calculate values for the charge transfer between the parts, ΔC and the electronic contribution to the binding energy, ΔE. With this knowledge, we showed how it was possible to solve the set of non-linear equations, which give these quantities in terms of the Green functions of the isolated parts of the system, for the matrix elements of the perturbation Hamiltonian. We showed a good agreement between the band structures generated with these parameters and the Kohn Sham band structure, which comes from the more sophisticated density functional calculation. The agreement was seen to improve as we relaxed the assumption of perfect screening, and considered a screening cloud of finite radius.

In the second part of chapter three, we utilised the same Green function methods to investigate a range of adsorbed impurities, again through the use of a simple contact potential. In this section, we showed that it is possible to find correlations between ΔE and ΔC. Given knowledge of either of these, this correlation allows us to extract information about the possible range of values that the other has, even when no details are known about the contact potential. We showed how it is possible to investigate a wide range of impurities, with the aim of finding the ideal combination of nanotube / dopant pair to maximise changes in the physical properties of the system, something which is especially desirable if we are to utilise nanotubes as molecular sensors. When compared to *ab-initio calculations*, good agreement was found.

The work presented in this chapter been published in [74], [73], and [72].

6.1.4 Overview of chapter four

The fourth chapter of this thesis focused on trying to understand some aspects of the reported helical coiling observed for some polymeric molecules bound to the surface of nanotubes. Again, the chapter was composed of two sections. In the first section, we asked if it was possible that spontaneous helical order could arise in a simple

model for the polymer / nanotube interaction. Here, we treated the nanotube by considering a two dimensional free electron gas confined to the surface of a nanoscale cylinder. The interaction with the cylinder was modeled by the inclusion of a highly localised perturbing potential, which was allowed to coil around the tube at a constant angle. By drawing an analogy with the Kronig-Penney model, we were able to utilise the LFM equations for the change in the binding energy to suggest that there were certain spacings between adjacent images of the perturbing potential that extremised the change in the total energy of the system. Since different coiling angles correspond exactly to different spacings between adjacent images, we were able to show a non-monotonic dependence of the binding energy on the coiling angle. This may give a hint that a wrapping polymer need not restrict itself to following the inherent chirality of the nanotube that it wraps around.

To this end, we considered a somewhat more sophisticated model for the nanotube / polymer binding, where we again treat the nanotube within the tight-binding model. Since we do not have the precise details of the makeup of the polymer strand, and bearing in mind the possibility of placing charge on the wrapping molecule, we chose instead to consider the effect that a charged one dimensional stripe wrapping around the nanotube has.

In order to clarify the effects that the different properties of the perturbing molecule can have on the electronic structure of the nanotube, we calculated the dependence of a number of quantities of physical interest on three different parameters that characterise the potential: the width, the coiling angle and the amplitude of the potential. Quantities investigated included the size of the perturbation-induced mini-gaps, the electronic contribution to the binding energy, and the position of the van Hove singularities. To do this, we modeled the effect that the polymer had on the electronic structure of the nanotube via a polarisation potential, which corresponds to the weak coupling limit of the LFM. As in the first section of the chapter, we saw a non-monotonic dependence of the total energy of the system on the coiling

angle; however, in this case, we saw that the most dramatic changes in the binding energy did indeed correspond to the high symmetry directions of the nanotube.

The work in this chapter has been published in [85] and [84].

6.1.5 Overview of chapter five

This chapter again dealt with understanding the interaction between polymer strands and a nanotube that they wrap around. The tenor of this chapter is somewhat different to what went before, however; whereas in previous chapters we focused on using quantum mechanical models to understand changes induced by doping in the electronic structure of the nanotube, here we used an extension of the classical Frenkel-Kontorova model to investigate the mechanical properties of wrapped nanotubes. In this chapter, we modeled a polymer strand wrapping about a nanotube via a ball and spring chain embedded in an external hexagonal potential. We argued that the effect of imperfect stress transfer across a nanotube / polymer-matrix interface suppresses the ability of the nanotubes to mechanically reinforce a composite containing a small amount of nanotubes. In this work, we have identified the occurrence of efficient stress transfer across the interface with a templating of the polymer onto the walls of the nanotube. Comparison with experiment showed that a uniform angular distribution leads to a prediction for reinforcement quite similar to that observed. Our model was also found to predict a non-monotonic dependence of the reinforcement on the average nanotube radius. Investigations of this prediction have incidentally further clarified the role that nanotubes play in nucleating a thick crystalline coating, which seems to act as the primary agent of reinforcement in poly-vinyl alcohol / nanotube composites [99].

The work presented in this chapter has been published in [90].

6.2 Possible extensions of this work

Throughout this work, I have consistently utilised simple models to try to understand the properties of nanotubes which interact with foreign objects. The general formalism to treat doped nanotubes presented in chapters two and three was utilised within the zone-folded approach for the electronic structure of the nanotube. While this allows us to use existing formulae for the Green functions of the nanotube, it comes at the price that we do not take curvature into account. There is, in principle, no need to restrict ourselves to this approach. A tight-binding method based on a non-isotropic hopping integral will be able to reproduce the curvature induced mini-gaps in those tubes which are over-metallised by the zone folding approach. It is also well known that the use of a non-orthogonal basis set is needed to account for that portion of the band structure of a nanotube which lies above the Fermi level. While this was not of concern to us, since we have looked at ground state properties, this is another area where the general model can be extended.

Perhaps the most important extension of the formalism over its presentation here is to include multiple orbitals per atom. Such an approach will necessitate more complicated coupling matrices, involving more parameters to be determined. This will require the introduction of more Lloyd formula relations; suitable candidates are local density of states relations between the tight-binding parameters and the change in the integrated local density of states. Similar correlations between the binding energy and the energy transfer to the adsorbate are expected in this case.

As regards the work performed in chapter five, this model has already been extended to model a polymeric monolayer at the surface of the nanotube. A similar approach, based on an investigation of a two dimensional ball-and-string lattice arranged as a monolayer around a nanotube, and carried out within our group by Kenneth Treacy as a summer project, displayed similar features to the one dimensional model presented in chapter five. Again, we were able to see that sections of the net favoured to go into registry with the underlying potential, in a similar

fashion to the argument presented in this work.

As far as the work on coiling polymers is concerned, one of the obvious weaknesses is that we have left the parameters that characterise the potential as free variables. It may be useful to try to study a simple polymer. In the same vein, while we used a square well potential to model the polarisation interaction, there is no need to restrict ourselves to this shape. It seems reasonable to suppose that the introduction of a distribution function for λ (the amplitude of the perturbing potential) as both a function of the width, and of the distance traversed along the polymer strand may be necessary to model the various one dimensional charge distributions that occur in nature.

Appendix A

Green Functions

The time independent properties of an isolated electronic system are most familiarly described in terms of the time-independent Schrodinger equation

$$\hat{H}|\psi\rangle = E_\psi|\psi\rangle, \tag{A.1}$$

where $\hat{H}$ is a linear operator called the Hamiltonian, $|\psi\rangle$ describes the quantum eigenstate of the system, and E_ψ is the energy of the system when it is in the eigenstate $|\psi\rangle$. The so-called electronic structure of the system then corresponds to a knowledge of these allowed energies.

In the independent electron model, which will be assumed throughout this work, it is assumed that electrons in a solid interact only with the ionic lattice, and not with one another. In this fashion, we are able to write the Hamiltonian of the system as a product of Hamiltonians for single electrons. For an isolated molecule inside the independent electron approximation, the electronic structure of the molecule corresponds to a sequence of bound state energies $E_0, E_1, E_2, \cdots$, ordered from the lowest to the highest. In the absence of magnetic interactions, there is a spin degeneracy of 2, since each state can be occupied by two electrons with different values of the magnetic spin quantum number, without violating the Pauli principle. Furthermore, there may exist further symmetries of the molecule that mean that some

of the energy levels are equal.

For an extended system which is periodic, Bloch's theorem tells us that we can write the Hamiltonian of the total system as the sum of Hamiltonians of electrons with definite crystal momentum k. While the energy levels of an atom generally fall into a sets of points, in a solid the allowed energies fall into bands. For example, there may be allowed states in the range (E_0, E_1), none in the range (E_1, E_2) and some more in the range (E_2, E_3). For a truly infinite system (a mathematical idealisation that nonetheless is an excellent approximation for solids with at least one macroscopic dimension due to the sheer size of Avogadro's number), the usual way of characterising the electronic structure of the system is through the use of the so-called density of states. The density of (single-electron) states is formally defined as the number of states that lie in the range $[E, E + \delta E)$ in the limit that $\delta E \to 0$, normalised to the size of the interval.

Lloyd's formula utilises information about the isolated subsystems not by directly considering their individual Hamiltonians, but rather through using the corresponding single particle Green function (in this work, the phrases "Green function" and "single particle Green function" will be used interchangeably, as we will not consider any many-body Green functions). Roughly speaking, the Green function (which will here almost exclusively be denoted by some variant of the letter g) gives an idea about the causal connection between two states *at a given energy*, E. If $\hat{g}(E)$ is the Green function of the Hamiltonian corresponding to the system O, then $\hat{g}(E)|o_i\rangle = \sum_j c_j(E)|o_j\rangle$ for some complex functions $c_j(E)$, and $\langle o_i| \hat{g}(E) |o_j\rangle$ will be a complex function of energy E (in principle non-zero). On the other hand, under the assumption that the state $|a_j\rangle$ is orthogonal to all the $|o_i\rangle$ and that $\hat{G}$ is the combined Green function of the *isolated* subsystems then $\langle a_j| \hat{G} |o_i\rangle = \langle o_i| \hat{G} |a_j\rangle = 0$, for all j: the Green function matrix element between initially disconnected parts of the system vanishes.

It is apparent from the definition that matrix elements of the Green function

carries dimensionality of inverse energy. A series of remarks are worth making at this point. First off concerns the utility of the Green function approach. As far as we are concerned, the most useful property that the Green function has is the fact that it is intimately related to the partial density of states for electrons on orbital $|\phi\rangle$ by the relation

$$\rho_\phi(E) = \frac{-1}{\pi}\mathrm{Im}\left(\langle\phi|\,\hat{g}\,|\phi\rangle\right) \tag{A.2}$$

Since the total density of states is just got by summing over all orbitals ϕ

$$\rho(E) = \sum_\phi \frac{-1}{\pi}\mathrm{Im}\left(\langle\phi|\,\hat{g}\,|\phi\rangle\right) = \frac{-1}{\pi}\mathrm{Tr}\left(\mathrm{Im}\left(\hat{g}(E)\right)\right). \tag{A.3}$$

In this fashion, with the knowledge of the Green function, we can plot the density of states, and make inferences about the physical properties of the corresponding material. The limit can be attained by evaluating $g(E)$ for successively smaller values of η. This approach breaks down if there is a divergence in the density of states. The density of states should be viewed as a distribution function; like Dirac's delta function it should appear as a factor in an integrand, the integral of which is finite. Even so, it is worth pointing out that for non-zero *eta*, a Lorentzian broadening allows us to work with a sufficiently close approximation to the true density of states (or more often in this work, the *change* in density of states), which does not diverge (or diverges only in proportion to the system size).

Secondly, if the Hamiltonian is of a particularly simple form, $\hat{H} = \epsilon|\epsilon\rangle\langle\epsilon|$ then

$$\begin{aligned}\hat{g}(E) &= \lim_{\eta\to 0^+}\left(|\epsilon\rangle\langle\epsilon|(E+i\eta) - \epsilon|\epsilon\rangle\langle\epsilon|\right)^{-1} \\ &= \lim_{\eta\to 0^+}\frac{|\epsilon\rangle\langle\epsilon|}{E+i\eta-\epsilon}.\end{aligned} \tag{A.4}$$

Such a Hamiltonian will be met when I consider the electronic structure of an adsorbed atom, where the interpretation of α will be that of the ionisation potential of the atom.

A final point is that even if the Hamiltonian is more complicated than that of the simple atom, if we can still find its eigenbasis $|k,\beta\rangle$ (where we are foreshadowing the use Bloch theorem to use k as a quantum number that partially diagonalises the Hamiltonian), then we can again write

$$\begin{aligned}
\hat{g}(E) &= \lim_{\eta\to 0^+} (\hat{1}(E+i\eta) - \hat{H})^{-1} \\
&= \lim_{\eta\to 0^+} (\sum_{k,\beta} |\epsilon_{k,\beta}\rangle\langle\epsilon_{k,\beta}|(E+i\eta) - \sum_{k,\beta} \epsilon_{k,\beta}|\epsilon_{k,\beta}\rangle\langle\epsilon_{k,\beta}|)^{-1} \\
&= \sum_{k,\beta} \lim_{\eta\to 0^+} \frac{|\epsilon_{k,\beta}\rangle\langle\epsilon_{k,\beta}|}{E+i\eta-\epsilon_{k,\beta}}. \qquad \text{(A.5)}
\end{aligned}$$

Appendix B

Derivation of Lloyd's formula

To derive Lloyd's formula we assume that the system is initially described by a Green function $\hat{g}$, the coupling Hamiltonian is $\hat{V}$ and the coupled Green function is denoted by $\hat{G}$. We assume that Dyson's equation holds:

$$\begin{aligned} \hat{G} &= \hat{g} + \hat{g}\hat{V}\hat{G} \\ \Rightarrow \hat{G} - \hat{g}\hat{V}\hat{G} &= \hat{g} \\ \Rightarrow (\hat{1} - \hat{g}\hat{V})\hat{G} &= \hat{g} \\ \Rightarrow \hat{G} &= (\hat{1} - \hat{g}\hat{V})^{-1}\hat{g} \end{aligned} \tag{B.1}$$

Dyson's equation can then be formally solved to yield

$$\hat{G} = \hat{g} + \hat{g}\hat{V}(\hat{1} - \hat{g}\hat{V})^{-1}\hat{g} \tag{B.2}$$

where the operator $\hat{V}(\hat{1} - \hat{g}\hat{V})^{-1}$ is commonly called the *T-matrix* and denoted $\hat{T}$. Even if $\hat{V}$ is independent of energy, $\hat{T}$ is, in general, not. The change in the density of states is then given as $\Delta\rho(E) = \frac{-1}{\pi}\mathrm{Im}\left(\mathrm{Tr}\left(\hat{G}(E) - \hat{g}(E)\right)\right)$, which is

$$\Delta\rho(E) = \frac{-1}{\pi}\mathrm{Im}\left(\mathrm{Tr}\left(\hat{g}\hat{T}\hat{g}\right)\right) \tag{B.3}$$

Which by the cyclic property of the Trace of the product of operators gives

$$\Delta\rho(E) = \frac{-1}{\pi}\mathrm{Im}\left(\mathrm{Tr}\left(\hat{T}\hat{g}^2\right)\right). \tag{B.4}$$

By the definition of the Green function,

$$\begin{aligned}\hat{g}^2 &= (E\hat{1} - \hat{H})^{-2} \\ &= -\frac{\mathrm{d}}{\mathrm{d}E}(E\hat{1} - \hat{H})^{-1} \\ &= -\frac{\mathrm{d}}{\mathrm{d}E}\hat{g}(E)\end{aligned} \tag{B.5}$$

which can be inserted into Eq. (B.4) to yield

$$\begin{aligned}\Delta\rho &= \frac{-1}{\pi}\mathrm{Im}\left(\mathrm{Tr}\left(-\hat{T}\frac{\mathrm{d}}{\mathrm{d}E}\hat{g}(E)\right)\right) \\ &= \frac{1}{\pi}\mathrm{Im}\left(\mathrm{Tr}\left((\hat{1} - \hat{g}\hat{V})^{-1}(\frac{\mathrm{d}\hat{g}}{\mathrm{d}E}V)\right)\right)\end{aligned} \tag{B.6}$$

However, since $\hat{V}$ is energy independent,

$$\frac{-1}{\pi}\mathrm{Tr}\left(\frac{\mathrm{d}}{\mathrm{d}E}\log\left(\hat{1} - \hat{g}\hat{V}\right)\right) = \frac{1}{\pi}\mathrm{Tr}\left((\hat{1} - \hat{g}\hat{V})^{-1}(\frac{\mathrm{d}g}{\mathrm{d}E}V)\right) \tag{B.7}$$

Comparing Eq. B.6 with the imaginary part of B.7 gives Lloyd's formula in its usual form

$$\Delta\rho = \frac{-1}{\pi}\mathrm{Im}\left(\mathrm{Tr}\left(\frac{\mathrm{d}}{\mathrm{d}E}\log\left(\hat{1} - \hat{g}\hat{V}\right)\right)\right). \tag{B.8}$$

Appendix C

Lloyd's formula for a localised perturbation

In this appendix, I aim to show how we can limit the evaluation of the determinant of the infinite-dimensional Lloyd matrix (introduced in Chapter 2), to a much smaller sub-matrix, in the case of a localised perturbation.

We write our localised basis set as $|i\rangle$. The determinant is invariant under choice of basis set, so we may as well work in this basis. We assume that the perturbation $\hat{V}$ all but the first n of the $|i\rangle$ lie in the kernel of $\hat{V}$ (this amounts to nothing more than a reordering of our basis). We take this as an effective definition of a localised perturbation. That is, we assume that

$$\hat{V}|i\rangle = 0, \qquad i > n \tag{C.1}$$

then

$$\langle j|\,\hat{V}\,|i\rangle = 0, \qquad i > n, j > n \tag{C.2}$$

and denote it as V_{ij} otherwise. It is not necessary to assume that any of the g_{ij} vanish. We must form the (in principle infinite dimensional) matrix $\sum_k g_{ik}V_{kj}$. However, due to the way that the determinant is constructed, it can be shown that the matrix

$\langle i|\hat{1} - \hat{g}(E)\hat{V}|j\rangle$ has the same determinant as the square sub-matrix consisting only of the first n rows and n columns. This is due to the sparse nature of the matrix of the perturbation potential.

To show this explicitly, consider the jth row of the matrix $\hat{g}(E)\hat{V}$, where $j > n$. The ith entry in this row is the number $\sum_k g_{ik}V_{kj}$. But since $j > n$, $V_{kj} = 0$ for all k, and so the matrix element is zero. So for all $j > n$, the jth column of the matrix of $\hat{g}(E)\hat{V}$ is a column of zeroes. This means that the only non-zero entry in the jth column of the matrix of $\hat{1} - \hat{g}(E)\hat{V}$ is the entry 1 in the jth row. In this fashion we show that the determinant of the total matrix is the same as that of the much smaller $n \times n$ matrix of the first n rows and columns.

To illustrate, consider the concrete example where we have only 4 states, of which only two are affected by the perturbation

$$\begin{pmatrix} g_{11} & g_{12} & g_{13} & g_{14} \\ g_{21} & g_{22} & g_{23} & g_{24} \\ g_{31} & g_{32} & g_{33} & g_{34} \\ g_{41} & g_{42} & g_{43} & g_{44} \end{pmatrix} \begin{pmatrix} V_{11} & V_{12} & 0 & 0 \\ V_{21} & V_{22} & 0 & 0 \\ 0 & 0 & 0 & 0 \\ 0 & 0 & 0 & 0 \end{pmatrix} = \begin{pmatrix} g_{11}V_{11} + g_{12}V_{21} & g_{11}V_{12} + g_{12}V_{22} & 0 & 0 \\ g_{21}V_{11} + g_{22}V_{21} & g_{21}V_{12} + g_{22}V_{22} & 0 & 0 \\ g_{31}V_{11} + g_{32}V_{21} & g_{31}V_{12} + g_{32}V_{22} & 0 & 0 \\ g_{41}V_{11} + g_{42}V_{21} & g_{41}V_{12} + g_{42}V_{22} & 0 & 0 \end{pmatrix}. \tag{C.3}$$

So that the determinant of the matrix $|i\rangle\hat{1} - \hat{g}(E)\hat{V}\langle j|$ is

$$\det = \begin{vmatrix} 1 - g_{11}V_{11} - g_{12}V_{21} & -g_{11}V_{12} - g_{12}V_{22} & 0 & 0 \\ -g_{21}V_{11} - g_{22}V_{21} & 1 - g_{21}V_{12} - g_{22}V_{22} & 0 & 0 \\ -g_{31}V_{11} - g_{32}V_{21} & -g_{31}V_{12} - g_{32}V_{22} & 1 & 0 \\ -g_{41}V_{11} - g_{42}V_{21} & -g_{41}V_{12} - g_{42}V_{22} & 0 & 1 \end{vmatrix} \tag{C.4}$$

Expanding in minors from the lower right hand corner, we see that the only choice from the third row is the third entry: all others require the selection of a zero entry

from the third column. So

$$\det = \begin{vmatrix} 1 - g_{11}V_{11} - g_{12}V_{21} & -g_{11}V_{12} - g_{12}V_{22} \\ -g_{21}V_{11} - g_{22}V_{21} & 1 - g_{21}V_{12} - g_{22}V_{22} \end{vmatrix} \tag{C.5}$$

This $n \times n$ determinant may then be evaluated either analytically, for example by expanding in minors, or by a numerically stable algorithm. From this point on, any reference to the matrix $\hat{1} - \hat{g}(E)\hat{V}$ will refer to this sub-matrix, which restricts our attention only to those sites which are involved in the perturbation.

Appendix D

Calculation of composite Green function for perturbed linear chain

Here we calculate the composite Green function for a linear chain perturbed by an adsorbed atomic impurity as required in Section 2.4.5. By definition,

$$\hat{G} = \Delta\hat{G} + \hat{g}$$

By Dyson,

$$\hat{G} = \hat{g} + \hat{g}\hat{V}\hat{G}$$

For a general matrix element,

$$G_{jj'} = g_{jj'} + \begin{pmatrix} g_{ja} & g_{j0} \end{pmatrix} \begin{pmatrix} \delta_a & \tau \\ \tau^* & \delta_0 \end{pmatrix} \begin{pmatrix} G_{aj'} \\ G_{0j} \end{pmatrix},$$

So that in particular (setting $j = a$),

$$\begin{pmatrix} G_{aj'} \\ G_{0j'} \end{pmatrix} = \begin{pmatrix} g_{aj'} \\ g_{0j'} \end{pmatrix} + \begin{pmatrix} g_{aa} & g_{a0} \\ g_{0a} & g_{00} \end{pmatrix} \begin{pmatrix} \delta_a & \tau \\ \tau^* & \delta_0 \end{pmatrix} \begin{pmatrix} G_{aj'} \\ G_{0j} \end{pmatrix}.$$

Rearranging gives

$$\left[\begin{pmatrix} 1 & 0 \\ 0 & 1 \end{pmatrix} - \begin{pmatrix} g_{aa} & 0 \\ 0 & g_{00} \end{pmatrix} \begin{pmatrix} \delta_a & \tau \\ \tau^* & \delta_0 \end{pmatrix}\right] \begin{pmatrix} G_{aj'} \\ G_{0j'} \end{pmatrix} = \begin{pmatrix} g_{aj'} \\ g_{0j'} \end{pmatrix}$$

or equivalently

$$\begin{pmatrix} G_{aj'} \\ G_{0j'} \end{pmatrix} = \left[\begin{pmatrix} 1 & 0 \\ 0 & 1 \end{pmatrix} - \begin{pmatrix} g_{aa}\delta_a & \tau g_{aa} \\ g_{00}\tau^* & g_{00}\delta_0 \end{pmatrix}\right]^{-1} \begin{pmatrix} g_{aj'} \\ g_{0j'} \end{pmatrix}.$$

So

$$\begin{pmatrix} G_{aj'} \\ G_{0j'} \end{pmatrix} = \begin{pmatrix} 1 - g_{aa}\delta_a & -\tau g_{aa} \\ -g_{00}\tau^* & 1 - g_{00}\delta_0 \end{pmatrix}^{-1} \begin{pmatrix} g_{aj'} \\ g_{0j'} \end{pmatrix}$$

Which by the elementary formula for the determinant of a 2×2 matrix gives

$$\begin{pmatrix} G_{aj'} \\ G_{0j'} \end{pmatrix} = \frac{1}{\det} \begin{pmatrix} 1 - g_{00}\delta_0 & \tau g_{aa} \\ g_{00}\tau^* & 1 - g_{aa}\delta_a \end{pmatrix} \begin{pmatrix} g_{aj'} \\ g_{0j'} \end{pmatrix},$$

where

$$\det = 1 - \delta_a g_{aa} - \delta_0 g_{00} - g_{aa} g_{00}(|\tau^2| - \delta_a \delta_0).$$

We are interested in the matrix element G_{aa} which, bearing in mind $g_{0a} = 0$, can be read off the top line of the above matrix equation (j'=a):

$$\begin{aligned} G_{aa} &= \frac{1}{\det} g_{aa}(1 - g_{00}\delta_0) \\ \Rightarrow \Delta G_{aa} &= \frac{1}{\det} g_{aa}(1 - g_{00}\delta_0) - g_{aa} \end{aligned} \tag{D.1}$$

We write the increase in number of particles on site a as ΔC (which is $\frac{-1}{e}$ times the increase in positive charge). Using the fact that the diagonal element $\langle a| \hat{G} |a\rangle$ of the total GF give the local density of states on orbital a, (as described in Chapter

One), we have

$$\Delta C = \frac{-1}{\pi} \int_{-\infty}^{E_F} \mathrm{d}E \ \mathrm{Im} \left(\frac{g_{aa}(1 - g_{00}\delta_{00})}{1 - g_{00}\delta_{00} - g_{aa}\delta_a + g_{00}g_{aa}(\delta_{00}\delta_a - |\tau|^2)} - g_{aa} \right) \qquad \text{(D.2)}$$

Appendix E

A comment on numerical implementation

The most conventional and straight forward way to calculate the necessary integrals is to simply view the integrand as a function of a real variable E and to perform the integration numerically, with a sufficiently large negative number being taken as the lower limit of integration. It is necessary to introduce a small positive η in place strictly taking the limit $\eta \to 0$ There are a number of complicating factors for this approach. First off, since we are in one dimension, the Green functions will display Van Hove singularities. These manifest themselves as sharp Lorentzian-type peaks in the Green function. The height of these peaks scales inversely proportional to the size of the small number η, while the width scales in proportion to η. To perform the integration, we need to sample the integrand at energy scales smaller than the width of such features. If we choose a constant step size, this can lead to a very high number of points at which we have to sample the integrand. This suggests that we use a variable step size algorithm to perform these integrals, such as Gaussian-Kronrod quadrature.

There is one point that I must raise, however. Since we are dealing with the logarithm of a complex number z, it is clear that the imaginary part of $\log z$ will

always lie in the range $[0, 2\pi)$ (or some contiguous interval of equal size). In other words, the complex number z is restricted to the first Riemann sheet. Every time the number z passes through the branch cut (as we vary E), we see a discontinuity of size $\pm 2\pi$ in the integrand (depending on which direction we pass the branchcut.

Since the position of the branch cut is arbitrary, we see immediately that such discontinuities are unphysical, and should be corrected. To do this, we tabulate the value of the integrand in the domain of integration. We check the integrand for sudden jumps of size $\simeq 2\pi$. We can keep track of the branch cut by using a tracking function $B(E)$ which takes the discrete values $\cdots, -2\pi, 0, 2\pi \cdots$. Then the integral $\int_{-\infty}^{E_F} \mathrm{d}E \, \log\left(z(E)\right)$.

One way around this is to extend the integral to the complex plane. The basic idea is that we have some sort of integral of the form

$$I = \int_{-\infty}^{E_F} \mathrm{d}E \, \log(z(E)) \tag{E.1}$$

which is numerically expensive due to the discussed features of the integrand. If we can be assured that there are no poles of this function in the upper half plane (as we are for sums and products of retarded Green functions), we may form the contour displayed in Fig. E.1

The integrand has no poles in the upper-half plane. On the large circular arc, the Green function $g(z)$ can be shown to be approximated as $\frac{1}{z}$ (where $|z|$ is extremely large). It can be shown that

$$I := \int_{-\infty}^{E_F} \mathrm{d}E \, \log(z(E)) = -i \int_{0}^{\infty} \mathrm{d}E \, \log(z(iE + E_F)) - \frac{i\pi \mathrm{Tr}\left(\hat{V}\right)}{2} \tag{E.2}$$

where both integrals are carried out over a straight line path.

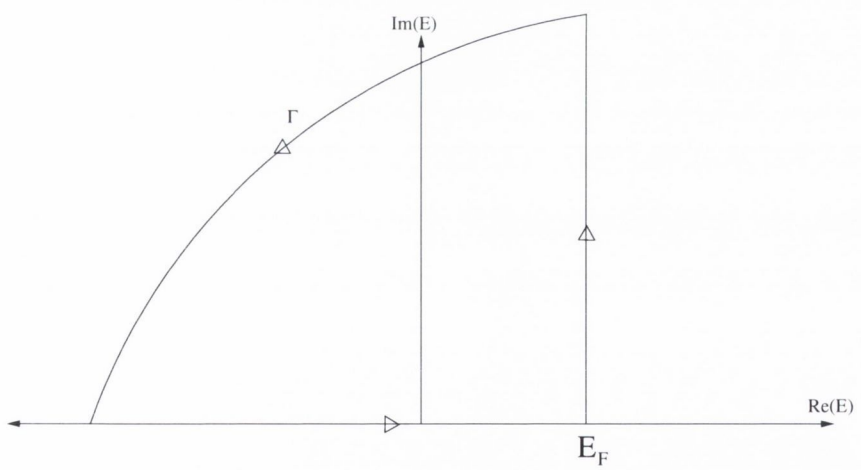

Figure E.1: Schematic of the integration contour chosen in the complex plane to ease numerical integration. The horizontal contour corresponds to the integration we originally sought, the arc is assumed to be taken in the limit of infinite radius, while the vertical line extends from the Fermi energy parallel to the imaginary axis.

Appendix F

Calculation of real space Green function for 1D free electron gas

As an illustration as to how contour integration can be used to provide analytical formulae for matrix elements of certain Green functions, I here provide a derivation of the formula for the diagonal element of the real space Green function matrix element of a one dimensional free electron gas.

Here, we assume that the eigenstates $|x\rangle$ of the position operator $\hat{X}$ form a continuum indexed by the real numbers between $[-L, L]$, where we will ultimately take the limit $Lto\infty$.

We define the Fourier transform of the states $|x\rangle$ through the expression

$$|k\rangle = \frac{1}{\sqrt{2L}} \int_{-L}^{L} \mathrm{d}x \; e^{ikx} |x\rangle. \tag{F.1}$$

Taking the scalar product with a real space ket, we see

$$\begin{aligned} \langle x_0|k\rangle &= \frac{1}{\sqrt{2L}} \int_{-L}^{L} \mathrm{d}x \; e^{ikx} \langle x_0|x\rangle \\ &= \frac{1}{\sqrt{2L}} \int_{-L}^{L} \mathrm{d}x \; e^{ikx} \delta(x_0 - x) \\ &= \frac{1}{\sqrt{2L}} e^{ikx_0}, \end{aligned} \tag{F.2}$$

where we have used the orthonomality relationship between the real space kets. It can be shown that the states $|k\rangle$ diagonalise the free electron Hamiltonian, with corresponding eigenvalue $E_k = \frac{\hbar^2 k^2}{2m}$, where m is the mass of the particle of interest. Correspondingly, we may write the Green function of the gas as

$$\hat{g}(E) = \sum_k \frac{|k\rangle\langle k|}{E + i0^+ - E_k} \tag{F.3}$$

We wish to evaluate $\langle x|\, \hat{g}(E)\, |x'\rangle$. To do this we project with the relevant bra and ket, and use Eq. (F.2) (and its complex conjugate) to find

$$\begin{aligned} \langle x|\, \hat{g}\, |x_0\rangle &= \sum_k \frac{\langle x|k\rangle\langle k|x_0\rangle}{E + i0^+ - E_k} \\ &= \frac{1}{2L} \sum_k \frac{e^{ik(x-x_0)}}{E + i0^+ - \frac{\hbar^2 k^2}{2m}} \end{aligned} \tag{F.4}$$

To perform the sum, we approximate it with an integral, which it will agree with in the limit that we take $L \to \infty$. The allowed values of k in the case of a finite L are the integral multiples of $\frac{2\pi}{2L}$, as determined by the imposition of periodic boundary conditions. This means that $\Delta k = \frac{\pi}{L}$ is the difference between two succesive values of k. We pass from the sum to the integral through the prescription:

$$\sum_k \Delta k f(k) = \int \mathrm{d}k\ f(k) \tag{5}$$

$$\Rightarrow \sum_k f(k) = \frac{L}{\pi} \int \mathrm{d}k\ f(k) \tag{6}$$

where f is the function whose values we wish to sum over. Applying this presciption to Eq. (F.4), we have

$$\begin{aligned} \langle x|\, \hat{g}\, |x_0\rangle &= \frac{1}{2L} \frac{L}{\pi} \int_{-\infty}^{\infty} \mathrm{d}k\ \frac{e^{ik(x-x_0)}}{E + i0^+ - \frac{\hbar^2 k^2}{2m}} \\ &= \frac{1}{2\pi} \int_{-\infty}^{\infty} \mathrm{d}k\ \frac{e^{ik(x-x_0)}}{E + i0^+ - \frac{\hbar^2 k^2}{2m}}. \end{aligned} \tag{7}$$

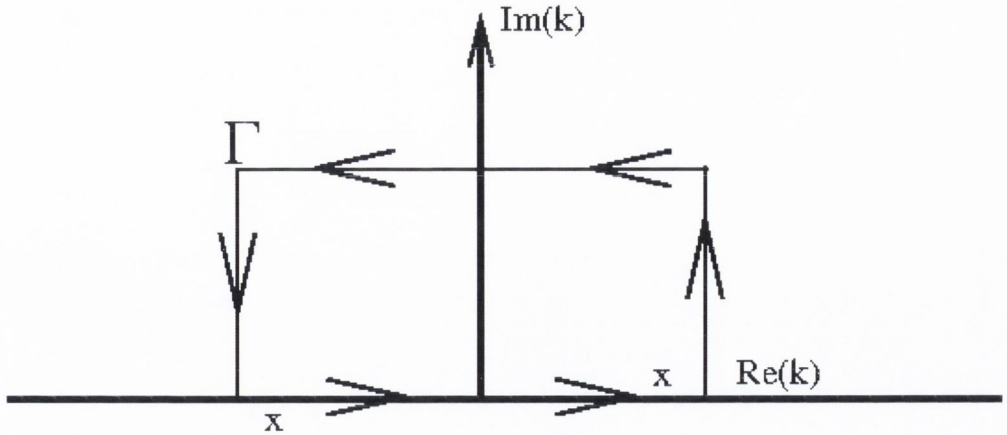

Figure 1: Schematic of the rectangular integration contour chosen to evaluate The Green function of the 1D free electron gas. The horizontal section near the real axis corresponds to the integration we originally sought, and the end points are chosen so that one of the poles (marked with an x) lies inside the contour. By choosing the vertical sections to lie equidistant from the imaginary axis, the evenness of the integrand ensures that their contributions mutually cancel. The other horizontal section is taken in the limit $\mathrm{Im}\,(k) \to \infty$.

This integral is readily performed through the use of contour integration. First off, we note that the integrand possesses two simple poles in the complex plane: at $k = k_0(E) = \pm\frac{\sqrt{2mE+i0^+}}{\hbar}$. To perform the integration, we use a rectangular contour in the complex $k-$plane. If the quantity $x - x_0$ is positive, we close the contour in the upper half plane, and in the lower otherwise. The contour is displayed in Fig. F for the case of positive $x - x_0$.

$$\int_{-\infty}^{\infty} \mathrm{d}k \; \frac{e^{ik(x-x_0)}}{E + i0^+ - \frac{\hbar^2 k^2}{2m}} = \int_{\Gamma} \mathrm{d}k \; \frac{e^{ik(x-x_0)}}{E + i0^+ - \frac{\hbar^2 k^2}{2m}} \tag{8}$$

By using Cauchy's theorem [44], we may evaluate the second of these as

$$\int_{\Gamma} \mathrm{d}k \; \frac{e^{ik(x-x_0)}}{E + i0^+ - \frac{\hbar^2 k^2}{2m}} = -2\pi i m \frac{e^{ik_0(x-x_0)}}{\hbar^2 k_0}. \tag{9}$$

Here we have used the fact if we can write $f(k) = \frac{p(k)}{q(k)}$ as the ratio of two holomorphic functions p and q of complex k, then the residue of f at simple pole k_0 is $\frac{p(k_0)}{q'(k_0)}$, where

$q'(k_0)$ is the derivative of q at k_0. The overall sign is dictated by the fact we traverse the contour in an anticlockwise sense. Including the appropriate prefactors, and plugging in for the value of k_0, we have

$$\langle x|\,\hat{g}\,|x_0\rangle \;=\; -im\frac{e^{i\frac{\sqrt{2mE+i0^+}}{\hbar}(x-x_0)}}{\hbar\sqrt{2mE+i0^+}}. \tag{10}$$

If we choose units such that $m = \hbar = 1$, the diagonal element becomes

$$\langle x_0|\,\hat{g}\,|x_0\rangle \;=\; -i\sqrt{\frac{1}{2E+i0^+}}, \tag{11}$$

as claimed in Eq. 4.4.

Bibliography

[1] S. Iijima. Helical microtubules of graphitic carbon. *Nature*, 354:56–58, November 1991.

[2] Riichiro Saito, Mitsutaka Fujita, G. Dresselhaus, and M. S. Dresselhaus. Electronic structure of graphene tubules based on C_{60}. *Physical Review B*, 46(3):1804–1811, July 1992.

[3] Yuanbo Zhang, Yan-Wen Tan, Horst L. Stormer, and Philip Kim. Experimental observation of quantum hall effect and Berry's phase in graphene. *Nature*, 438:201–204, Nov 2005.

[4] K. S. Novoselov, A. K. Geim, S. V. Morozov, D. Jiang, M. I. Katsnelson, I. V. Grigorieva, S. V. Dubonos, and A. A. Firsov. Two-dimensional gas of massless Dirac fermions in graphene. *Nature*, 438:197–200, Nov 2005.

[5] N. M. R. Peres, F. Guinea, and A. H. Castro Neto. Electronic properties of disordered two-dimensional carbon. *Physical Review B*, 73:125411, 2006.

[6] L. X. Zheng, M. J. O'Connell, S. K. Doorn, X. Z. Liao, Y. H. Zhao, E. A. Akhadov, M. A. Hoffbauer, B. J. Roop, Q. X. Jia, R. C. Dye, D. E. Peterson, S. M. Huang, J. Liu, and Y. T. Zhu. Ultralong single-wall carbon nanotubes. *Nature Materials*, 3:673–676, October 2004.

[7] R. Saito, G. Dresselhaus, and M. S. Dresselhaus. *Physical Properties of Carbon Nanotubes*. Imperial College Press, 1998.

[8] J. W. G. Wildoer, L. C. Venema, A. G. Rinzler, R. E. Smalley, and C. Dekker. Electronic structure of atomically resolved carbon nanotubes. *Nature*, 391:59–62, January 1998.

[9] Léon Van Hove. The occurrence of singularities in the elastic frequency distribution of a crystal. *Physical Review*, 89(6):1189–1193, March 1953.

[10] Philip Kim, Teri W. Odom, Jin-Lin Huang, and Charles M. Lieber. Electronic density of states of atomically resolved single-walled carbon nanotubes: Van Hove singularities and end states. *Physical Review Letters*, 82(6):1225–1228, February 1999.

[11] Stefan Frank, Philippe Poncharal, Z. L. Wang, and Walt A. Heer. Carbon nanotube quantum resistors. *Science*, 280(5370):1744–1746, June 1998.

[12] T. Dürkop, S. A. Getty, E. Cobas, and M. S. Fuhrer. Extraordinary mobility in semiconducting carbon nanotubes. *Nano Letters*, 4(1):35–39, January 2004.

[13] Min-Feng Yu, Bradley S. Files, Sivaram Arepalli, and Rodney S. Ruoff. Tensile loading of ropes of single wall carbon nanotubes and their mechanical properties. *Physical Review Letters*, 84(24):5552–5555, June 2000.

[14] E. Hernández, C. Goze, P. Bernier, and A. Rubio. Elastic properties of C and B_x C_y N_z composite nanotubes. *Physical Review Letters*, 80(20):4502–4505, May 1998.

[15] Lanhua Wei, P. K. Kuo, R. L. Thomas, T. R. Anthony, and W. F. Banholzer. Thermal conductivity of isotopically modified single crystal diamond. *Physical Review Letters*, 70(24):3764–3767, June 1993.

[16] Motoo Fujii, Xing Zhang, Huaqing Xie, Hiroki Ago, Koji Takahashi, Tatsuya Ikuta, Hidekazu Abe, and Tetsuo Shimizu. Measuring the thermal conductivity of a single carbon nanotube. *Physical Review Letters*, 95(6):065502+, 2005.

[17] P. Kim, L. Shi, A. Majumdar, and P. L. McEuen. Thermal transport measurements of individual multiwalled nanotubes. *Physical Review Letters*, 87(21):215502+, October 2001.

[18] Savas Berber, Young-Kyun Kwon, and David Tománek. Unusually high thermal conductivity of carbon nanotubes. *Physical Review Letters*, 84(20):4613–4616, May 2000.

[19] N. Mingo and D. A. Broido. Carbon nanotube ballistic thermal conductance and its limits. *Physical Review Letters*, 95(9):096105, 2005.

[20] Michael Rubinstein and Ralph H. Colby. *Polymer Physics*. Oxford University Press, 2003.

[21] P. M. Ajayan, L. S. Schadler, C. Giannaris, and A. Rubio. Single-walled carbon nanotube-polymer composites: Strength and weakness. *Advanced Materials*, 12(10):750–753, 2000.

[22] E.T. Thostenson, Z Ren, and T.-W Chou. Advances in the science and technology of carbon nanotubes and their composites: a review. *Composites Science and Technology*, 61:1899–1912, October 2001.

[23] J. K. W. Sandler, J. E. Kirk, I. A. Kinloch, M. S. P. Shaffer, and A. H. Windle. Ultra-low electrical percolation threshold in carbon-nanotube-epoxy composites. *Polymer*, 44(19):5893–5899, September 2003.

[24] Alan B. Dalton, Steve Collins, Edgar Muñoz, Joselito M. Razal, Von Howard Ebron, John P. Ferraris, Jonathan N. Coleman, Bog G. Kim, and Ray H. Baughman. Super-tough carbon-nanotube fibres. *Nature*, 423(6941):703, June 2003.

[25] L. S. Schadler, S. C. Giannaris, and P. M. Ajayan. Load transfer in carbon nanotube epoxy composites. *Applied Physics Letters*, 73:3842–3844, December 1998.

[26] J. N. Coleman, M. Cadek, R. Blake, V. Nicolosi, K. P. Ryan, C. Belton, A. Fonseca, J. B. Nagy, Y. K. Gun'ko, and W. J. Blau. High performance nanotube-reinforced plastics: Understanding the mechanism of strength increase. *Advanced Functional Materials*, 14(8):791–798, 2004.

[27] M. Cadek, J. N. Coleman, V. Barron, K. Hedicke, and W. J. Blau. Morphological and mechanical properties of carbon-nanotube-reinforced semicrystalline and amorphous polymer composites. *Applied Physics Letters*, 81(27):5123–5125, 2002.

[28] J. N. Coleman and M. S. Ferreira. Geometric constraints in the growth of nanotube-templated polymer monolayers. *Applied Physics Letters*, 84(5):798–800, 2004.

[29] S. R. Lustig, A. Jagota, C. Khripin, and M. Zheng. Theory of structure-based carbon nanotube separations by ion-exchange chromatography of DNA/CNT hybrids. *J. Phys. Chem. B*, 109(7):2559–2566, February 2005.

[30] S. J. Tans, A. R. M. Verschueren, and C. Dekker. Room-temperature transistor based on a single carbon nanotube. *Nature*, 393:49–52, May 1998.

[31] Sander J. Tans, Michel H. Devoret, Hongjie Dai, Andreas Thess, Richard E. Smalley, L. J. Geerligs, and Cees Dekker. Individual single-wall carbon nanotubes as quantum wires. *Nature*, 386(6624):474–477, April 1997.

[32] Philip G. Collins, Keith Bradley, Masa Ishigami, and A. Zettl. Extreme oxygen sensitivity of electronic properties of carbon nanotubes. *Science*, 287(5459):1801–1804, March 2000.

[33] Jing Kong, Nathan R. Franklin, Chongwu Zhou, Michael G. Chapline, Shu Peng, Kyeongjae Cho, and Hongjie Dai. Nanotube molecular wires as chemical sensors. *Science*, 287(5453):622–625, January 2000.

[34] Phaedon Avouris, Zhihong Chen, and Vasili Perebeinos. Carbon-based electronics. *Nature Nanotechnology*, 2:605–615, October 2007.

[35] Jean-C. Charlier, Xavier Blase, and Stephan Roche. Electronic and transport properties of nanotubes. *Reviews of Modern Physics*, 79(2):677, May 2007.

[36] D. Ciuparu, Y. Chen, S. Lim, G. L. Haller, and L. Pfefferle. Uniform-diameter single-walled carbon nanotubes catalytically grown in cobalt-incorporated MCM-41. *J. Phys. Chem. B*, 108(2):503–507, January 2004.

[37] A. T. Costa Jr., D. F. Kirwan, and M. S. Ferreira. Indirect exchange coupling between magnetic adatoms in carbon nanotubes. *Physical Review B*, 72:085402, 2005.

[38] P. Lloyd. Wave propagation through an assembly of spheres: II. The density of single-particle eigenstates. *Proceedings of the Physical Society*, 90(1):207–216, 1967.

[39] Rudolf Zeller. An elementary derivation of Lloyd's formula valid for full-potential multiple-scattering theory. *Journal of Physics: Condensed Matter*, 16(36):6453–6468, 2004.

[40] Mauro S. Ferreira and Stefano Sanvito. Contact-induced spin polarization in carbon nanotubes. *Physical Review B*, 69(3):035407, 2004.

[41] O. Céspedes, M. S. Ferreira, S. Sanvito, M. Kociak, and J. M. D. Coey. Contact induced magnetism in carbon nanotubes. *Journal of Physics: Condensed Matter*, 16(10):L155–L161, 2004.

[42] B. C. Lee and Y. C. Chang. Interlayer exchange coupling in (111) Co/Cu/Co trilayers: Full-band versus reflection-amplitude calculations. *Physical Review B*, 62(6):3888–3894, 2000.

[43] Subhradip Ghosh, D. A. Biava, W. A. Shelton, and D. D. Johnson. Systematically exact integrated density-of-states Lloyd's formula for disordered alloys with short-range order. *Physical Review B*, 73(8):085106, 2006.

[44] George B. Arfken and Hans J. Weber. *Mathematical Methods For Physicists.* Academic Press, June 2005.

[45] Jun Li, Qi Ye, Alan Cassell, Hou T. Ng, Ramsey Stevens, Jie Han, and M. Meyyappan. Bottom-up approach for carbon nanotube interconnects. *Applied Physics Letters*, 82(15):2491–2493, 2003.

[46] Jia Chen, Christian Klinke, Ali Afzali, and Phaedon Avouris. Self-aligned carbon nanotube transistors with charge transfer doping. *Applied Physics Letters*, 86(12):123108, 2005.

[47] W. Kohn and J. M. Luttinger. Theory of donor states in silicon. *Physical Review*, 98(4):915–922, May 1955.

[48] F. J. Morin and J. P. Maita. Electrical properties of silicon containing Arsenic and Boron. *Physical Review*, 96(1):28–35, October 1954.

[49] Jae-Yel Yi and J. Bernholc. Atomic structure and doping of microtubules. *Physical Review B*, 47(3):1708–1711, January 1993.

[50] D. Grimm, A. Latgé, R. B. Muniz, and M. S. Ferreira. Transport suppression in polymer-doped zigzag carbon nanotubes. *Physical Review B*, 71(11):113408, 2005.

[51] L. Duclaux. Review of the doping of carbon nanotubes (multiwalled and single-walled). *Carbon*, 40(10):1751–1764, August 2002.

[52] W. Zhou, J. Vavro, N. M. Nemes, J. E. Fischer, F. Borondics, K. Kamarás, and D. B. Tanner. Charge transfer and Fermi level shift in p-doped single-walled carbon nanotubes. *Physical Review B*, 71(20):205423, 2005.

[53] R. Czerw, M. Terrones, Jean-C. Charlier, X. Blase, B. Foley, R. Kamalakaran, N. Grobert, H. Terrones, D. Tekleab, P. M. Ajayan, W. Blau, M. Rühle, and D. L. Carroll. Identification of electron donor states in n-doped carbon nanotubes. *Nano Letters*, 1(9):457–460, September 2001.

[54] Jing Kong, Jien Cao, Hongjie Dai, and Erik Anderson. Chemical profiling of single nanotubes: Intramolecular p–n–p junctions and on-tube single-electron transistors. *Applied Physics Letters*, 80(1):73–75, 2002.

[55] Yu-Liang Mao, Xiao-Hong Yan, and Yang Xiao. First-principles study of transition-metal-doped single-walled carbon nanotubes. *Nanotechnology*, 16(12):3092–3096, December 2005.

[56] Sylvain Latil, Stephan Roche, Didier Mayou, and Jean-C. Charlier. Mesoscopic transport in chemically doped carbon nanotubes. *Physical Review Letters*, 92(25):256805, 2004.

[57] S. Latil, S. Roche, and Jean-C. Charlier. Electronic transport in carbon nanotubes with random coverage of physisorbed molecules. *Nano Letters*, 5(11):2216–2219, November 2005.

[58] Ch. Adessi, Stephan Roche, and X. Blase. Reduced backscattering in potassium-doped nanotubes: Ab initio and semiempirical simulations. *Physical Review B*, 73(12):125414, 2006.

[59] A. V. Krasheninnikov, K. Nordlund, P. O. Lehtinen, A. S. Foster, A. Ayuela, and R. M. Nieminen. Adsorption and migration of carbon adatoms on carbon nanotubes: Density-functional ab initio and tight-binding studies. *Physical Review B*, 69(7):073402, 2004.

[60] Ronald E. Cohen, Michael J. Mehl, and Dimitrios A. Papaconstantopoulos. Tight-binding total-energy method for transition and noble metals. *Physical Review B*, 50(19):14694–14697, November 1994.

[61] Diana E. Tuyarot, Belita Koiller, and R. B. Capaz. Tight-binding total-energy method applied to polyacetylene. *Physical Review B*, 61(11):7187–7190, March 2000.

[62] Richard M. Martin. *Electronic Structure: Basic Theory and Practical Methods.* Cambridge University Press, April 2004.

[63] W. Matthew C. Foulkes and Roger Haydock. Tight-binding models and density-functional theory. *Physical Review B*, 39(17):12520–12536, June 1989.

[64] J. Zhao and J. P. Lu. A nonorthogonal tight-binding total energy model for molecular simulations. *Physics Letters A*, 319:523–529, December 2003.

[65] Daniel Sánchez-Portal, Pablo Ordejón, Emilio Artacho, and José M. Soler. Density-functional method for very large systems with LCAO basis sets. *International Journal of Quantum Chemistry*, 65(5):453–461, 1997.

[66] Pablo Ordejón, Emilio Artacho, and José M. Soler. Self-consistent order-N density-functional calculations for very large systems. *Physical Review B*, 53(16):R10441–R10444, April 1996.

[67] D. M. Ceperley and B. J. Alder. Ground state of the electron gas by a stochastic method. *Physical Review Letters*, 45(7):566–569, 1980.

[68] Hyoungki Park, Jijun Zhao, and Jian P. Lu. Distinct properties of single-wall carbon nanotubes with monovalent sidewall additions. *Nanotechnology*, 16(6):635–638, June 2005.

[69] J. W. Mintmire and C. T White. Electronic and structural properties of carbon nanotubes. *Carbon*, 33(7):893–902, February 1995.

[70] C. G. Rocha, T. G. Dargam, and A. Latgé. Electronic states in zigzag carbon nanotube quantum dots. *Physical Review B*, 65(16):165431, April 2002.

[71] J. Mathon, Murielle Villeret, and H. Itoh. Selection rules for oscillations of the giant magnetoresistance with nonmagnetic spacer layer thickness. *Physical Review B*, 52(10):R6983+, 1995.

[72] C. G. Rocha, A. Wall, A. R. Rocha, and M. S. Ferreira. Modelling the effect of randomly dispersed adatoms on carbon nanotubes. *Journal of Physics: Condensed Matter*, 19(34):3446–3449, 2007.

[73] Claudia G. Rocha, Andrew Wall, and Mauro S. Ferreira. Electronic properties of nanotube-based sensors: An inverse modeling approach. *Europhysics Letters*, 82:27004+, March 2008.

[74] C. G. Rocha, A. Wall, A. R. Rocha, and M. S. Ferreira. Modeling the effect of dispersed doping agents in carbon nanotubes. *Journal of Nanoscience and Nanotechnology*, 7(10):3446–3449, October 2007.

[75] K. H. An, S. Y. Jeong, H. R. Hwang, and Y. H. Lee. Enhanced sensitivity of a gas sensor incorporating single-walled carbon nanotube-polypyrrole nanocomposites. *Advanced Materials*, 16(12):1005–1009, 2004.

[76] B. E. Kilbride, J. N. Coleman, J. Fraysse, P. Fournet, M. Cadek, A. Drury, S. Hutzler, S. Roth, and W. J. Blau. Experimental observation of scaling laws for alternating current and direct current conductivity in polymer-carbon nanotube composite thin films. *Journal of Applied Physics*, 92(7):4024–4030, 2002.

[77] Ming Zheng, Anand Jagota, Ellen D. Semke, Bruce A. Diner, Robert S. Mclean, Steve R. Lustig, Raymond E. Richardson, and Nancy G. Tassi. DNA-assisted dispersion and separation of carbon nanotubes. *Nature Materials*, 2(5):338–342, May 2003.

[78] B. McCarthy, J. N. Coleman, S. A. Curran, A. B. Dalton, A. P. Davey, Z. Konya, A. Fonseca, J. B. Nagy, and W. J. Blau. Observation of site selective binding in a polymer nanotube composite. *Journal of Materials Science Letters*, 19(24):2239–2241, December 2000.

[79] B. Z. Tang and H. Xu. Preparation, alignment, and optical properties of soluble poly(phenylacetylene)-wrapped carbon nanotubes. *Macromolecules*, 32(8):2569–2576, April 1999.

[80] Michael J. O'Connell, Peter Boul, Lars M. Ericson, Chad Huffman, Yuhuang Wang, Erik Haroz, Cynthia Kuper, Jim Tour, Kevin D. Ausman, and Richard E. Smalley. Reversible water-solubilization of single-walled carbon nanotubes by polymer wrapping. *Chemical Physics Letters*, 342(3-4):265–271, July 2001.

[81] V. V. Didenko, V. C. Moore, D. S. Baskin, and R. E. Smalley. Visualization of individual single-walled carbon nanotubes by fluorescent polymer wrapping. *Nano Letters*, 5(8):1563–1567, August 2005.

[82] R. Czerw, Z. Guo, P. M. Ajayan, Y. P. Sun, and D. L. Carroll. Organization of polymers onto carbon nanotubes: A route to nanoscale assembly. *Nano Letters*, 1(8):423–427, August 2001.

[83] Amos Maritan, Cristian Micheletti, Antonio Trovato, and Jayanth R. Banavar. Optimal shapes of compact strings. *Nature*, 406(6793):287–290, July 2000.

[84] Andrew Wall and Mauro S. Ferreira. Electronic contribution to the energetics of helically wrapped nanotubes. *Physical Review B*, 74(23):233401, 2006.

[85] Andrew Wall and Mauro S. Ferreira. Electronic density of states of helically-wrapped carbon nanotubes. *Journal of Physics: Condensed Matter*, 19(40):406227+, 2007.

[86] Eugen Merzbacher. *Quantum Mechanics*, chapter 6, pages 107–108. John Wiley & Sons, Inc., New York, 1998.

[87] J. N. Coleman, A. Fleming, S. Maier, S. O'Flaherty, A. I. Minett, M. S. Ferreira, S. Hutzler, and W. J. Blau. Binding kinetics and swnt bundle dissociation in low concentration polymer-nanotube dispersions. *J. Phys. Chem. B*, 108(11):3446–3450, March 2004.

[88] J. N. Coleman. Private communication, 2007.

[89] Daniel A. Heller, Esther S. Jeng, Tsun-Kwan Yeung, Brittany M. Martinez, Anthonie E. Moll, Joseph B. Gastala, and Michael S. Strano. Optical detection of DNA conformational polymorphism on single-walled carbon nanotubes. *Science*, 311(5760):508–511, January 2006.

[90] A. Wall, J. N. Coleman, and M. S. Ferreira. Physical mechanism for the mechanical reinforcement in nanotube-polymer composite materials. *Physical Review B*, 71(12):125421+, 2005.

[91] R. Murphy, J. N. Coleman, M. Cadek, B. McCarthy, M. Bent, A. Drury, R. C. Barklie, and W. J. Blau. High-yield, nondestructive purification and quantification method for multiwalled carbon nanotubes. *J. Phys. Chem. B*, 106(12):3087–3091, March 2002.

[92] Weiren Chou and Robert B. Griffiths. Ground states of one-dimensional systems using effective potentials. *Physical Review B*, 34(9):6219–6234, November 1986.

[93] O. M. Braun and Y. S. Kivshar. Nonlinear dynamics of the Frenkel-Kontorova model. *Physics Reports*, 306:1–108, December 1998.

[94] M. D. Miller. Ground-state phase diagrams for an oriented atomic chain on a triangular lattice. *Physical Review B*, 41(16):11396–11404, June 1990.

[95] Peiqing Tong, Baowen Li, and Bambi Hu. Wave transmission, phonon localization, and heat conduction of a one-dimensional Frenkel-Kontorova chain. *Physical Review B*, 59(13):8639–8645, April 1999.

[96] S. Aubry. Exact models with a complete devil's staircase. *Journal of Physics C: Solid State Physics*, 16(13):2497–2508, 1983.

[97] P. Bak. Commensurate phases, incommensurate phases and the devil's staircase. *Reports on Progress in Physics*, 45(6):587–629, 1982.

[98] Aleksey N. Kolmogorov and Vincent H. Crespi. Smoothest bearings: Interlayer sliding in multiwalled carbon nanotubes. *Physical Review Letters*, 85(22):4727–4730, November 2000.

[99] Jonathan N. Coleman, Martin Cadek, Kevin P. Ryan, Antonio Fonseca, Janos B. Nagy, Werner J. Blau, and Mauro S. Ferreira. Reinforcement of polymers with carbon nanotubes. The role of an ordered polymer interfacial region. Experiment and modeling. *Polymer*, 47(26):8556–8561, December 2006.